UCL
Université catholique de Louvain

École polytechnique de Louvain (EPL)

Numerical Investigation of an Offshore Vertical Axis Wind Turbine Farm

From the Wind Resource to the Control and Power Generation

Dissertation presented by
Charlène Collin, Valentin Moëns

for obtaining the Master's degree in
Electro-mechanical Engineering in Energy, Mechanical Engineering

Supervisor(s)
Philippe Chatelain, Emmanuel De Jaeger

Reader(s)
Caroline Leroi, Maud Moens, Dirk Van Hertem

Academic year 2016-2017

ABSTRACT

In order to fight climate change, renewable energy sources have become more and more attractive as part of the electrical energy mix of Europe. However, the existing technologies still need improvement in order to become competitive and phase fossil fuels out of the energy sector. In that regard, offshore wind has proven to be an interesting solution and still under-exploited resource.

This study explores whether vertical axis wind turbines could be an attractive alternative compared to the existing offshore horizontal axis wind turbine farms, thanks to a reduced levelized cost of electricity. This study uses numerical simulations to provide a first assessment.

In this technical investigation, the entire conversion chain is simulated from the wind resource to the electricity transmitted to the grid. One program simulates the mechanical behaviour of the wind turbine using the double multiple stream tubes model, another simulates the electrical power transformation and transport from the wind turbine to the grid. A one-way coupling is used between both programs in the form of a unique and common wind turbine speed controller. Finally, the coupling is tested on an offshore wind farm of 15 wind turbines of 5MW rated power each. The study demonstrates that DMST simulations do not provide reliable results for VAWTs. The electrical model proves to be robust and could be used for HAWT and VAWT farms. The coupling method is effective and proves to be at low computation cost.

ACKNOWLEDGMENTS

As this master thesis is the accomplishment of our engineering studies, many people helped produce the final results summarized in this report. We would like to thank them by acknowledging them.

First of all, many thanks to our supervisors, Prof. Philippe Chatelain and Prof. Emmanuel De Jaeger, for their expertise and guidance throughout the year. As well as to Caroline Leroi and Maud Moens for their availability and support every step of the way.

We would also like to thank Prof. Dirk Van Hertem for accepting to be an official jury of this work. We hope the results interest him as much as it did interest us.

We are also grateful for the support and the feedback on the report of Rudi Collin, Thibaut Deceuleneer, Luc Machiels and Jean-Pierre Moëns.

We would like to acknowledge the Consortium des Équipements de Calcul Intensif (CÉCI) who provided the computational resources, which is funded by the Fonds de la Recherche Scientifique de Belgique (F.R.S.-FNRS) under Grant No. 2.5020.11. And more particularly, we would like to thank Damien François who provided the thorough training sessions on the use of high-performance computing and all related tools. The present research also benefited from computational resources made available on the Tier-1 supercomputer of the Fédération Wallonie-Bruxelles, infrastructure funded by the Walloon Region under the grant agreement n°1117545.

We also thank Isabelle Hennau, who has been a precious help and lively support for many years now.

Finally, we would like to express our profound gratitude towards our families and close friends who supported us continuously throughout our years of study and encouraged us during the process of writing this thesis.

CONTENTS

LIST OF FIGURES

LIST OF TABLES

LIST OF ACRONYMS

ABL	Atmospheric Boundary Layer
AC	Alternating Current
AD	Actuator Disk
AVEM	Average Voltage Estimation Model
CFD	Computational Fluid Dynamics
DD	Direct Drive
DFIG	Doubly-Fed Induction Generator
DMST	Double Multiple Stream Tubes
DTC	Direct Torque Control
EMCC	Electro-Mechanical Conversion Chain
FOC	Field Oriented Control
GSC	Grid Side Converter
HAWT	Horizontal Axis Wind Turbine
HV	High Voltage
HVAC	High Voltage Alternative Current
LCOE	Levelised Cost of Electricity
LES	Large Eddy Simulation
LV	Low Voltage
MPPT	Maximum Power Point Tracking
MV	Medium Voltage
NREL	National Renewable Energy Laboratory
O&M	Operation and Maintenance
PCC	Point of Common Coupling
PLL	Phase Locked Loop
PMSG	Permanent Magnet Synchronous Generator
PWM	Pulse-Width Modulation
RF	Radial Feeder
SCIG	Squirrel Cage Induction Generator
SSC	Stator Side Converter
THD	Total Harmonic Distortion
TKE	Turbulent Kinetic Energy
TSR	Tip Speed Ratio
VAWT	Vertical Axis Wind Turbine
VPM	Vortex Particle-Mesh
WECS	Wind Energy Conversion System
WRSG	Wound-Rotor Synchronous Generator
$0dq$	Direct-Quadrature-Zero

LIST OF SYMBOLS

Mechanical Symbols

a	Induction Factor	[-]
A	Cross-Sectional Area	$[m^2]$
A_r	Aspect Ratio	[-]
α	Angle of Attack	$[rad]$
B	Number of blades	[-]
c	Chord Length	$[m]$
C_P	Power Coefficient	[-]
C_T	Thrust Coefficient	[-]
χ	Expansion Factor	[-]
D	Drag	$[N]$
F	Force or Thrust	$[N]$
H	Height	[m]
L	Lift	[N]
λ	Tip Speed Ratio	[-]
ν	Kinematic Viscosity	$[m^2/s]$
ω	Rotational Speed	$[rpm]$
p	Pressure	$[Pa]$
P	Power	$[W]$
R	Radius	$[m]$
Re	Reynolds	[-]
ρ	Air Density	$[kg/m^3]$
σ	Solidity	[-]
T	Torque	$[Nm]$
U	Flow Speed	$[m/s]$
w	Wake	[-]
∞	Upstream	[-]

Electrical Symbols

C	Capacitance	$[F]$
I	Current	$[A]$
L	Inductance	$[H]$
P	Active Power	$[W]$
ψ	Flux	$[Wb]$
Q	Reactive Power	$[VAR]$
R	Resistance	$[\Omega]$
V	Voltage	$[V]$

INTRODUCTION

In order to tackle climate change and therefore phase out conventional energy sources, the share of renewable energy sources inside the total energy mix is increasing. Wind energy, more particularly, is expected to play a key role in this sense. Wind power generation is constantly expanding with a total generation of 5.468 GWh in Belgium, which meets 8.03% (in 2015) of the country's need of electricity [1]. From that portion, about half is produced by offshore wind farms containing horizontal axis wind turbines (HAWT).

The levelised cost of electricity (LCOE) of offshore wind energy has fallen down to 126 $/MWh in 2016 [2] for farms containing HAWTs. The LCOE is equal to the total costs over the lifetime of the wind farm divided by the electricity produced over its lifetime. That cost is broken down into the investment costs, the operation and maintenance costs (O&M) and cost of capital, the capacity factor and the economic lifetime to be computed. The capital cost, called CAPEX, encompasses the turbine, grid connection and construction costs [3]. The breakdown of the cost of a HAWT shows that the tower, the rotor blades and the gearbox amount for the highest share of the cost (about 62%). Between 25 and 30% of the total costs of offshore wind farms are the operation and maintenance costs [4]. This is mainly due to the difficulty of access of the turbines and the lack of collaboration between the farm operators.

Vertical axis wind turbines (VAWT) have several advantages compared to the horizontal axis ones, even though aerodynamically, they are theoretically less efficient. The VAWT operates at a lower height, closer to the ground, which allows for the components of the nacelle, such as the generator, the power converter and the transformer, to be placed at ground level. As this is heavy equipment, it will allow a significant decrease in construction costs and in O&M costs. In VAWTs, no yaw control is needed as the energy from the wind can be harnessed independently of its direction.

Knowing this, one could find it interesting to compare an offshore VAWT farm with a HAWT farm in order to discover if the LCOE can be lowered. This study offers a technical comparison between HAWTs and VAWTs by simulating the power conversion from the wind resource to the electrical power. It also studies the ability to couple, in a one way method, the mechanical and electrical parts using two different programs.

Chapter 1 focuses solely on the mechanical part of the investigation and proposes the description of the aerodynamic models used to simulate a VAWT farm behaviour. It begins with the mathematical development of an actuator surface based model, the double multiple stream tubes model, which simplifies the computation of the rotor behaviour at the cost of strong hypotheses. Then, the model performances are evaluated in comparison with high fidelity results generated by a vortex model developed at UCL. Finally, the geometry of a 5 MWe turbine is determined and its performances are compared to those of a reference HAWT currently under study at UCL.

Chapter 2 aims at summarising the study of the electro-mechanical power conversion. Starting from the mechanical power created by the wind turbine, electricity is produced and transmitted to an onshore point of common coupling of the grid. First, the implementation of the various controls of the individual wind turbines is explained and the results of simulations performed on the program Matlab Simulink - simscape Power Systems are presented. Then, for computational cost reasons, the model is simplified into an average model of the operation of the power converter. Finally, the wind turbines are inserted into the final topology and tested.

Chapter 3 gives more insight on the method of coupling: the output of the mechanical part is used as input of the electrical part and the results are compared. The goal is to determine if this coupling method provides realistic results. Then, a comparison between a VAWT farm and a HAWT farm of same rated power and topology is carried out.

CHAPTER 1

MECHANICAL PART

1.1 Technical Context

A Vertical Axis Wind Turbine (VAWT) is an electro-mechanical device which allows to convert part of the wind kinetic energy in mechanical then electrical energy thanks to a generator. The blades of such turbines rotate around their vertical axis, contrary to their Horizontal Axis Wind Turbines (HAWT) counterparts.

This work on the mechanical part follows the master's theses of Taverne [5] and Donnay [6].

1.1.1 Description of VAWTs

Classification

VAWTs are divided in two main families, depending on the origin of the aerodynamic force generating mechanical power. First, drag-based turbines - also called Savonius from their Finnish inventor's name - rely on the drag force generated by the wind on scoops mounted on a rotating shaft. The S-shape of their scoops allows for a stronger drag force when the scoop is moving with the wind than when it is moving against it. Due to their drag-based mode of operation, they show poor performance at extracting power from the wind resource. Then come lift-based VAWTs - named Darrieus after their French inventor - which rely on the lift force generated by the blades in order to rotate. The Darrieus turbines can be sub-divided in three categories depending on their blade design (see Figure 1.1) : ϕ-shaped or parabolic, H-shaped with straight blades, and helical rotors. The latter show a better torque distribution over a rotation, reducing the periodic loading amplitude on the structure of the wind turbine, and increasing their lifetime, but this advantage comes at a greater manufacturing cost.

Geometry

This thesis focuses on the study of three-bladed H-rotor VAWTs. The three straight blades are equally distributed at a radius R and form the rotor. They are characterised by their chord length, c, and their length is referred to as the rotor height, H. Figure 1.2 represents this geometry, with U_∞, the upstream wind velocity, and ωR the speed of the blades.

1.1.2 Aerodynamic Prediction Models

Several methods currently exist in the study of the aerodynamics of VAWTs [10] : the most common makes use of computational fluid dynamics (CFD) in order to solve Navier-Stokes equations. The direct integration of lift and drag forces from the wind turbine blades requires a

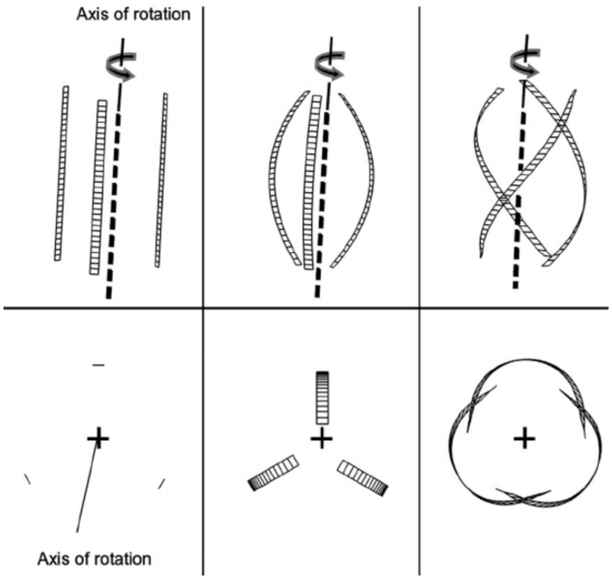

Figure 1.1: Darrieus VAWT's types. From left to right : H-rotor, ϕ-rotor, helical rotor. Top : dimetric projection, Bottom : plan view [9]

fine mesh to capture their effect, which increases the computational cost of such method. Then come vortex methods, for example the Vortex Particle-Mesh Method (VPM), developed at UCL, and providing excellent results [17]. Finally, momentum methods are much simpler and cheaper to implement, but require strong hypotheses. The model chosen in this thesis implements a momentum-based method, used in a CFD code developed at UCL, to provide results about the turbine's wake and the possible use of VAWTs in a wind farm.

Actuator Disk Model

First of all, the concept of actuator surface is described. A mechanical element harnessing power from a fluid can be represented in a simple manner by a two dimensional surface through which the given fluid is passing, creating a pressure discontinuity in the flow [7]. The actuator surface partially absorbs energy from the fluid, causing the latter to slow down (see Figure 1.3).

Methods based on momentum balance require an expression for the force applied by the fluid on the given actuator surface. In order to compute this force, several hypotheses are assumed : surface of infinitesimal thickness, perfect incompressible fluid, one dimensional, stationary and irrotational flow.

Mass flow rate conservation is applied to a control volume between the upstream flow and

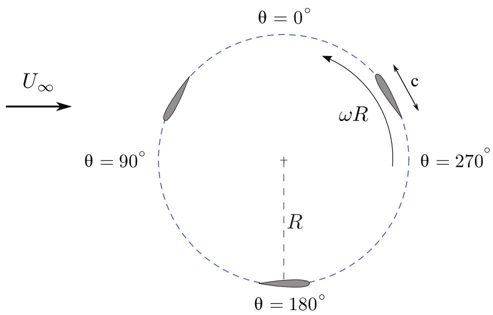

Figure 1.2: VAWT geometry and azimuthal position

the wake, and yields :

$$U_\infty A_\infty = U A = U_w A_w \tag{1.1}$$

with U, the flow speed, and A the cross-sectional area of the considered stream tube. Subscripts ∞ and w refer respectively to the upstream flow, and the wake.

Assuming the continuity of velocity through the actuator surface gives : $U_+ = U_- = U$. The energy extracted from the fluid implies a pressure decrease, $\Delta p = p_+ - p_-$. Since the flow is frictionless and there is no work or no energy transfer, Bernoulli equation can then be applied up and downstream of the actuator surface, where it is assumed that the pressure has recovered its upstream value p_∞ :

$$\begin{aligned} p_\infty + 0.5\,\rho\,U_\infty^2 &= p_+ + 0.5\,\rho\,U^2 \\ p_- + 0.5\,\rho\,U^2 &= p_\infty + 0.5\,\rho\,U_w^2 \end{aligned} \tag{1.2}$$

The pressure drop can be expressed from the two previous equations :

$$\Delta p = 0.5\,\rho\,(U_\infty^2 - U_w^2) \tag{1.3}$$

Provided that there is a stationary flow, this pressure drop encountered at the actuator surface corresponds to the force applied by the surface onto the fluid, as well as to its momentum change:

$$T = \dot{m}\,(U_\infty^2 - U_w^2) = \rho\,A\,U\,(U_\infty - U_w) \tag{1.4}$$

$$T = A\Delta p = 0.5\,\rho\,A(U_\infty^2 - U_w^2) \tag{1.5}$$

These two equation yield an expression for the wind speed at the actuator surface :

$$U = 0.5\,(U_\infty + U_w) \tag{1.6}$$

In other words, the wind speed at the actuator surface corresponds to the arithmetic mean value between up and downstream wind speed values. By defining the induction factor a as the wind speed decrease ratio between upstream conditions and the rotor, the following expressions are derived:

$$a = \frac{U_\infty - U}{U_\infty} \tag{1.7}$$

$$U = (1-a)U_\infty \tag{1.8}$$

$$U_w = (1-2a)U_\infty \tag{1.9}$$

Combining Equations 1.5 and 1.9, yields the following expression for thrust in the stream tube direction F_x :

$$F_x = 0.5\,\rho\,A\,U_\infty^2\,4a\,(1-a) \tag{1.10}$$

1.1.3 Introduction to the VAWT Aerodynamics

This section defines the concepts used further in the current chapter.

Power Coefficient

The effectiveness of a VAWT in extracting mechanical power, P, from wind is characterised by the power coefficient, C_P :

$$C_P = \frac{P}{0.5\rho A U_\infty^3} \qquad [-] \tag{1.11}$$

where ρ is the air density, A is the swept area $2RH$ of the rotor.

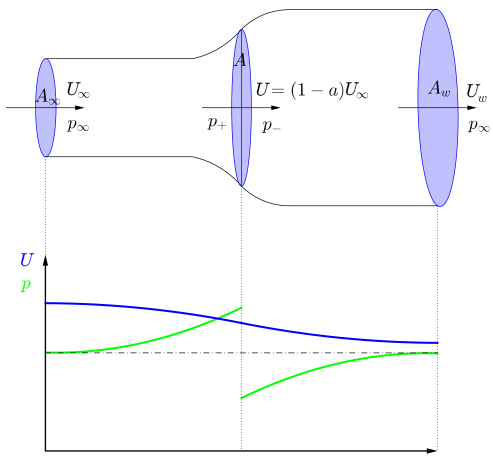

Figure 1.3: Stream tube (adapted from [5])

Thrust Coefficient

The thrust coefficient, C_T, is an indicator of the effect of the rotor on the fluid flow

$$C_T = \frac{F_x}{0.5\rho A U_\infty^2} \qquad [-] \tag{1.12}$$

Solidity

The rotor solidity expresses the ratio between the surface occupied by the blades, with regards to the swept area :

$$\sigma = \frac{Bc}{2R} \qquad [-] \tag{1.13}$$

where B is the number of blades of the rotor, and c is their profile chord length. It is worth noting that various expressions of solidity exist [11], and this one has been chosen for the sake of continuity with previous works [5, 6].

Tip Speed Ratio

The tip speed ratio is an adimensional parameter used to characterise a wind turbine, noted TSR, or λ :

$$TSR = \frac{\omega R}{U_\infty} \qquad [-] \tag{1.14}$$

It represents the ratio of the speed at the blade tips due to rotation, ωR, with the free stream wind speed.

Aspect Ratio

The aspect ratio used throughout this thesis corresponds to the ratio of the rotor height, H, with its diameter, D:

$$A_R = \frac{H}{D} \qquad [-] \tag{1.15}$$

1.1.4 Flow Physics of VAWTs

Cyclic Behaviour

The study of the aerodynamics of VAWT is complex due to the cyclic events experienced by the blades. Indeed, when the rotor is in operation, the blades of a VAWT will face incoming wind with alternatively positive and negative angles of attack, meaning that improvements realised on a blade for half a cycle will decrease the performances for the other half of the cycle [11]. Studies on variable pitch VAWTs show that adapting the pitch of the blades along their trajectory could be beneficial for their overall performances [13].

Dynamic Stall

Dynamic stall is a phenomenon taking place with unsteady aerodynamic behaviour as it is the case for VAWT. It is characterised by a delay of stall with comparison to static behaviour, depending on the rate of change of the angle of attack [14]. Its effects are therefore happening when the blades perceive wind speeds which locally go past their critical angle (i.e. the angle of attack at which stall occurs in static conditions), which is the case at low TSR. Results from the studied model extended to dynamic stall effects being inconclusive, the investigation has been carried out with the original model without dynamic stall.

1.2 Double Multiple Stream Tubes Model[1]

The Double Multiple Stream Tubes model (DMST) has been chosen in this thesis for its ease of implementation, effective computational cost and promising results [8]. This method uses the concept of actuator surfaces, by dividing the flow passing through the wind turbine in multiple stream tubes, and for each of them combines a pair of actuator surfaces (placed at the up and downstream parts of the rotor). Different variants of the model exist, the one used throughout this thesis makes uses of expanding stream tubes and variable induction factors between the up and downstream actuator disks.

1.2.1 Stream Tubes Expansion

The mass flow rate conservation combined to a decreasing wind speed through the wind turbine implies stream tubes expansion (Figure 1.4). It is firstly assumed that the vertical expansion along the y-axis is negligible, impeding that stream tubes expansion only occurs in the horizontal plane. Secondly, stream tubes are assumed to be straight. Finally, an incompressible flow in each stream tube is assumed, which implies that a section area, A_e, exists at some location along the stream tube, conserving the cross-sectional area of a tube without expansion, leading to the following formulation for a constant air density and per stream tube height :

$$A_{up}\,U_{up} = A_e\,U_e = A_{dw}\,U_{dw} \tag{1.16}$$

with A_{up} and A_{dw}, the inlet and outlet stream tube cross-sectional areas. A_e is the arithmetic average of these areas due to an even angle shifting between up and downstream intersections:

$$A_e = \frac{A_{up} + A_{dw}}{2} \tag{1.17}$$

Combining Equations 1.16 and 1.17 provides an expression for U_e :

$$U_e = \frac{2\,U_{up}\,U_{dw}}{U_{up} + U_{dw}} \tag{1.18}$$

[1]This section is adapted from [5] and [11].

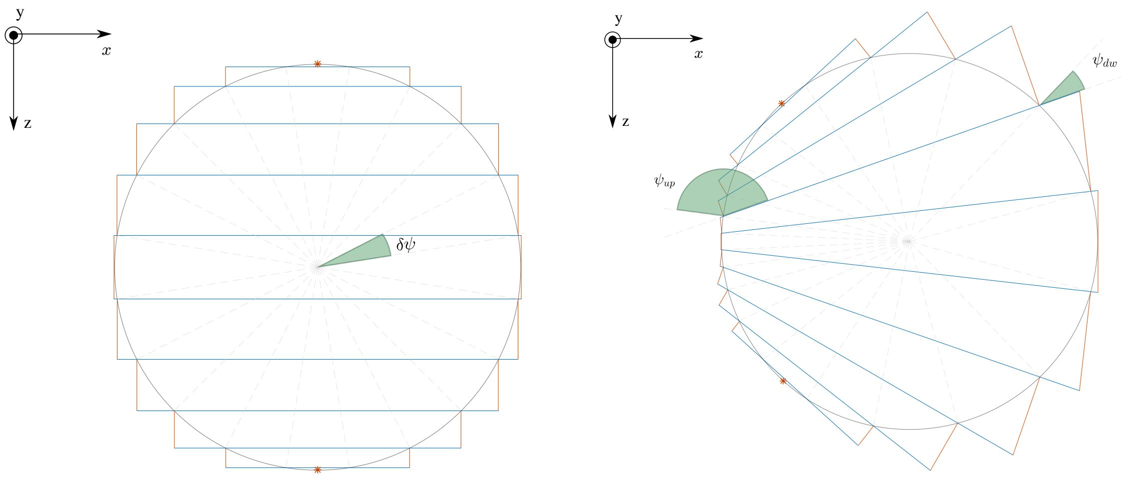

(a) Stream tubes without expansion

(b) Stream tube expansion

Figure 1.4: Stream tubes representation for $TSR = 4.28$ and a number of points on the circumference $N_t = 20$ (* : represents the application of a single actuator surface at the extremities of the rotor)

The area A_e can be computed from a configuration without expansion, depending on the arc cut off the circumference by the stream tube:

$$A_e = R\sin(\psi + \delta\psi) - R\sin(\psi) \tag{1.19}$$

with ψ referring here to the intersection of the lower edge of the chosen stream tube with the circumference, and $\delta\psi = 2\pi/N_t$ the angular step between two consecutive intersections, considering N_t points equally distributed on the circumference for the definition of the streamtubes without expansion. Assuming small $\delta\psi$ angles leads to the approximation :

$$A_e \approx R\cos(\psi)\delta\psi \tag{1.20}$$

Equations 1.18 and 1.20 of U_e and A_e are now replaced in Equation 1.16 :

$$\begin{aligned} R\cos(\psi)\delta\psi \frac{2\,U_{up}\,U_{dw}}{U_{up}+U_{dw}} &= A_{up}\,U_{up} = A_{dw}\,U_{dw} \\ &= R\cos(\psi)\,\Delta\theta_{up}\,U_{up} = R\cos(\psi)\,\Delta\theta_{dw}\,U_{dw} \end{aligned} \tag{1.21}$$

with $\Delta\theta_{up}$ and $\Delta\theta_{dw}$ expressing the variation in azimuthal position of a stream tube extremities with regards to the previous one.

Expansion factors up and downstream are now defined:

$$\begin{aligned} \chi_{up} &= \frac{2U_{dw}}{U_{up}+U_{dw}} < 1 \\ \chi_{dw} &= \frac{2U_{up}}{U_{up}+U_{dw}} > 1 \end{aligned} \tag{1.22}$$

leading to an expression for the variation in azimuthal position of the next stream tube:

$$\begin{cases} \Delta\theta_{up} &= \chi_{up}\delta\psi \\ \Delta\theta_{dw} &= \chi_{dw}\delta\psi \end{cases} \tag{1.23}$$

The stream tubes limits are then computed starting from the central one towards the extremities of the wind turbine, and single actuator disks are added ate the two extremities of the rotor (see Figure 1.4).

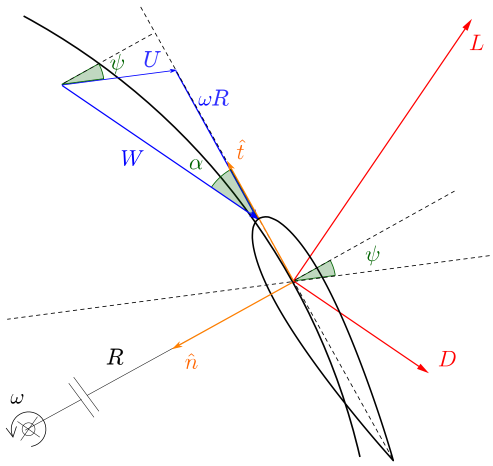

Figure 1.5: Flow around a blade and forces involved

1.2.2 Local Flow Geometry

Figure 1.5 depicts the speeds and forces playing a role in the aerodynamics of the blades.

Relative Speed

The relative speed W of the blade with respect to the wind takes two contributions into account: U, the incident wind speed on the blade following the stream tube direction, and ωR due to the blade rotation and tangent to its trajectory. The relative speed can be decomposed in normal and tangential components:

$$W_n = -U \cos\psi \qquad \text{and} \qquad W_t = \omega R + U \sin\psi \tag{1.24}$$

where $U = U_\infty(1-a_{up})$ in the upstream part, and $U = U_\infty(1-a_{dw})(1-2a_{up})$ in the downwind part (induction factors a are later described in Section 1.2.4). It can be noted that the contributions to relative velocity imply minimum and maximum values respectively around $\theta = 0$ and $\theta = 2\pi$, where in the case with negligible expansion, U_∞ and W are aligned.

Local Flow Reynolds Number

The local flow Reynolds number at the blade is defined as

$$Re = \frac{Wc}{\nu} \tag{1.25}$$

with ν the kinematic viscosity assumed to be constant and equal to $15 \cdot 10^{-6}$ $[m^2/s]$.

Angle of Attack

The angle of attack α is the angle between the cord of the blade and the relative velocity W, with positive angle of attacks defined for a relative wind velocity incoming from the outside of the cylinder swept by the blade :

$$\alpha = \arctan\left(\frac{-U\cos\psi}{U\sin\psi + \omega R}\right) = \arctan\left(\frac{W_n}{W_t}\right) \tag{1.26}$$

Angles of attack close to zero are encountered around $\theta = 0$ and $\theta = 2\pi$, due to the alignment between W and U_∞ as mentioned previously. In addition, maximum values are observed around $\theta = \pi/2$ and $\theta = 3\pi/2$ where incident and relative wind speeds are perpendicular to each other.

Forces Applied on the Blade

Due to the incoming flow, each blade develops lift L and drag D forces (see Figure 1.5), which are obtained from aerofoil data for lift and drag coefficients, C_l and C_d, depending on the local angle of attack, α, and local flow Reynolds number, Re. These forces are accounted for per unit of blade height H:

$$\begin{aligned} L &= 0.5\,\rho\,c\,C_l\,W^2 \qquad [N/m] \\ D &= 0.5\,\rho\,c\,C_d\,W^2 \qquad [N/m] \end{aligned} \tag{1.27}$$

from which we can obtain the normal and tangential components of the force acting on the blade:

$$\begin{aligned} F_n &= L\cos(\alpha) + D\sin(\alpha) = 0.5\,\rho\,c\,C_n\,W^2 \qquad [N/m] \\ F_t &= L\sin(\alpha) - D\cos(\alpha) = 0.5\,\rho\,c\,C_t\,W^2 \qquad [N/m] \end{aligned} \tag{1.28}$$

leading to the expression for adimensional normal and tangential forces coefficients:

$$\begin{aligned} C_n &= C_l\cos(\alpha) + C_d\sin(\alpha) \\ C_t &= C_l\sin(\alpha) - C_d\cos(\alpha) \end{aligned} \tag{1.29}$$

The tangential force component is responsible for the torque generated by the rotor, and the quality of the model to represent tangential forces will infer its ability to compute valid values for torque and power.

Another important force is the thrust in the stream tube direction F_x^{blade}:

$$F_x^{blade} = F_n\cos\psi + F_t\sin\psi \qquad [N/m] \tag{1.30}$$

1.2.3 Aerofoil Data

Aerofoil tables provide lift and drag coefficient for a range of angle of attack of a given blade profile at a given flow Reynolds number. Initial aerofoil tables for the small VAWT comparison are taken directly from the reference simulations (originating from Sandia Labs. [18]). The up-scaled 5MWe version of the wind turbine faces higher local Reynolds number and therefore the tables provided by Sandia Laboratories are used [15].

It is worth noting that these tables provide data for angles of attack past static stall angle. Caution is therefore required as the real behaviour of a stalled wing is governed by turbulence and dynamic effects, and the results provided by VAWTs at low tip speed ratio facing high angles of attack are unlikely to provide adequate results.

1.2.4 Induction Factors

Induction factors a represent the decrease in axial velocity undergone by a fluid passing through an actuator surface which retrieves work from the fluid. In the studied case, upstream and downstream actuator surface induction factors of a given stream tube can be expressed as:

$$\begin{aligned} a_{up} &= \frac{U_\infty - U_{up}}{U_\infty} \\ a_{dw} &= \frac{U_{rec} - U_{dw}}{U_{rec}} \end{aligned} \tag{1.31}$$

It is assumed that ambient pressure recovers in the wake between the up and downstream actuator surfaces, leading to the wind velocity U_{rec} :

$$U_{rec} = U_\infty(1 - 2a_{up}) \tag{1.32}$$

The induction factor computation for each actuator surface requires two functions. The first one is obtained from momentum balance and corresponds to the force applied in the windward direction by the fluid on a given actuator surface. The second one is obtained from blade element momentum theory.

From momentum theory, we can express the thrust coefficient, C_T, as following :

$$C_T^{mom} = \frac{F_x^{mom}}{0.5\,\rho A_{as}\,U_\infty^2} = \frac{2\rho A_{as} U_\infty^2\, a(1-a)}{0.5\,\rho\,A_{as}\,U_\infty^2} = 4a(1-a) \qquad [-] \tag{1.33}$$

with $A_{as} = R|\cos(\psi)|\delta\psi$, the area of an actuator surface per stream tube height, and U_∞ replaced by U_{rec} for the downwind actuator surface. For heavily loaded blades, an induction factor $a_{up} > 0.5$ would imply a negative wind speed (see Eq. 1.32), therefore Glauert's empirical correction is applied :

$$C_T^{mom} = \begin{cases} 4a(1-a) & \text{if } a \le a_{lim} \\ 1.7 - 4(\sqrt{1.7}-1)(1-a) & \text{if } a > a_{lim} \end{cases} \tag{1.34}$$

where it is assumed that the thrust coefficient reaches 1.7 when the induction factor approaches 1, and $a_{lim} = 1 - 0.5\sqrt{1.7} \approx 0.35$.

Blade elements participation to thrust can be taken into account through a second expression for the thrust coefficient C_T :

$$C_T^{blade} = \frac{-\overline{F_x^{blade}}}{0.5\,\rho\,c\,U_\infty^2} = \frac{-\left(\frac{B\delta\psi}{2\pi}\right) F_x^{blade}}{0.5\,\rho\,c\,U_\infty^2} \qquad [-] \tag{1.35}$$

where the minus sign is present to account for the reaction of the blade on the flow, $\frac{B\delta\psi}{2\pi}$ is added to take the average of the blade effect on a single actuator surface, and the thrust F_x^{blade} is the same as derived in Section 1.2.2.

The two expressions of thrust on the actuator surface F_x^{mom} and $-\overline{F_x^{blade}}$ must be equal and from Equations 1.33 to 1.35, it is now possible to solve numerically the induction factor for each actuator disk:

$$\frac{Bc}{2R}\frac{1}{\pi|\cos\psi|}\frac{W^2}{U_\infty^2}(-C_n\cos\psi - C_t\sin\psi) = \begin{cases} 4a(1-a) & \text{if } a \le a_{lim} \\ 1.7 - 4(\sqrt{1.7}-1)(1-a) & \text{if } a > a_{lim} \end{cases} \tag{1.36}$$

1.2.5 Power and Torque

Once the induction factor of an actuator surface is known, it is possible to compute the angle of attack and the relative velocity over the trajectory of each blade, and at this point the tangential forces F_t applied on the blade can be computed. This allows for the computation of torque and mechanical power generated by the wind turbine.

The instantaneous torque generated by a blade per rotor height is :

$$T_b(\theta) = F_t(\theta)\;R \qquad [Nm/m] \tag{1.37}$$

The total torque generated by the B blades per rotor height corresponds to :

$$T = B\frac{1}{2\pi}\int_0^{2\pi} T_b(\theta)\mathrm{d}\theta \qquad [Nm/m] \tag{1.38}$$

Finally, the expression for the power generated per rotor height is:

$$P = \omega T = B \frac{\omega R}{2\pi} \int_0^{2\pi} F_t(\theta) \mathrm{d}\theta \qquad [W/m] \tag{1.39}$$

1.3 Model Validation

This section begins with a convergence analysis realised in order to determine the best trade-off between computational time and results accuracy. Then, the results are compared to those of the Vortex Particle-Mesh Method applied to the case of a small vertical axis wind turbine which recently provided very adequate results [17].

1.3.1 Convergence of the Method

As it is shown on Figures 1.6 and 1.7, the method converges when the number of points on the circumference (and therefore the number of stream tubes) increases. This can be attributed to the smaller angle variations between successive stream tubes impeding a better accordance with the small angles assumptions previously stated.

A good trade-off between converged results and computational time is reached starting from $N_t = 40$ (for more details, please refer to Appendix A.1). The method being computationally affordable, the following section will be using eighty points on the circumference.

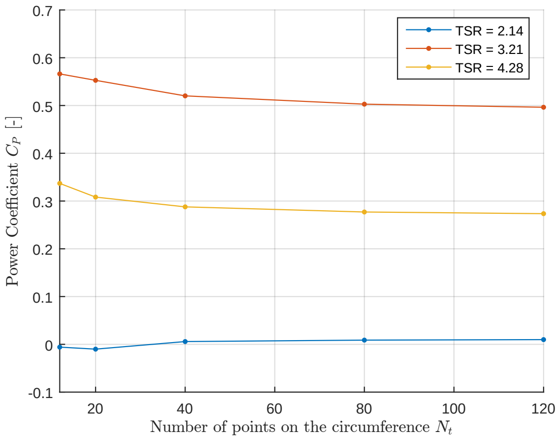

Figure 1.6: Power coefficient evolution with the number of calculation points

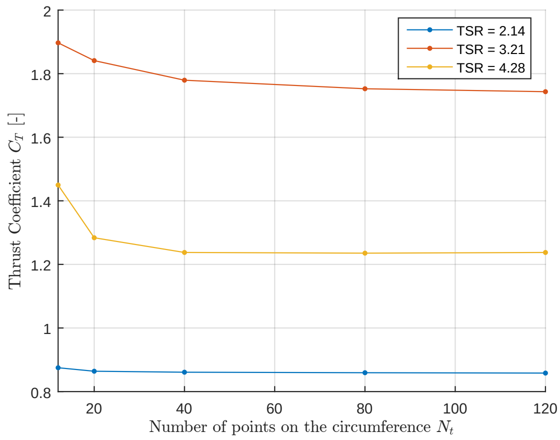

Figure 1.7: Thrust coefficient evolution with the number of calculation points

1.3.2 Vortex Particle-Mesh Method

The Vortex Particle-Mesh method (VPM) is a complex method requiring large parallel computation resources, which provides excellent results, and that has been used to model VAWT aerodynamics [17].

The vorticity-velocity formulation of the Navier-Stokes equations is treated in a dual manner by particles for the advection, and by a mesh to evaluate the differential operators and the fast Poisson solvers. Their communication is managed through high order interpolation. Then, the sources of vorticity are accounted for through an immersed lifting line approach, based on airfoil polars [16]. Such a model allows for a detailed capture of the wake development.

Results for a studied VAWT are compared to those of the DMST in the next section.

1.3.3 Comparison Between VPM and DMST Results

The wind turbine parameters used with both methods are reported on Table 1.1. The comparison between VPM and DMST results required the usage of DMST with stream tubes expansion (as explained before), as well as DMST without accounting for stream tubes expansion. The latter is obtained when expansion coefficients χ_{up} and χ_{dw} in Eq 1.22 are both set to 1 in order to prevent the expansion from occurring, while all other parts of the model are kept unchanged in order to keep an adjustable code.

Figure 1.8 presents the profiles of angle of attack, as well as normal and tangential forces developed by a blade over a revolution. These forces per unit of blade height are non-dimensionalized with respect to the blade chord c and the dynamic pressure $q_0 = 1/2\rho U_\infty^2$. It emerges from these figures, that a general agreement for VAWT characteristics appears:

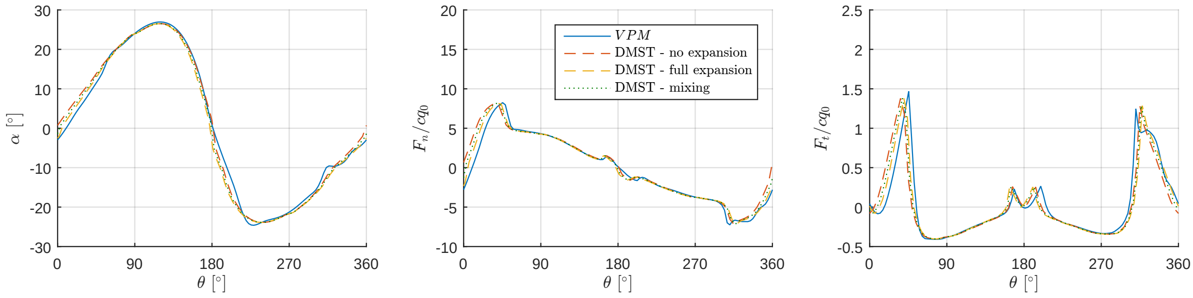

(a) TSR = 2.14

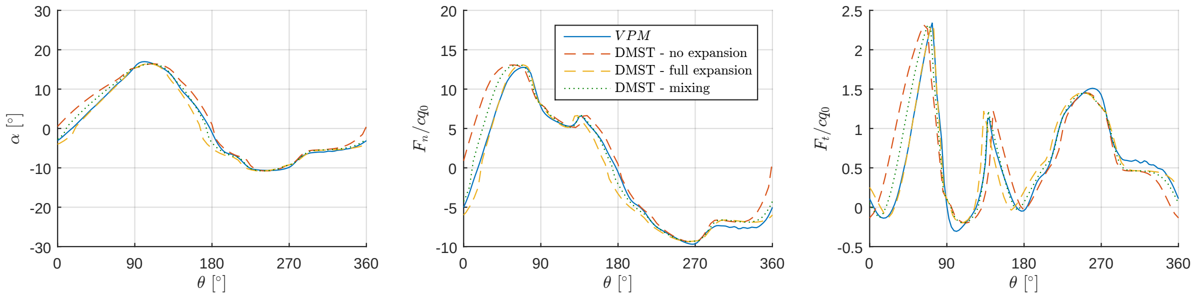

(b) TSR = 3.21

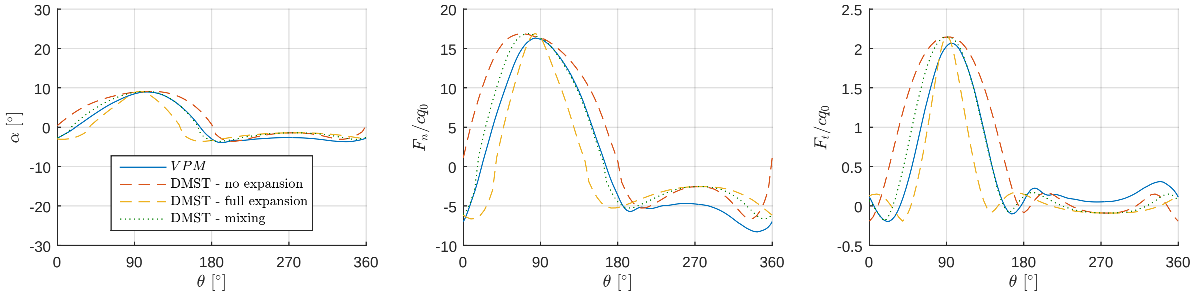

(c) TSR = 4.28

Figure 1.8: Comparison between VPM results at mid-height and DMST results: evolution of the angle of attack α, the normal force coefficient F_n/cq_0, and the tangential force coefficient F_t/cq_0

High angles of attack at low tip speed ratio, due to high normal relative wind speed contribution. The angle of attack curve flattening is observed in the downwind region due to the wind flow slowdown in the downwind part; this effect is moderate at low tip speed ratio, and becomes more important at high tip speed ratio due to a more loaded wind turbine. Maximum and minimum angle of attack values are respectively observed slightly after 90° and before 270° due to the flow expansion. A sharp decrease in tangential force is observed for high angles of attack, due to stalled blades.

The DMST model with stream tubes expansion yields results showing angle of attack profiles which are more contracted at high TSR with regards to the vertical median plane ($90° - 270°$ θ plane), in comparison to VPM results. This causes the wake at high TSR to be narrower due to the reduction in azimuthal span of the forces applied on the flow. This is attributed to an overestimation by the model of the expansion when the wind turbine is heavily loaded. Indeed, the DMST model without accounting for stream tubes expansion provides opposite results, with stretched out angle of attack profiles.

From the previous set of observations, an exploratory analysis has been conducted to mix models with and without expansion in order to fit the results (see Section 1.3.4).

Table 1.1: Reference VAWT parameters

Upstream velocity U_∞	11	[m/s]
Aspect Ratio H/D	1.5	[-]
Rotor height H	4.5	[m]
Rotor diameter D	3	[m]
Blade chord c	0.1725	[m]
Blade number B	3	[-]
Airfoil	NACA 0015	

1.3.4 Exploratory Analysis : Mixing DMST Models With and Without Expansion

As mentioned in Section 1.3.3, the DMST model with stream tubes expansion overestimates their expansion at high TSR. Power and torque coefficients curves (see Figure 1.10) provide an insight on the actual TSR at which the expansion starts being overestimated. The mixing is therefore based on the minimum thrust coefficient value reached for TSRs differing by less than 1% between the DMST models with and without expansion (i.e. in the current case, $C_T \approx 1.6$).

Expansion factors (Equation 1.22) are now redefined in order to limit their expansion with an error function Φ :

$$\begin{aligned} \chi_{u,mixing} &= 1 - \Phi(1 - \chi_u) < 1 \\ \chi_{d,mixing} &= 1 + \Phi(\chi_d - 1) > 1 \end{aligned} \tag{1.40}$$

The error function Φ (Figure 1.9) is optimised with regards to the parameters ε_1 and ε_2 in order to fit the power coefficient obtained from VPM (see Figure 1.10a). The boundaries b_1 and b_2 of the function are set after multiple iterations, to reduce the span of the function. Final parameters values are summarised in Table 1.2.

$$\Phi = b_2 - \frac{(b_2 - b_1)}{2} \left[\text{erf} \left(\frac{TSR - \varepsilon_2}{\varepsilon_1} \right) \right] \tag{1.41}$$

The expansion overestimation from the original model can be observed from the streamlines comparison on Figure 1.11, where the results at high TSR greatly differ from the VPM simulations, whereas the mixing provides a more adequate expansion. It can be noticed from the streamlines that the expansion is not symmetrical with regards to the median plane ($90° - 270°$ plane). This effect is due to blade motion and blade-wake interaction [12].

Finally, it can be observed from Figure 1.8 that the mixing improves the ability of the model to capture angles of attack and loadings. This is confirmed on simulation results :

Figures 1.13 shows horizontal slices of axial velocities at mid-height. They show good agreement as we observe a similar wake decay mechanism, governed by the TSR: at low a TSR of 2.14, the wake is weakened by the stall event, and remains stable. On the other hand a shorter wake is observed for a TSR of 3.21 and 4.28, even showing recirculating flow for the most loaded rotor. Figures 1.12 shows slices of the turbulent kinetic energy (TKE) :

$$\overline{k} = \frac{\overline{u'u'} + \overline{v'v'} + \overline{w'w'}}{2U_{mean,NREL}^2}. \tag{1.42}$$

The generation of TKE corresponds to the smearing of the velocity deficit for TSRs of 3.21 and 4.28. In the case of the most loaded rotor, the recirculation occurring is accompanied by a large production of TKE, which increases the rate of wake velocity smearing. Explaining why we can observe a shorter wake in this case. In the case of TSR of 2.14, the stability of the wake is reflected by the absence of noticeable TKE generation.

Additionally, the mixing provides good adequacy with power and thrust coefficients curves (see Figure 1.10), where it can be observed that the case without expansion highly overestimates the power coefficient at high TSR, while the model with expansion greatly underestimates it. At slow to moderate TSR, the expansion of the stream tubes is small enough to provide similar results.

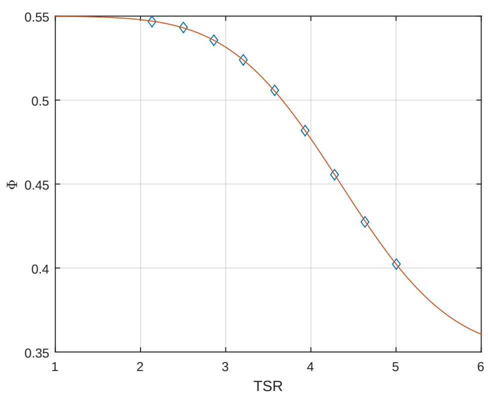

Figure 1.9: Fitting function Φ (◇ : points at which VPM data are available)

Table 1.2: Mixing DMST models parameters

ε_1	1,4407
ε_2	4.3507
b_1	0.35
b_2	0.55

1.4 HAWT Farm Reference

The aim of this thesis is to eventually compare the aerodynamic behaviour and power production between an offshore farm of HAWTs and a farm of VAWTs. In order to do so, the reference HAWT farm results are obtained from M. Moens, currently conducting a PhD thesis at UCL on the study of HAWTs.

The reference HAWT that will be used originates from the "NREL offshore 5 MW baseline wind turbine" defined in a report from the National Renewable Energy Laboratory [19], and is characterised by a rated power of 5 MWe, a hub height of 90m, and a rotor diameter of 126m.

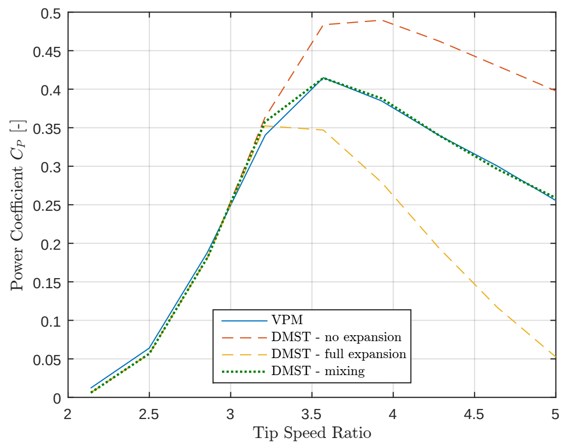

(a) Power coefficient

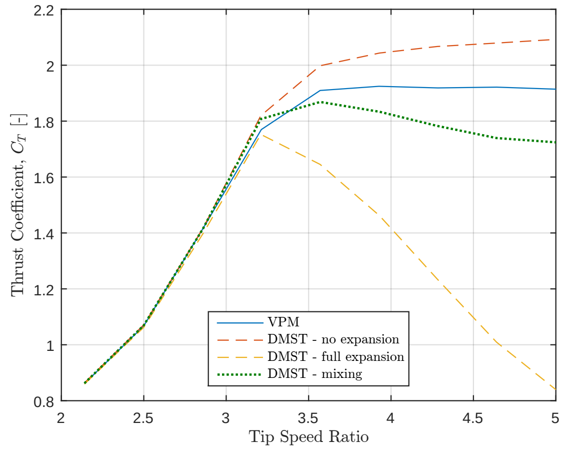

(b) Thrust coefficient

Figure 1.10: Power and thrust coefficients evolution with the tip speed ratio

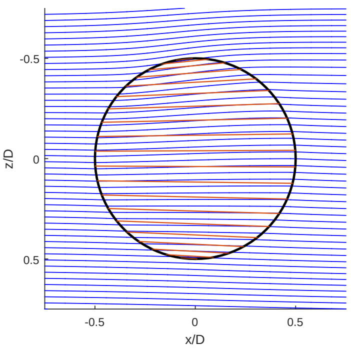

(a) TSR = 2.14, full expansion

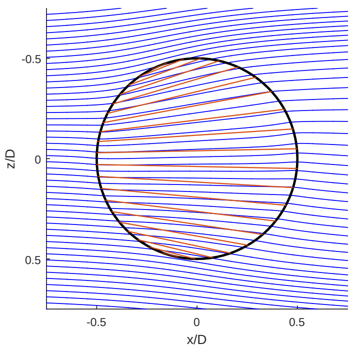

(b) TSR = 3.21, full expansion

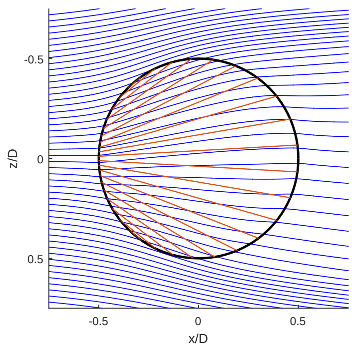

(c) TSR = 4.28, full expansion

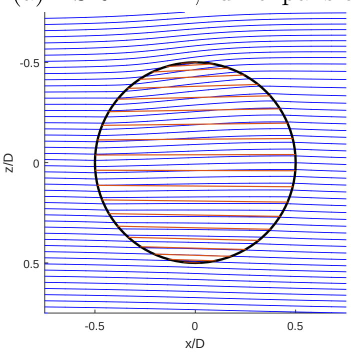

(d) TSR = 2.14, mixing expansion

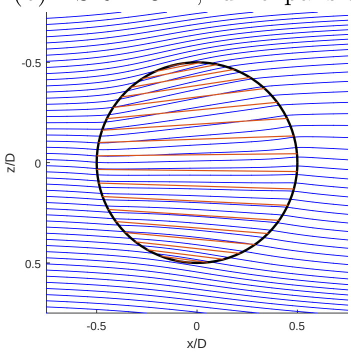

(e) TSR = 3.21, mixing expansion

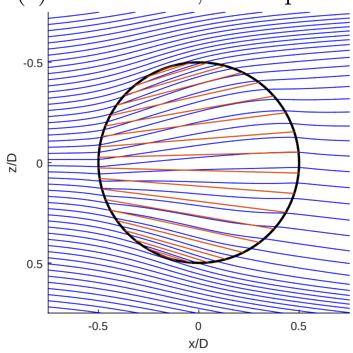

(f) TSR = 4.28, mixing expansion

Figure 1.11: Comparison between stream tubes from the DMST model (orange) and streamlines from VPM simulations (blue)

This HAWT will be denoted *NREL* in the rest of the text.

The considered wind farm layout is composed of three rows of five wind turbines each are aligned with the stream-wise direction. The comparison will be based on a same power density and a same number of wind turbines between the farms, implying the same positioning of the turbines. In order to reach this objective, an up-scaling of the VAWT will be studied in Section 1.5. Furthermore, the *NREL* is provided with information about the rotor dynamics and a controller, therefore a controller scheme will be implemented for the up-scaled VAWT (see Section 1.6.1).

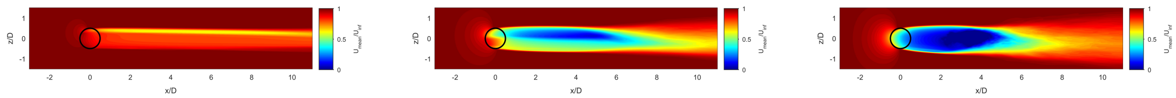

(a) TSR = 2.14, VPM (b) TSR = 3.21, VPM (c) TSR = 4.28, VPM

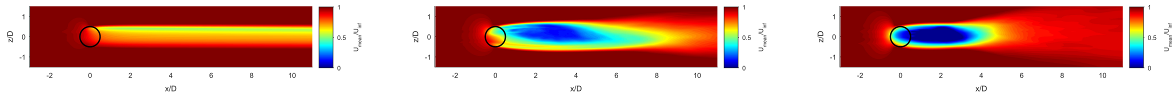

(d) TSR = 2.14, DMST (e) TSR = 3.21, DMST (f) TSR = 4.28, DMST

Figure 1.12: Comparison between mean velocity slices from VPM simulations (up) and from CFD simulations with the DMST model (down)

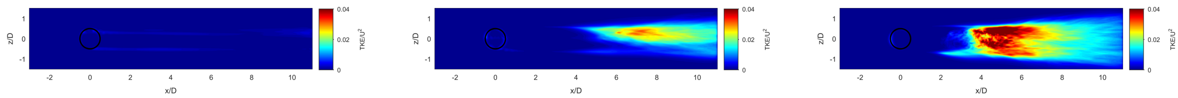

(a) TSR = 2.14, VPM (b) TSR = 3.21, VPM (c) TSR = 4.28, VPM

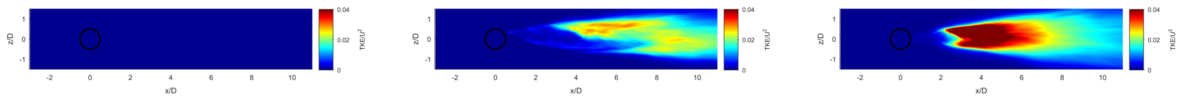

(d) TSR = 2.14, DMST (e) TSR = 3.21, DMST (f) TSR = 4.28, DMST

Figure 1.13: Comparison between turbulent kinetic energy from VPM simulations (up) and from CFD simulations with the DMST model (down)

The following points come directly from the publication M. Moens, et al.[20], and are added here for the sake of completeness.

1.4.1 HAWT Farm Simulation

The approach selected for the HAWT farm simulation needed accuracy, a realistic response of wind turbines and an affordable computation time. It is "based on classical structured mesh CFD, [and] consists in Large Eddy Simulation (LES) on relatively coarse meshes and the use of [a high accuracy] Actuator Disk (AD) model for the wind turbines. [...] The ground effect is taken into account by adding wall models, allowing a representation of the wind shear and turbulence structures for an atmospheric boundary layer under neutral conditions" [20].

Flow Solver - Big Flow

"[The] LES of incompressible turbulent flows [...] is performed using a fourth-order finite differences code developed at UCL, formulated in primitive variables (i.e. in velocity and pressure) and using a structured staggered mesh arrangement. The Navier-Stokes equations, supplemented by a subgrid scale (SGS) model, are solved using a fractional-step method with the delta form for the pressure and are discretized in space using a fourth order finite difference scheme. The Poisson equation for the pressure is solved using a multigrid solver [...]. The time integration is carried out using an explicit second-order Adams-Bashforth scheme. [...] The wind turbine effect is added through external body forces (per volume) acting on the flow [discussed below].

x is the stream-wise direction, y, the vertical direction and z the span-wise direction. Instantaneous velocities are imposed at the inlet boundary [see below] and a convective boundary condition is applied at the outflow. Periodic boundary conditions are imposed in the z direction

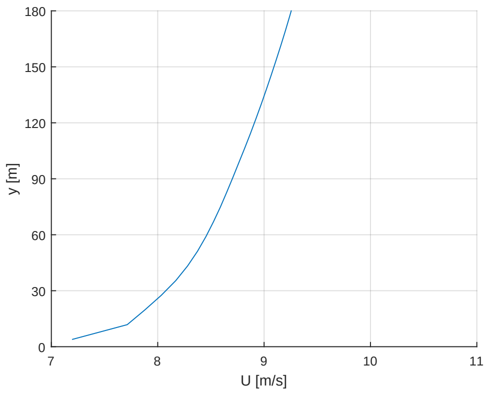

Figure 1.14: Atmospheric boundary layer profile – only the lower part at the scale of the wind turbines is shown

and no-through flow is enforced at the top. At the bottom, wall effects are included using a wall model, which is required for simulations at high Reynolds number, as in ABL simulations. A wall stress model for a rough wall is here applied, to compute the surface shear stress as a function of the LES velocity field at the third vertical grid point" [20].

Wind turbine model

"The [HAWT] is accounted for through an AD: with this model, the actual geometry of the rotor blades is replaced by body force terms acting over the surface swept by the rotor. [...] The local disk velocities are modified using a tip-loss factor in order to account for the finite number of blades. [...] This model, coupled to LES, has been verified through a comparison with higher fidelity results, produced using a Vortex Particle-Mesh method with immersed lifting lines" [20].

Turbulence generation

"The code can handle turbulent inflow conditions in two fashions: using precursor LES results or using turbulent fluctuations pre-generated with the Mann algorithm and over-imposed to a chosen velocity profile at the inlet. For wind farm simulations, the first approach is the most appropriate: it involves running a prior simulation of a turbulent boundary layer flow without wind turbines, [...] later used as inflow for simulations with wind turbines" [20].

1.4.2 VAWT Farm

The VAWT farm follows the same principles and topology as the HAWT farm, with the most adverse wind origin scenario for the wind turbines. As mentioned, the same power density has been set to compare the two farms.

1.5 VAWT Upscaling

This section describes the path followed to up-scale the VAWT studied in Section 1.3, in order to generate a 5MWe geometry that will later be used in wind farm simulations.

1.5.1 First iteration round

In a first up-scaling attempt, geometric and aerodynamic similarities are taken into account : the number of blades, their profile, as well as the wind turbine solidity and tip speed (and thus the tip speed ratio as well) are conserved, in order to obtain similar flow geometry [21, 22].

The selected up-scaling parameter is the rotor swept area $A = 2\,R\,H$, with reference to the Darrieus 5MW DeepWind baseline swept area A_{DW}[23]. The following scaling factor enables lengths to be proportional to the scaling factor sf.

$$sf = \sqrt{\frac{A_{DW}}{A}} = 29.81 \tag{1.43}$$

Therefore, we have for the up-scaled VAWT :

$$\begin{aligned} R_{sc} &= R\ sf \\ H_{sc} &= H\ sf \\ c_{sc} &= c\ sf \end{aligned} \tag{1.44}$$

This first iteration provides a good approximation of the desired up-scaled geometry, yet it is now necessary to tune it finely in order to select a valid $5\,MWe$ option comparable to the *NREL*.

1.5.2 Second iteration round and discussion

The VAWT geometry to choose for wind farm simulations can be approached in multiple manners. Hereafter are discussed the main points which lead to the final up-scaled VAWT geometry (Table 1.3), and in order to obtain the final geometry, this process is realised iteratively.

Ground Clearance

The ground clearance refers to the altitude of the blades' lowest extremity. Below are listed the considered choices :

- Same ground clearance for VAWT and HAWT;
- Set the VAWT's mid-height at the same altitude as the reference NREL HAWT (90m);
- Lower clearance for the VAWT, as proposed in the DeepWind 5MW baseline (15m).

The first possibility allows for a similar vertical positioning of the rotor for the VAWT and the reference HAWT, yet it is less realistic as VAWTs are generally installed lower than HAWT. The second one provides a smaller clearance as well as a similar vertical positioning between HAWT and VAWT. The last possibility is more representative of what the implementation of a real size rotor would resemble, experiencing lower wind speed at the bottom due to atmospheric boundary layer. This latter choice has been chosen for its credibility, yet this is the very limit authorised by the CFD simulations, which require clearance for the law of the wall.

Rotor Height

While conserving an aspect ratio of 1.5, the rotor height will be the determinant factor for the rotor geometry. Here as well, several options are available while comparing VAWT and HAWT :

- Conserving the integral $\int U(y)^3 \mathrm{d}A$, taking into account the wind speed profile along the altitude due to an atmospheric boundary layer;
- Conserving the value $(C_{P,max}\,A)$;
- Keeping an equal swept area A.

The first choice ensures comparable results regarding the fact that besides turbulence, both VAWT and HAWT would be facing the same wind power, the second one would allow for the same potential power production while taking into account the rotor geometry, and the last one allows for geometrically comparable wind turbines although VAWT would be expected to have a larger swept area for the same power production.

Provided that it has been decided previously to position the VAWT lower than the HAWT, the first possibility here would allow for a comparable power production.

Power Coefficient

The DMST model as it is now overestimates the power coefficient C_P of VAWTs, therefore multiple choices are possible regarding the TSR at which the control will have to aim.

- VAWT $C_{P,max}$;
- HAWT $C_{P,max}$;
- Power coefficient inferior to VAWT $C_{P,max}$.

The first possibility corresponds to the operating mode of HAWT for wind speeds below the rated value, but currently considered VAWT geometry have a power coefficient of about 0.55. The second possibility would allow following HAWT's behaviour whose modeled $C_{P,max}$ is expected to be in the vicinity of 0.54. Furthermore, lowering the power coefficient by increasing the tip speed ratio would imply selecting an operating range where maximum angle of attack encountered are lower and thus moving away from operating range dominated by dynamic stall. Finally, the third possibility could be to choose a power coefficient from literature, or VPM simulations. This latter possibility would allow avoiding high angles of attack as well, but a correct value would be difficult to determine and justify, therefore discarding this option.

Discussion

Each point mentioned previously enabled the analysis to be pursued :

The fitting of the integral $\int U(y)^3 \mathrm{d}A$ for a VAWT's height of 138m returns similar results for the three considered ground clearance (respectively 2.5%, 0.8%, and 1.1% relative error on the integral). This height provides a superior swept area with regards to the HAWT, yet with an increase limited to 1.8%.

Simulations of HAWT in uniform flow provide a $C_{P,max}$ of 0.54, below rated power (region 2). DMST model predicts a $C_{P,max}$ of 0.55 for an upscaled VAWT of 138m, which is slightly higher. Given that VAWT are not expected to have a higher C_P than HAWT, the operating point of the VAWT model will be lowered to a $C_{P,max}$ of 0.54 in the region 2 at a higher TSR, in order to keep coherence with the compared HAWT. Finally, it results from this combination that the three announced possibilities for the rotor height return similar results for a ground clearance of 15m.

Mixing Models with and without expansion

Due to the shifting of C_P and C_T curves towards lower tip speed ratios, it is necessary to adapt the fitting function Φ used earlier in order to find a compromise between models with and without expansion. Indeed, the range of local Reynold's numbers encountered being one order of magnitude higher than for the small wind turbine, a more adapted airfoil data set is used.

The adaptation of the Φ-curve starts with the choice of two reference tip speed ratios : the TSR corresponding to $C_{P,max}$ for the model with expansion, and the TSR corresponding to the reference C_T (see Section 1.3.4). The fitting function's parameters ε_1 and ε_2 are then fitted in order to shift the function towards lower TSR, and slightly stretch it out (see Figure 1.15).

Results

The parameters of the up-scaled VAWT are summarised in Table 1.3. It can be observed that its power coefficient curve (Figure 1.16a) rises beyond $C_P = 0.5$, because the selected model does not account for dynamic stall which would have limited the maximum value of the curve. The thrust coefficient curve (Figure 1.16b) is also shifted towards lower TSR, while keeping a maximum value in the same range as the small VAWT.

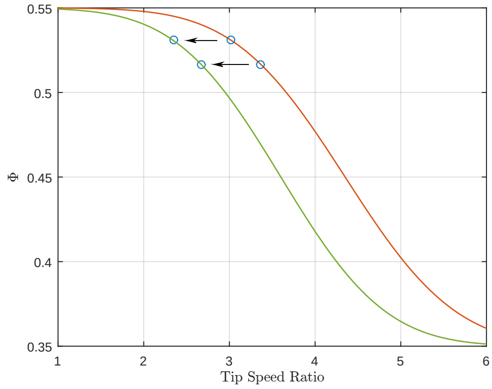

Figure 1.15: Fitting function Φ for the up-scaled VAWT (○ : reference points; orange : original geometry; green : up-scaled geometry)

Table 1.3: Upscaled VAWT parameters

Scaling factor sf	30.67	[-]
Aspect Ratio $A_R = H/D$	1.5	[-]
Height H	138	[m]
Diameter D	92	[m]
Chord c	5.29	[m]
Blade number B	3	[-]
Airfoil	NACA 0015	

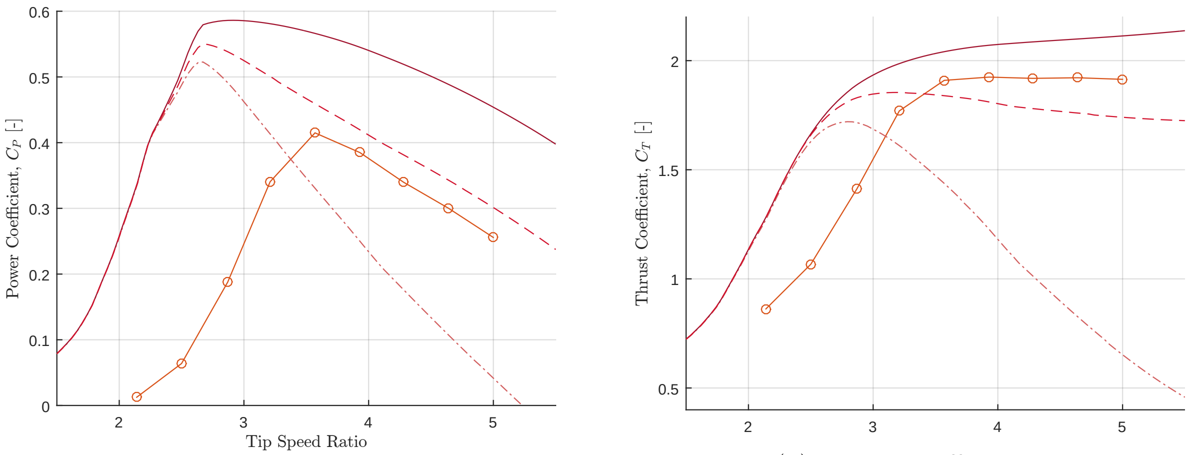

(a) Power coefficient

(b) Thrust coefficient

Figure 1.16: Power and thrust coefficients evolution with the tip speed ratio for the upscaled VAWT (○ : VPM data; ·— : DMST with expansion; — : DMST without expansion; —— : mixing)

1.6 Control of the VAWT

In order for the one-way coupling to be performed between mechanical and electro-mechanical investigations in this thesis, a common strategy must be established. This section describes the control scheme used in VAWT's simulations in order to retrieve the maximum mechanical power out of the wind resource, also called maximum power point tracking (MPPT). From the results of previous sections, the target steady-state power response as a function of wind speed can be established (see Figure 1.17). It is worth noting that the *NREL* reference response will differ from the used HAWT model, which provides a higher maximum power coefficient with the actuator disk model.

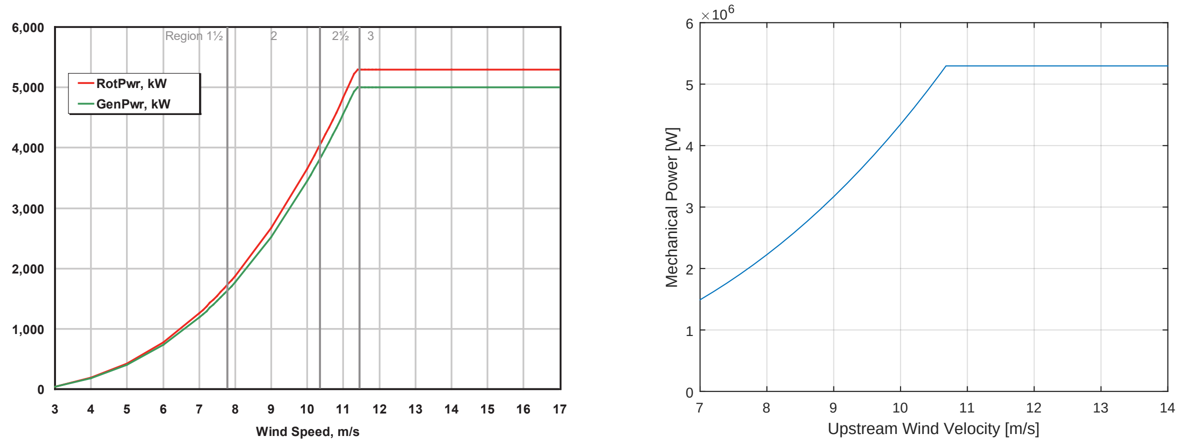

(a) NREL 5MWe (adapted from [19])

(b) Up-scaled VAWT

Figure 1.17: Steady-state power response as a function of wind speed

The variation of the C_P-TSR curve (Figure 1.16a) with the power production point is assumed to be located at a constant TSR. Below rated power production, the control system will therefore aim at a fixed TSR_{opt} until the rated power production is reached. Once it is reached, the aero-dynamical efficiency of the wind turbine is to be degraded if one wishes to keep a constant mechanical power production. Other possible strategies are described in Section 2.2.

1.6.1 Torque-based Rotation Speed Control

The current control of the rotation speed is performed on torque (based on [32]). Indeed, the time variation of the rotation speed ω depends on mechanical and generator torques (respectively noted T_m and T_{gen}) :

$$\frac{\mathrm{d}\omega}{\mathrm{d}t} = \frac{T_m - T_{gen}}{J} \tag{1.45}$$

where J is the inertia of the rotor, assumed to be $4.98 \cdot kg\, m^2$ - taking the DeepWind 5MW baseline as reference [24]. The value of mechanical torque is computed from mechanical power and rotational speed at the previous step :

$$T_m = \frac{P_m}{\omega} \tag{1.46}$$

The optimal rotation speed at a given instant, ω^*, depends on the upstream conditions U_∞, already required by the DMST model and therefore made available. From the definition of TSR (Equation 1.14), we have :

$$\omega^* = \frac{TSR_{opt} U_\infty}{R} \tag{1.47}$$

In the case of VAWT simulations, the average U_∞ is measured $1.25H$ ahead of the rotor center (for more details, please refer to Section 1.7), and averaged over the swept area in order to provide a single value $\bar{U}_\infty$ to the controller.

The instantaneous rotation speed is subject tot rapid wind variations (e.g. from wind gusts upfront wind turbine's wake oscillations), and its value is therefore smoothed via a target rotational speed ω_{target} before being fed to the control scheme. The variation $\mathrm{d}\omega_{target}$ is computed as following at each time step :

$$\mathrm{d}\omega_{target} = -\frac{\omega_{target} - \omega^*}{\tau}\mathrm{d}t \tag{1.48}$$

with $\mathrm{d}t$ the time step of the simulation, and τ a chosen time constant for the negative exponential smoothing. In the studied case, a τ value of 15 seconds provided good results.

At this point, ω_{target} is now used in a proportional-integral (PI) control scheme (developed in Section 1.6.1). The rotation speed error between target and effective rotation speed is :

$$e = \omega_{target} - \omega \tag{1.49}$$

used in the computation of T_{gen} :

$$T_{gen} = -\left(K_P + K_I \int_0^t e \, \mathrm{d}t\right) \tag{1.50}$$

Finally, the effective rotation speed variation can be computed :

$$\mathrm{d}\omega = \frac{T_m - T_{gen}}{J}\mathrm{d}t \tag{1.51}$$

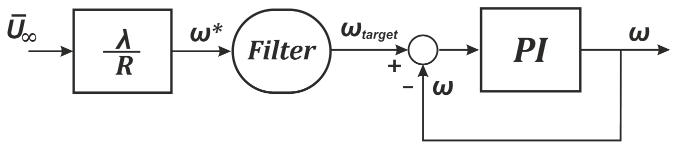

Figure 1.18: Control loop of the mechanical maximum power point tracking

In order to implement the control of the MPPT as shown on Figure 1.18, the Swing Equation 1.45 is tranformed into the Laplace domain:

$$J\omega s = T_m - T_e$$

leading to open loop transfer function $\frac{1}{Js}$ In order to obtain a zero steady-state error, a PI controller is chose, its transfer function is:

$$K_P + \frac{K_I}{s}$$

The resulting transfer function is:

$$T(s) = \frac{(K_P + \frac{K_I}{s})\frac{1}{Js}}{1 + (K_P + \frac{K_I}{s})\frac{1}{Js}} = \frac{(K_P s + K_I)/J}{s^2 + \frac{K_P}{J}s + \frac{K_I}{J}}$$

It is second order transfer function with denominator of generic form: $s^2 + 2\zeta\omega_n s + \omega_n^2$. This enables to find the parameters of the controller:

$$K_P = 2\zeta\omega_n J$$

$$K_I = \omega_n^2 J$$

ω_n is the natural pulsation and *zeta* is the damping ratio of the controller, chosen in order to have an appropriate step response.

1.7 CFD Implementation[2]

This section explains how the DMST model is implemented in the flow solver mentioned previously (see Section 1.4.1) in order to compute flow simulations of VAWTs and VAWT farms. Indeed, the original routine is run with MATLAB and requires information about the VAWT geometry, the upstream velocity, and the tip speed ratio at which it operates. Therefore this routine requires to be translated to a *C* code in order to interact with the flow solver where each wind turbine is treated as a separate structure, whose parameters' evolution depends on the flow simulation.

[2]The initial implementation was made by [5]

1.7.1 Upstream Velocity

The VAWT geometry is defined for the whole simulation, and the operating point is either computed by the controller, or set to a given TSR. The last information required for the DMST model to perform is the upstream velocity ahead of the rotor. In order to account for upstream wind speed variation along the vertical axis (e.g. because of an atmospheric boundary layer, wind turbulence), the wind flow is treated by taking several vertical slices separately. For each of these slices, the average speed is computed from a plane ahead of the rotor. The distance at which the speed is measured must be large enough to avoid slower velocities induced by the rotor, yet not too much in order to avoid accounting too early for the effects of the previous wind turbine's wake if there is any or to avoid anticipation from the wind turbine with regards to the wind variations. A trade-off value must be selected to compose with the previous effects. Then, each of the given speed is then treated in a different call to the DMST model sub-routine.

1.7.2 Force Distribution

From an upstream velocity value, the DMST model returns the distribution of normal and tangential loadings per rotor height, F_n and F_t. These forces are then projected in the coordinates of the solver and applied to a circle representing the rotor cross-section.

The DMST model on its own does not account for vertical variations of the loadings along the axis of the turbine as it assumes a single upstream velocity. In order to account for upstream wind vertical variations, the results of the DMST are applied by taking into account their vertical distribution.

The flow solver requires the force application to be distributed locally in order to avoid discontinuities that would result from the direct addition of forces on the circle representing the rotor's section.

1.8 Performance Analysis

1.8.1 Farm Results

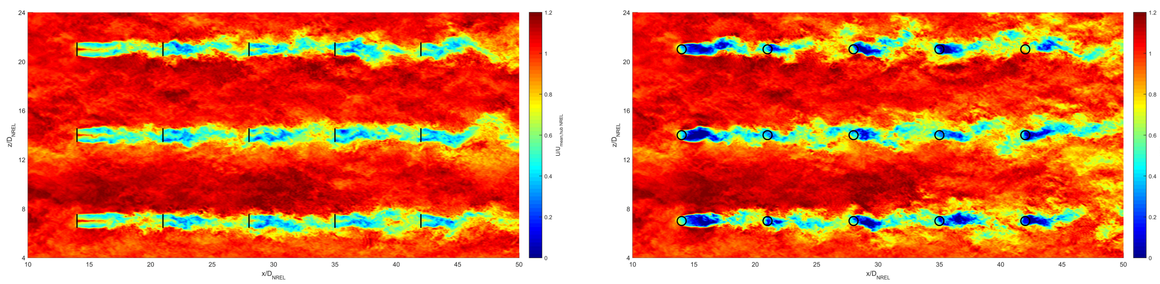

(a) HAWT (b) VAWT

Figure 1.19: Instantaneous stream-wise velocity at *NREL* hub-height

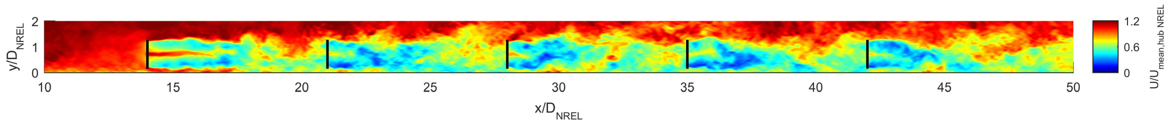

(a) HAWT

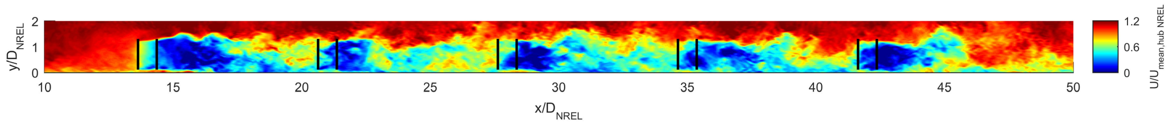

(b) VAWT

Figure 1.20: Instantaneous stream-wise velocity at $z = 7D_{NREL}$ (first row)

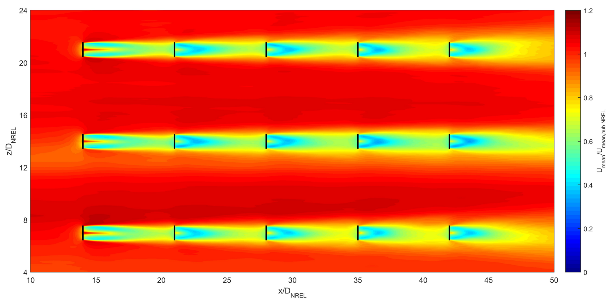

(a) HAWT

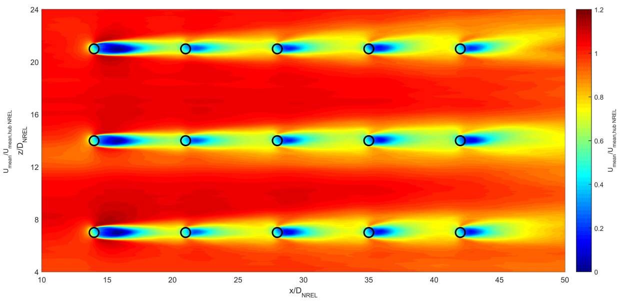

(b) VAWT

Figure 1.21: Mean stream-wise velocity at $NREL$ hub-height

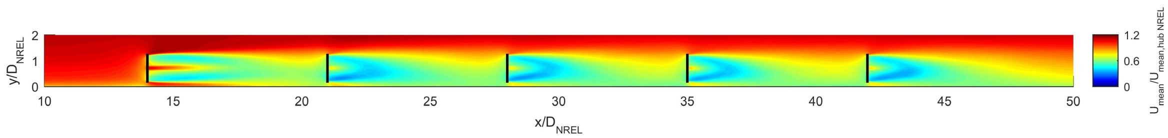

(a) HAWT

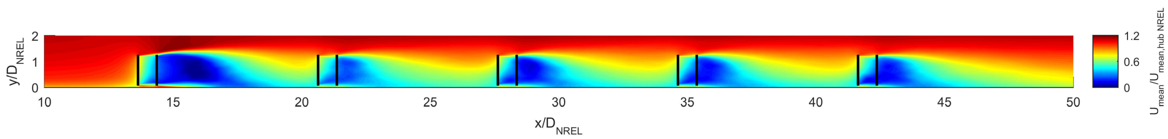

(b) VAWT

Figure 1.22: Mean stream-wise velocity at $z = 7D_{NREL}$ (first row)

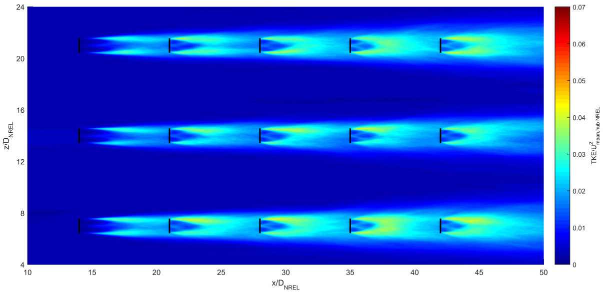

(a) HAWT

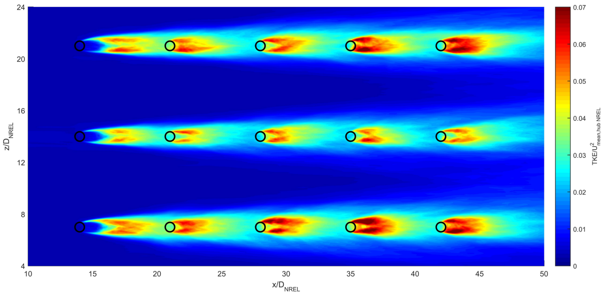

(b) VAWT

Figure 1.23: Turbulent kinetic energy at *NREL* hub-height

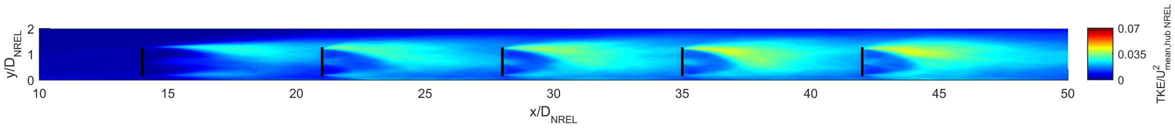

(a) HAWT

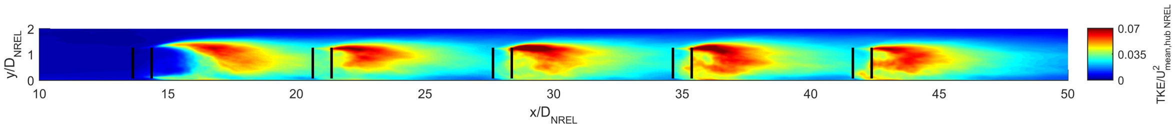

(b) VAWT

Figure 1.24: Turbulent kinetic energy at $z = 7D_{NREL}$ (first row)

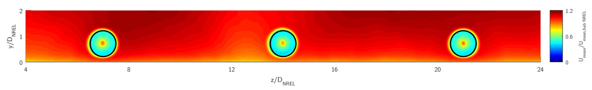

(a) HAWT

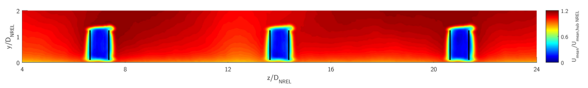

(b) VAWT

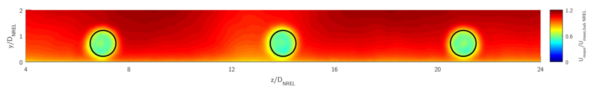

(c) HAWT

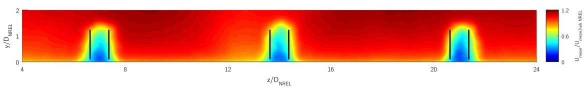

(d) VAWT

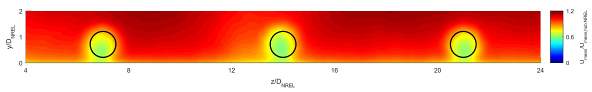

(e) HAWT

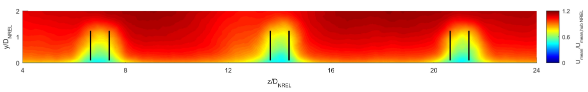

(f) VAWT

Figure 1.25: Mean streamwise velocity at $1D_{NREL}$, $3.5D_{NREL}$, $6D_{NREL}$ after the first wind turbine line

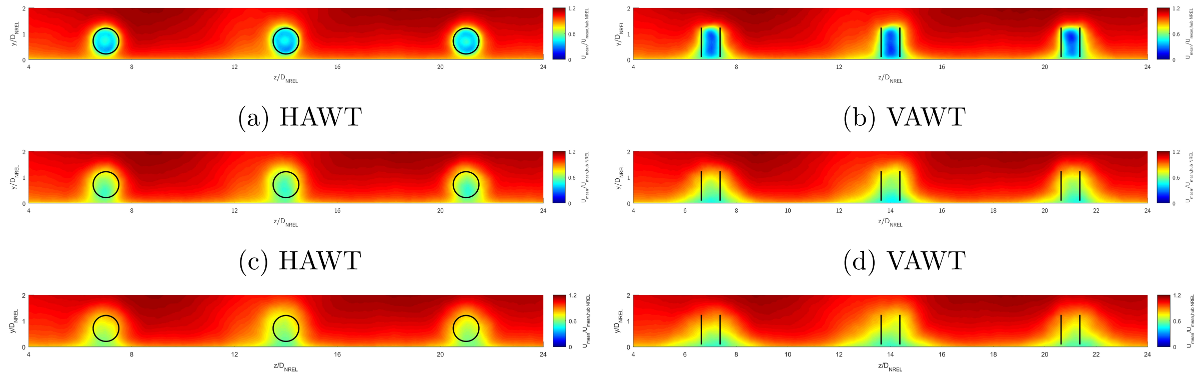

(a) HAWT (b) VAWT

(c) HAWT (d) VAWT

(e) HAWT (f) VAWT

Figure 1.26: Mean streamwise velocity at $1D_{NREL}$, $3.5D_{NREL}$, $6D_{NREL}$ after the second wind turbine line

Figures presented in this section show in parallel the behaviour of HAWTs and VAWTs in a farm configuration, arranged similarly on the same domain size and facing the same wind flow with atmospheric boundary layer and turbulence. This domain's dimension are : $52D_{NREL} \times 8D_{NREL} \times 28D_{NREL}$, corresponding to x, the stream-wise direction, y, parallel to the VAWT axis, and z, cross-stream and perpendicular to the VAWT axis. The differences in flow evolution and wake are being investigated, as well as the power production from each farm.

Figure 1.19 shows horizontal slices of axial velocities at *NREL*'s hub height (90m) for both farms. The velocity scale is non-dimensionalized by using the axial velocity from the ABL at *NREL*'s hub height. Figure 1.20 shows vertical slices of axial velocities located at $z/D = 7$ (i.e. passing through the centres of the first row's wind turbines). HAWT and VAWT slices were not taken at the same instant in the simulations, which means that they are not subject to exactly the same upstream flow. These instantaneous velocity slices show a VAWT farm having a more complex impact on the air flow than its HAWT counterpart. Indeed, recirculation can even be observed at the beginning of the wake, close to the turbines. Yet, these slices also indicate that the VAWT's wake decays rapidly to reach a state comparable to HAWT's before approaching the next downstream wind turbine line.

Figures Figure 1.21 and 1.22 depict slices taken at the same location as previously, for non-dimensionalized mean axial speed. The average is taken on both cases over the equivalent of slightly less than $(2 \times 52D/U_{mean,NREL})$. These mean stream-wise slices show that, on average, the flow tends to recover a similar stream-wise speed before hitting the next line of rotors. The vertically asymmetrical shape of the wake can be observed, indicating performances hindered by the low vertical clearance allowed to VAWTs.

Figures 1.23 and 1.24 show slices of the turbulent kinetic energy (TKE)

$$\overline{k} = \frac{\overline{u'u'} + \overline{v'v'} + \overline{w'w'}}{2U^2_{mean,NREL}}. \tag{1.52}$$

They depict an air flow generating much more turbulence in the case of the VAWT farm, providing insights at the turbulent state of the wake. Besides, we can notice that the generation of TKE coincides with the smearing of velocity deficit. This can be observed for VAWTs and HAWTs, yet at a higher rate for VAWTs, which eventually allows both of them to provide the same wind conditions to the next downwind wind turbines. Indeed, the observed back-flow is accompanied by the high production of TKE, accelerating the rate of wake velocity smearing.

Then, Figures 1.25 and 1.26 presenting slices of the mean stream-wise velocity following the first and second lines of wind turbines appear to confirm that even though there is a large speed decrease right after VAWT rotors, the wake decays rapidly and starts showing a similar behaviour between HAWTs and VAWTs before meeting the next line. The combination of slices of axial velocity show a much stronger wake in the case of VAWTs in comparison to HAWTs. Moreover, the slices associated to the first line's wake show more clearly the stall-generated structures that are advected along the wake. Their impact on the second line can be noticed on the mechanical power generated (see Figure 1.27): while the fraction of average power generated by HAWTs on the second line drops by 55% with regards to the first line and appears to stabilize in the next lines to a slightly lower fraction, the percentage drop on the second line of VAWTs appears to be the same as for HAWTs, but then the third rotor line reaches better performances than the second, to a value that seems stabilized for the next lines.

Finally, the observation from the previous paragraph also emerges from Figure 1.28, depicting the instantaneous mechanical power over 500 seconds of individual wind turbines in the central row. Indeed, the first line wind turbines produce a comparable amount of mechanical power, but the mechanical production from the last lines appears much higher in the case of VAWTs. This also appears to be the case for average power generation on Figure 1.29 over the same period of about $(2 \times 52D/U_{mean,NREL})$

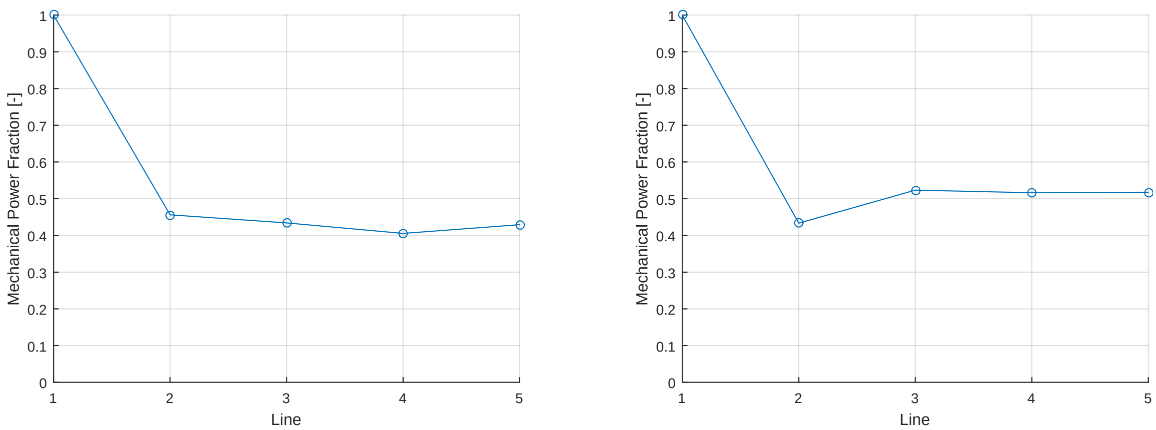

(a) HAWT (b) VAWT

Figure 1.27: Fraction of mean mechanical power generation on the central row with regards to the first line wind turbine

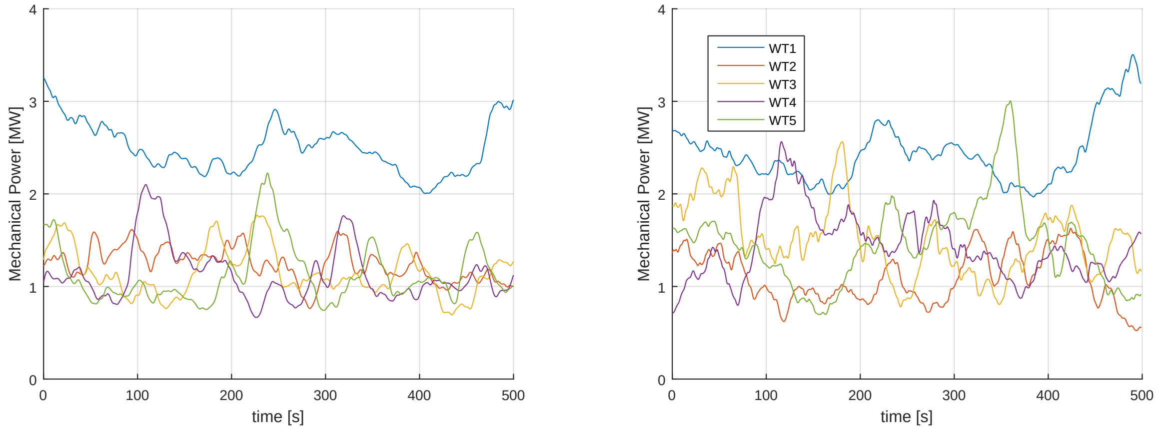

(a) HAWT (b) VAWT

Figure 1.28: Mechanical power generation in the central row over 500s. Wind turbines are labelled after by their line number.

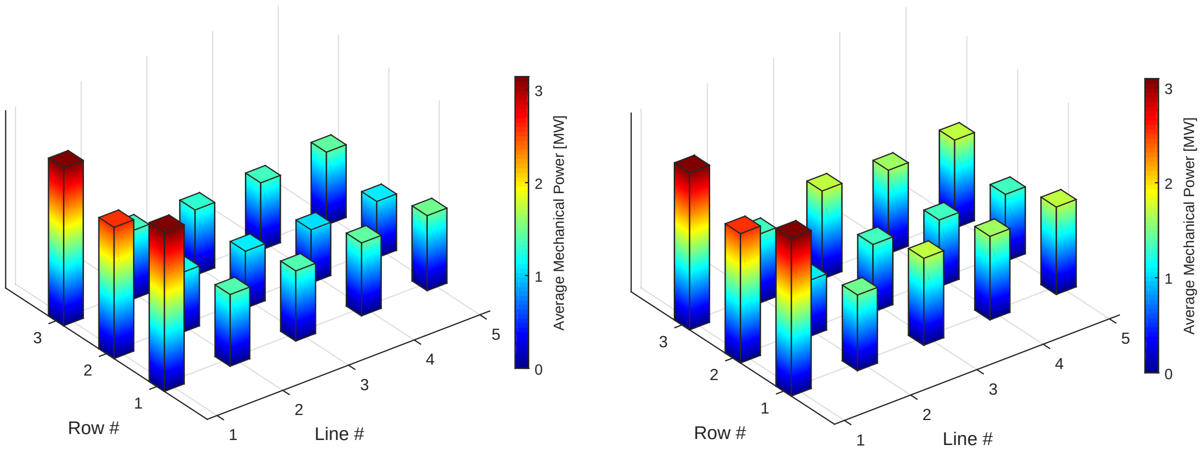

(a) HAWT (b) VAWT

Figure 1.29: Mean mechanical power generation

CHAPTER 2

ELECTRICAL PART

The electrical part of this wind turbine farm study consists in the modeling of the electro-mechanical conversion chain. The mechanical power harvested by the blades is converted in electricity suited for the electrical grid.

The electrical chapter of this report gathers a thorough research and simulated application of a choice of electro-mechanical conversion chain considered most suited for this project. The final result is a robust simulation in Matlab-Simulink that uses the Simscape-Power System environment.

In order to design the simulations and validate the results, each component of the conversion system has carefully chosen parameters rendering realistic results. A change in these parameters with real ones can be easily applied and offers a simulation of a real farm.

The major hypothesis considered is the fact that the wind farm is offshore, situated at the Belgian coast and contains up to 20 wind turbines. All the other hypotheses and parameters are detailed in the following sections.

This chapter starts with the motivation of conversion chain choices followed by its modeling. The control is divided in two parts: the control of the generator and the control of the electricity put into the grid. This model is implemented in an average model in order to accelerate the simulations. Afterwards, the synchronization of the 20 wind turbines is explained.

2.1 Wind Energy Conversion System and Grid Connection

The choice of the wind energy conversion system and grid connection is guided by the main characteristics of the wind turbine farm. The farm is situated offshore, each wind turbine yields a power of $5MW$ leading to a total power capacity of $100MW$ for the entire farm (as this is the rated power for the design of the farm). The wind turbines are considered to be large.

The main concern considering the choice of this type of conversion system is the overall cost that needs to be minimized. That accounts for the installed cost and the O&M. The goal is also to maximize the energy yield. Finaly, the power quality is important as well [25]. When considering horizontal axis wind turbines, the weight of the generator and converter is also an important aspect that increases the cost of the structure. However, the turbine considered in this report has a vertical axis allowing the conversion chain to be placed at sea level, decreasing the structure cost. Existing conversion systems are sorted according to two criteria: The use of a direct-drive or a gearbox and whether the generator is electrically excited or uses permanent magnets.

The motivations for the choice of conversion chain and the choice of grid connection are presented in the following order: the electro-mechanical conversion chain, the connection to the onshore grid, the impact of the wind farm on the power quality.

2.1.1 The Electro-Mechanical Conversion Chain (EMCC)

The EMCC can take different shapes and structuring design choices must be made before the simulations can be performed. Those choices will be made to optimise the total cost, the reliability and maintenance requirements (at equal cost), and the ability to provide higher output power quality. Assessment of the different options available rely on the available literature (referred).

Schematically, the EMCC is composed of the following elements (some optional):

- A physical connection between the wind turbine and the generator (direct or gearbox)
- A generator (type C or type D)
- A converter
- A submarine cable (HVDC or HVAC)
- A point of common coupling

Some combinations are not possible and complementarity must be ensured. The critical element is the generator.

Generator

Fixed speed or variable speed generator

A variable speed generator enables to adapt the rotational speed of the wind turbine in function of the wind speed, ensures minimal power fluctuation and should be preferred over a fixed speed generator [33]. It however requires power electronics downstream to adjust frequency and voltage to the grid requirements [60]. Nevertheless this combination “variable speed + power converter” is recommended.

Type C or Type D

Within the variable speed generators, several types exist:

- Type C consists of a Doubly-Fed Induction generator (DFIG). It can run at variable speed slightly above or below their synchronous speed and must commonly be used with a gearbox [36]. See the chain on Figure 2.1.
- Type D consists of different possibilities: the Squirrel Cage Induction Generator (SCIG); the Permanent Magnet Synchronous Generator (PMSG); the Wound-Rotor Synchronous Generator (WRSG). The type D does not always require a gear box (direct drive connection). See the chain on Figure 2.2

The drive train of wind turbine generators is subject to severe mechanical stress. It needs to support high transient loading during start-up, shut-down and emergency stop, and strong wind variations - all above normal onshore conditions. The direct drive, although operating at high torque (but low speed) is technically less complex than a gearbox.

As a result, a gearbox is more costly, has higher maintenance requirements and failure risks than a direct drive [25], [26], [28]. At the same time, generators driven through direct drive must contain more poles than the ones driven by gearbox, to produce a sufficiently high frequency

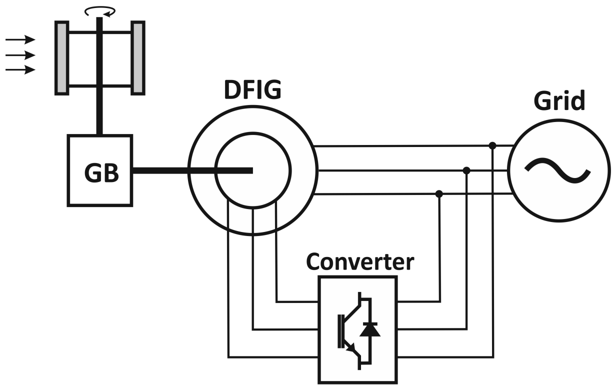

Figure 2.1: The type C Wind Energy Conversion System [36]

despite lower rotation speed. This in turn increases the cost of direct drive generators. The combined cost is usually comparable. The preference is then given to the higher reliability of the "type D + Direct drive" combination.

To be complete, a DFIG could also be used with a direct drive, providing the use of a slip scale converter [34], but this solution proves more costly than the other options and must be discarded.

Within the Type D family, the PMSG is the most efficient with its highest energy yield. Self-excited thanks to the permanent magnets, it does not use brushes which again decreases maintenance requirements. The generator is used with a fully rated converter - enabling reactive power compensation and active power control, resulting in a smooth grid connection. The chain is observed on Figure 2.2.

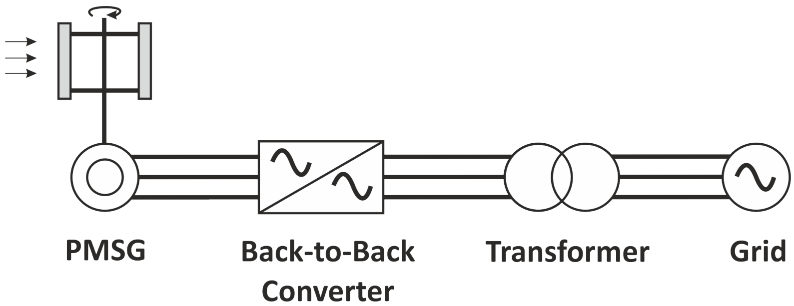

Figure 2.2: The type D Wind Energy Conversion System with the PMSG (The generator could also be of another type, such as SCIG or WRSG).

Converter

A description of the power converter is shown on Figure 2.3. The converter can be partitioned in a rectifier, that controls the electro-mechanical torque and an inverter, controlling active power and reactive power to the grid. As stated, this converter provides reactive power compensation and a smoother grid connection. The IGBT's play the role of switching using Pulse Width Modulation (PWM). The advantages are its low maintenance cost as well as the fact that the interharmonics generated are easily filtered [39]. Other types of converters are possible as well. For example, the role of the rectifier can be taken over by a diode with a boost. However, the back-to-back converter is the most appropriate type considering large-scale wind turbines.

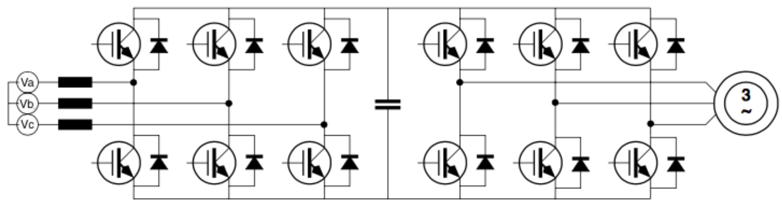

Figure 2.3: The back-to-back converter [39]

Point of Common Coupling and Cable

Offshore wind farms are connected to the electrical transmission system at a Point of Common Coupling where the grid is strong enough to absorb the power [29]. Concerning this wind farm, a Medium Voltage (MV) local grid is created, where the power generated by each wind turbine is collected and then fed into the onshore grid. The choice of that voltage is only economically driven [27]. It depends on the characteristics of the cables available on the market and the need of the wind farm.

The power is transmitted through a submarine cable until it reaches shore where it continues its way in an underground cable or an overhead line until the point of common coupling of a substation. The options of the connection are the following: a HVAC cable or a HVDC cable. Cost-wise, the HVAC cable is used when the distance between the farm and the onshore substation is shorter than approximately $50km$, [35]. This option generates high reactive power through a capacitance effect. In this case, the voltage level is increased by means of a transformation offshore before transmission to the shore. The cable can be oil-insulated or PEX-inuslated [30]. The HVDC cable has no capacitance effect but is more expensive as two converters need to be added. Therefore, this option is used for longer distances, when the costs break even.

Given the setup of the wind farm in this simulation (distance to onshore grid is smaller than $50km$), the HVAC option is selected.

The complete resulting scheme of the chain, shown on Figure 2.4, can be described as follows. The generator produces power at a variable frequency and magnitude. That power is converted in order for the voltage to match the grid frequency $50Hz$. Next, a step up transformer increases the voltage level to the local grid Medium Voltage. The power produced by all the wind turbines is collected and stepped up again to high voltage for transmission. A submarine HVAC cable conducts the power from the offshore substation to the onshore grid.

2.1.2 Impact of Wind Farm on Power Quality

As stated by the ENTSO-e, the European Network of Transmission System Operators for Electricity, wind turbines have to answer to new requirements in response to the high penetration of renewable energy in the grid. Those requirements are gathered in the codes. [30] states that the impact of an offshore wind farm on the power quality of the grid can have various forms. Different aspects of the voltage have to be studied, such as voltage variations, voltage fluctuations (e.g. flicker can occur during operations and switching) and steady-state voltage. Harmonics have to be studied as well, they induce power losses and higher currents leading to overheating consequences. In this case, the PWM allows the implementation of smaller filters, as the switching frequency is of the order of a few kHz, the generated harmonics have a higher frequency.

A load flow analysis is used to assess the impact of the wind farm on the grid in terms of voltage stability at the PCC. The frequency of the power system shows the balance between

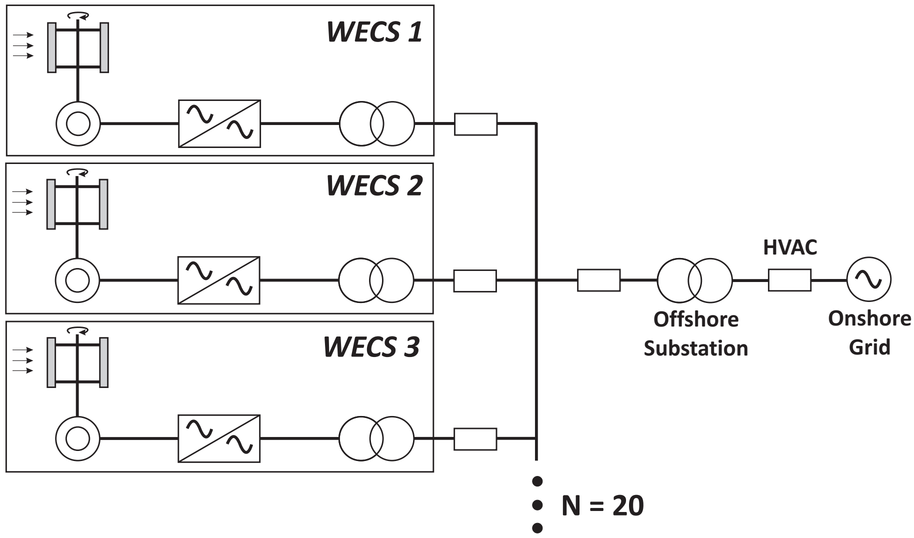

Figure 2.4: The Connection to the grid

production and consumption. Knowing that and as recalled in [31], the requirements are active power control to limit overproduction from the farm, control of the reactive power through the control of the voltage and participation in restoring the balance when a fault occurs in the power system.

The scope of this project is to study steady-state and faultless situations.

2.2 The Control of the Wind Turbine

Now that the choice of the chain has been covered, here is a description of the wind energy conversion system. The wind turbine outputs a mechanical power which is dependent on the speed of the wind. It can also be expressed as the product of the torque and the rotational speed of the shaft.

$$P_m = \frac{1}{2}\rho A C_p v_{wind}^3 = T_m \omega_m$$

How that power is extracted from the wind thanks to the blades has been explained in the previous chapters on the aerodynamical study.

The PMSG takes that torque as an input and transforms it into electrical power. The generator is connected to the back-to-back power converter consisting in a forced-commutated rectifier called the stator-side converter (SSC) and a forced-commutated inverter called the grid-side converter (GSC) connected through a common DC-link which is a capacitor [39]. The chain is shown on Figure 2.2.

The SSC controls the eletromechanical torque and thereby the rotational speed. The GSC controls the DC-link voltage and reactive power, while assuring that the output voltage has the same frequency as the grid voltage, that is $50Hz$.

This type of drive-train allows a full speed range (until rated speed) and provides a total decoupling of the control of the generator and the grid. The advantage is a smooth connection to the grid at the right frequency.

In this chapter the parameters of the wind energy conversion system and its control are presented in two parts: the generator side and the grid side. The references of the main pieces that helped building the theory and simulations of this section of the study are [38], [41], [32] and [40].

2.2.1 Generator side

The generator side consists of the permanent magnet synchronous generator and the stator side converter. In order to allow a realistic conclusion to be made about the simulations, parameters are chosen carefully from the literature available about wind turbine conversion chains.

The Governing Equations

The governing equations of the generator side are derived from the voltage equations of the PMSG written according to the "generator" sign convention.

$$V_{sa} = -R_s I_{sa} - \frac{d\psi_a}{dt}$$

$$V_{sb} = -R_s I_{sb} - \frac{d\psi_b}{dt}$$

$$V_{sc} = -R_s I_{sc} - \frac{d\psi_c}{dt}$$

Those equations are then written in Park's reference frame using the Direct-Quadrature-Zero transformation ($0dq$). Indeed, modeling the PMSG in a synchronously rotating reference frame allows to work with constant inductances (as they are no longer a function of the position of the rotor) because the permanent magnet flux linkage direction is aligned with the direct axis, leading to a constant magnetic path. For more information about the Park transformation, please refer to Appendix B.2.

$$\overline{V}_{0dq} = -R_s \overline{I}_{0dq} - \frac{d\overline{\psi}_{0dq}}{dt} - j\omega_e \overline{\psi}_{0dq}$$

The equation for the direct voltage and the quadrature voltage is found by isolating the real and the imaginary parts from each other.

$$V_{sd} = -R_s I_{sd} - \frac{d\psi_{sd}}{dt} - \omega_e \psi_{sq}$$

$$V_{sq} = -R_s I_{sq} - \frac{d\psi_{sq}}{dt} + \omega_e \psi_{sd}$$

No rotor equation is considered as the rotor is composed of permanent magnets and is not wound. Moreover, the rotor is round leading to one stator inductance $L_s = L_d = L_q$. The zero-current i_0 is constrained to be equal to zero as the generator is considered to be star-connected without neutral connection.

By decomposing the stator flux linkages ψ_{sd} and ψ_{sq} into their dependance on the stator currents I_{sd} and I_{sq} and the magnetic flux of the permanent magnet ψ_{PM}, the equations become

$$V_{sd} = -R_s I_{sd} - L_s\left(\frac{dI_{sd}}{dt} - \omega_e I_{sq}\right) \tag{2.1}$$

$$V_{sq} = -R_s I_{sq} - L_s\left(\frac{dI_{sq}}{dt} + \omega_e I_{sd}\right) + \omega_e \psi_{PM} \tag{2.2}$$

The resulting equivalent circuit of the PMSG is shown on Figure 2.5.

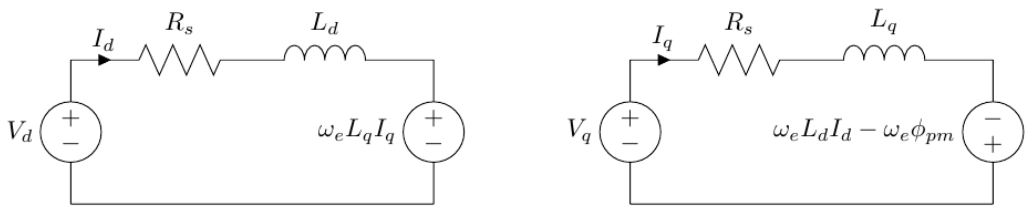

Figure 2.5: The equivalent circuit of the PMSG in the $0dq$ reference frame

In order to control a PMSG, several strategies exist such as Direct Torque Control (DTC) or Field Oriented Control (FOC). A short review of a comparison of the two methods reveals that the dynamic torque response observed with DTC is better than with FOC while the contrary is true in steady-state. In this thesis, FOC is applied.

To implement the control, the expressions of active and reactive power are necessary to find the equation of the electromagnetic torque. It will be used in the "Swing Equation", which models the link between the electrical and the mechanical torque.

The equations for the power are computed while neglecting stator resistance and considering a stationary state.

$$P_s = V_{sd} I_{sd} + V_{sq} I_{sq} = -\omega_e \psi_{PM} I_{sq}$$

$$Q_s = V_{sd} I_{sq} - V_{sq} I_{sd} = -\omega_e [L(I_{sd}^2 + I_{sq}^2) + \psi_{PM} I_{sd})]$$

As $T_{em} = \frac{P_s}{\omega_m}$ and $\omega_e = p\omega_m$ with p the number of pair poles of the synchronous generator, this gives

$$T_{em} = -p\psi_{PM} I_{sq} \tag{2.3}$$

The model described here uses Park's transform that conserves the power. Another form of Park's transform conserves the amplitudes, this is the one used by SimPowerSystems. The consequence is a multiplication factor of $\frac{3}{2}$ in the equation of the Torque T_{em}.

Finally, the dynamical behavior of the whole system can be described by the equation of motion. T_m is the mechanical torque, J is the total inertia of the system, that includes the inertia of the generator about the shaft, the rotor and the rotating part of the turbine itself. Equation 2.4 represents the acceleration occuring when there is a difference between the mechanical and the electromagnetic torque, defining the motion of the machine.

$$T_m - T_{em} = J \frac{d\omega_m}{dt} \tag{2.4}$$

The goal of the wind turbine control system is to retrieve the largest amount of power from the wind, it is also called the Maximum Power Point Tracking (MPPT). The method used here is the Tip Speed Ratio (TSR) Control that consists in keeping the TSR at its optimal value in order to extract the maximum power out of the wind [43]. The curves on Figure 2.6 show the power that can be extracted from the wind as a function of the rotational speed of the turbine for several values of wind velocity. This is the preferred method concerning large-scale wind turbines. The only requirement is the need to measure the wind speed at each time step.

Of course, other methods exist. One of them is the Optimal Torque Control where the torque is optimized according to the optimal TSR. Here the wind speed is not measured directly, therefore the efficiency of this methods is lower than the one of the TSR control. The third method considered is the Power Signal Feedback Control. It uses a record of the optimal speeds taken from the maximum power curves of the wind turbine. The efficiency is comparable to the Optimal Torque Control. The last method is the Perturb and Observe Control which uses optimization to find the maximum power point. This method is less dynamic and is therefore not used in wind turbines with large inertia [43].

Back to the control of the wind turbine, the FOC technique uses the rotational speed of the shaft to control the power extracted, by tracking the optimal speed at which the rotor should rotate to maximize that power. This is found through the aerodynamical equations, based on the mechanical parameters of the wind turbine and described in the mechanical sections of this thesis. By using Equation 2.5, the control ensures the reaching of the optimal speed. λ_{opt} is the TSR, v_{wind} is the speed of the wind and R is the Radius of the wind turbine.

$$\omega_{ref} = \frac{\lambda_{opt} v_{wind}}{R} \tag{2.5}$$

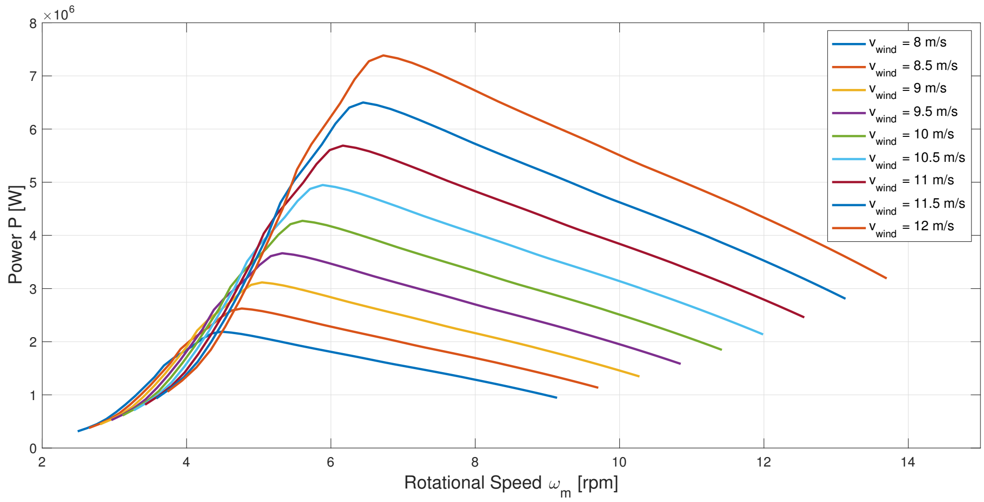

Figure 2.6: For different wind speeds, the power curve is given as a function of the rotational speed of the wind turbine. The maximum power points can be observed.

Equations 2.1, 2.2, 2.3 and 2.4 model the behavior of the generator side of the system and are used to implement a control of the speed and torque of the generator. On one side, Equation 2.3 shows that the torque is controlled by only the quadrature current I_{sq} output by the PMSG. Therefore, the reference of the direct current I_{sd} is controlled to be 0 to allow a linear control of the active power P_s and minimize the Joule losses. On the other side, Equation 2.4 leads to the conclusion that the rotational speed of the rotor can be controlled by applying a variation to the torque. For example, if the turbine is rotating faster than the optimal speed, computed on the basis of the wind speed, the absolute value of the electromagnetic torque should be decreased in order to reduce the rotational speed. Therefore current I_{sq} has to drop.

The model being described, some parameters are needed before completing the control equations.

The Permanent Magnet Synchronous Generator

The parameters governing the operation of the PMSG are found in [37] and are the properties used for the $5MW$ baseline wind turbine of the NREL (The United States National Renewable Energy Laboratory). The inertia of the rotor and turbine about the shaft comes from [42]. All the parameters needed can be computed from the values in Table 2.1.

Table 2.1: Data and Parameters of the Generator Side

Wind Turbine Parameters	
Rating	5MW
Control	Variable Speed
Rotor and turbine inertia about the shaft	$4.98 * 10^8 kg.m^2$
Generator Parameters	
Nominal Power $P_{gen,nom}$	$5.3MW$
Nominal Torque $T_{gen,nom}$	$4.18MN.m$
Generator inertia about the shaft	$5,025,500kg.m^2$
Generator Side Characteristics	
No. of pole pairs, p	100
The rms induced no load voltage at rated speed, E_0	$2.31kV$
The stator resistance, R_s	0.08Ω
The magnetizing inductance, L_{sm}	$3.352mH$
The leakage inductance, L_{sl}	$5.028mH$

Computed from the nominal power and the nominal torque, the nominal speed of the generator is $12.1rpm$. The inertia of the generator, the rotor and the turbine gives the inertial time constant

$$H = \frac{\frac{1}{2}J\omega_{nom}^2}{P_{nom}} = 76.2928s$$

Physically, in twice the value of H, when the nominal torque is applied to the generator, it reaches the nominal speed. The inertia of a VAWT is about 12 times the inertia of a HAWT for a rated power of $5MW$.

The flux linkage is $\psi_{PM} = 25.765Wb$, found through this equation:

$$E_0 = \frac{\omega_e \psi_{PM}}{\sqrt{3}} = \frac{p\omega_m \psi_{PM}}{\sqrt{3}}$$

ω_e is the electric rotational speed and ω_m is the mechanical rotational speed. As the generator considered is round, the direct and quadrature inductances are equal to each other. Their value is computed as follows

$$L_q = L_d = L_s = L_{sm} + L_{sl} = 8.379mH$$

Comments on the Parameters of the PMSG:

The parameters can be compared to the ones of a PMSG used for small wind turbines. The one chosen has a rated power of $50kW$ [32].

For a representative comparison, the electrical parameters are written in per unit value. For more information about this unit system, please refer to Appendix B.1. For the large wind turbine generator, the base voltage is the no load voltage at rated speed $V_B = 2310V$, the base power is $S_B = 5.3MVA$. For the small one, the base voltage is $V_b = 32V$ and the base power is $S_b = 50kVA$. The stator resistance of the large wind trubine generator is 200 times larger than the small one. The armature inductance, is about 50 000 times larger.

There are about 5 times more pole pairs in the large generator. Finally, considering the inertia of the generator, it is a 1000 times larger for the large generator and it results in an inertial time constant of about 1 second.

This allows to conclude that the extrapolation from a $50kW$ PMSG towards $5MW$ is not linear at all and the parameters cannot just be extrapolated on that basis.

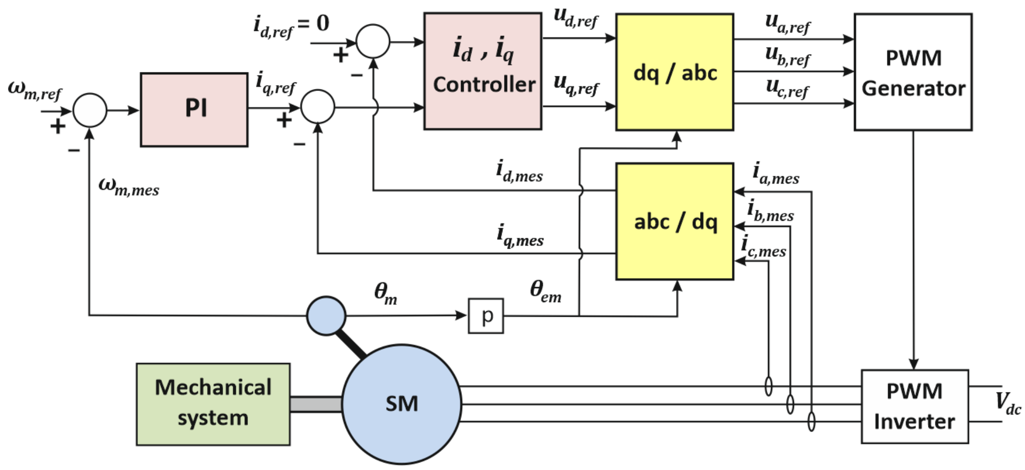

Figure 2.7: The global control of the dq current components of the PMSG [41]

The Implementation of the Control

A control has to be implemented for I_{sd} and I_{sq}, based on the governing equations and parameters detailed in the previous subsections. From the errors in $0dq$ current components, a $0dq$ voltage reference is computed and transformed into a pulse through a Pulse-Width Modulation (PWM) controlling the switches of the rectifier to the DC-link, as shown in Figure 2.7.

The control loops are designed according to the governing equations 2.1, 2.2, 2.3 and 2.4, rewritten in the Laplace domain. They are presented in Figure 2.8. As stated previously, the torque can be controlled by varying only the quadrature component of the current I_{sq}. The control of it is based on the error in rotational speed, which is the difference between the optimal rotational speed and the actual one. The optimal rotational speed is computed from the wind speed in Equation 2.5.

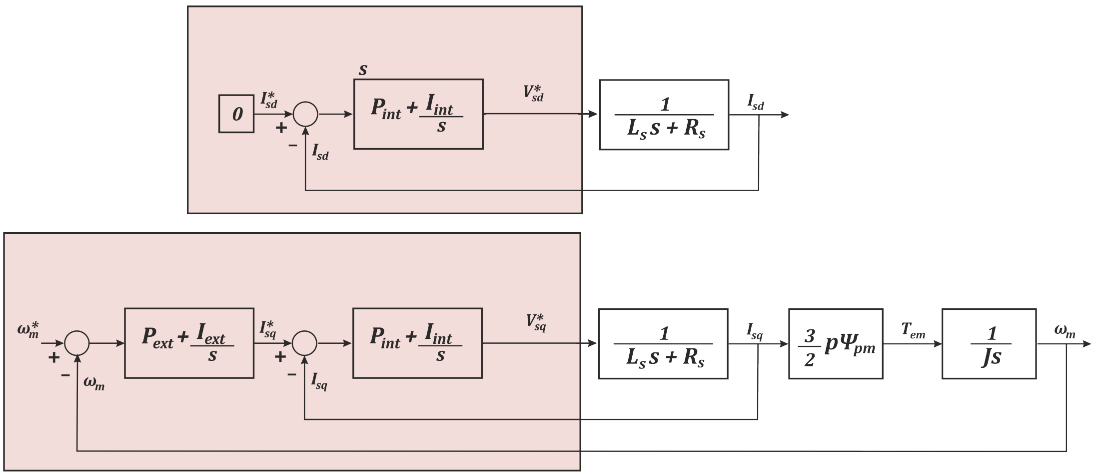

Figure 2.8: The detailed control of the dq current components of the PMSG

When designing the inner loop, only that loop is considered. However, for the design of the outer loop, the inner one is considered to be a unity block, as shown in Figure 2.9. This hypothesis is true when the internal loop is faster (about 10 times) than the external loop.

The controller used is a proportional integral (PI) controller in order to cancel out the static error.

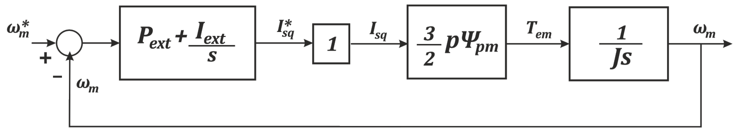

Figure 2.9: Design method of the outer loop of the control of I_{sq} of the PMSG

Equation 2.1 for the direct component of the voltage, V_{sd}, is written in the Laplace domain:

$$I_{sd} = \frac{p\omega_m L_s I_{sq} + V_{sd}^*}{R_s + L_s s} = \frac{V_{sd}}{R_s + L_s s}$$

giving the following reference voltage:

$$V_{sd}^* = V_{sd} - p\omega_m L_s I_{sq}$$

The term $-p\omega_m L_s I_{sq}$ is the feedforward term. This enables the extraction of the open loop transfer function $G(s)$:

$$G(s) = \frac{1}{L_s s + R_s}$$

For the direct current I_{sd}, the variable P_{int} and I_{int} are found considering the controller transfer function $C(s)$:

$$C(s) = P_{int} + \frac{I_{int}}{s}$$

Be careful not to mix up the underscore s that stands for "stator" and the normal s which is the complex variable $s = j\omega$. Next, the closed loop transfer function can be computed:

$$T(s) = \frac{C(s)G(s)}{1 + C(s)G(s)} = \frac{\frac{P_{int}}{L_s}s + \frac{I_{int}}{L_s}}{s^2 + \frac{R_s + P_{int}}{L_s}s + \frac{I_{int}}{L_s}}$$

This is a second order transfer function, therefore, the denominator can be written in the generic form:

$$s^2 + 2\zeta\omega_n s + \omega_n^2$$

This allows to find the parameters of the PI chain as a function of the parameters of the generator:

$$P_{int} = 2\zeta\omega_{int} L_s - R_s$$

$$I_{int} = \omega_{int}^2 L_s$$

The inner loop parameters are the same for the quadrature component of the current I_{sq}, with another feedforward term: $p\omega_m(L_s I_{sd} + \psi_{PM})$.

Now, for the outer loop, the method is similar with as open loop transfer function $G(s)$:

$$G(s) = \frac{p\psi_{PM}}{Js} = \frac{T_{em}}{Js}$$

and results in the following parameters:

$$P_{ext} = 2\zeta\omega_{ext}\frac{J}{p\psi_{PM}}$$

$$I_{ext} = \omega_{ext}^2 \frac{J}{p\psi_{PM}}$$

In Figure 2.9, the block scheme of the outer loop of the control of the quadrature component of the current is shown. In the block connecting I_{sq} and T_{em}, there is a multiplication factor of 3/2. This is due to the conservation of amplitude in the Park transform used by Simulink, as explained before.

ω_{int}, ω_{ext} and ζ are the last parameters to finalize the generator side design.

In order to limit DC-link voltage variations and, as mentioned before, to enable the design method of the outer loop, the natural frequency of the inner loop is chosen to be 10 times faster than the outer loop. The frequency for the controllers is: $f_{int} = 100Hz$ and $f_{ext} = 10Hz$ leading to pulsations $\omega_{int} = 2\pi f_{int}$ and $\omega_{ext} = 2\pi f_{ext}$. Next, the damping ratio ζ can be adjusted between the boundaries 0.7 and 1 to limit the overshoot. After some tests of the simulations with variation of the parameters, the decision is to fix it to 1.

In the SSC, the switching frequency of the PWM generator is fixed and therefore, the modulation is not synchronous. The switching frequency is chosen to enable cancelling of higher order harmonics. For the modulation to be synchronous, the ratio between the frequency and carrier frequency has to be an integer. The harmonics of order 3 are cancelled if the modulation ratio is a multiple of 3, that is the ratio between the switching frequency and the stator frequency. However the stator frequency is not constant, therefore the cancelling of the order 3 harmonics cannot be known in advance. The choice goes to a switching frequency of $3kHz$. However, this will not be relevant after the switching model is changed into an average model. This is discussed in Section 2.3.

The generator side is now covered, the next logical step is to present the grid side.

2.2.2 Grid side

The grid side comprehends the grid side converter and the connection to the medium voltage local grid, right before the step up transformer. The GSC is an inverter whose switches are controlled by the pulse coming out of a PWM generator. The goal of the control is to keep the DC-link Voltage constant to a value imposed by the parameters, in order to keep the active power production flowing from the generator to the grid. The other purpose of the GSC is to control the grid voltage and thereby the reactive power.

The Governing Equations

The GSC is governed by its voltage equations that can be written in Park's reference frame. They are built from the equivalent circuit found on Figure 2.10. The subscript c points to the converter and the subscript g to the grid.

$$V_{cd} = RI_d + L\frac{dI_d}{dt} - \omega_e LI_q + V_{gd} \tag{2.6}$$

$$V_{cq} = RI_q + L\frac{dI_d}{dt} + \omega_e LI_d \tag{2.7}$$

The active and reactive power to the grid are computed as follows:

$$P_g = V_{gd}I_d$$

$$Q_g = -V_{gd}I_q \tag{2.8}$$

The active power exchange around the DC-link capacitor is computed with P_s, the output power from the stator of the generator and P the power exchanged by the capacitor, derived from the energy stored in the capacitor, $\frac{CV^2}{2}$.

$$P = P_s - V_{gd} I_d$$

To control the DC-link voltage, the power from the stator P_s is considered to be constant compared to the pace of variation of the power flowing towards the grid side converter, $V_{gd}I_d$. Therefore, the only control variable for this purpose is I_d.

$$CV_{dc}\frac{dV_{dc}}{dt} = P_s - V_{gd} I_d \tag{2.9}$$

Equations 2.6, 2.7, 2.8 and 2.9 are governing the control.

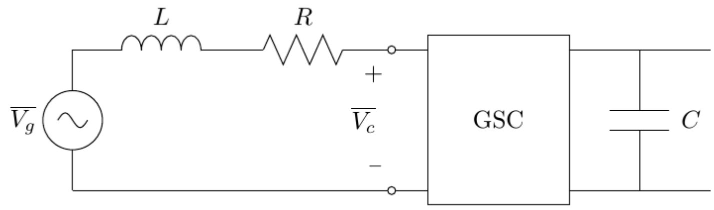

Figure 2.10: The equivalent circuit of the grid side converter

To obtain the direct and quadrature components, one needs the phase angle of the grid voltage in real time. This is obtained when the frequency of the output of the inverter is equal to the one of the grid and that for each phase. This phase angle is found through a Phase Locked Loop (PLL) and is used to create the pulse from the PWM.

Now that the governing equations are known, the parameters can be chosen.

The Parameters of the Elements of the Grid Side

The parameters chosen for the thesis are taken from the NREL $5MW$ baseline wind turbine [37] and are appropriate for the situation designed in this master thesis. The parameters are gathered in Table 2.2.

Table 2.2: Characteristics of the Grid Side

Grid Side Characteristics	
Grid Voltage V_g	$4kV$
Line Filter Inductance L_f	$4mH$
DC Bus Voltage V_{DC}	$6.4kV$
DC Bus Capacitance C	$4000\mu F$

The Implementation of the Control

Knowing the parameters and the equations, the control of the grid side can be implemented by starting with the PLL. It has been designed according to [44] and [45] and the resulting loop is shown in Figure 2.11. The PLL is divided in three parts: the phase detector, the loop filter and the Voltage Controlled Oscillator (VCO). The phase detector tracks the phase of the grid voltage. The loop filter is a PI controller. The VCO ensures to match the phase. To compute the parameters of the PI controller, the system is linearized and the transfer function is written as:

$$\frac{\phi_{out}}{\phi_{in}} = \frac{K_{PD}K_{VCO}C(s)}{s + K_{PD}K_{VCO}C(s)}$$

ϕ_{out} and ϕ_{in} are the output and input phases respectively. K_{PD} is the gain of the phase detector, K_{VCO} is the gain of the VCO and $C(s)$ is the transfer function of the loop filter, i.e. the PI controller.

$$C(s) = P_{PLL} + \frac{I_{PLL}}{s}$$

The resulting transfer function is:

$$T(s) = \frac{K_{PD}K_{VCO}P_{PLL}s + K_{PD}K_{VCO}I_{PLL}}{s^2 + K_{PD}K_{VCO}P_{PLL}s + K_{PD}K_{VCO}I_{PLL}}$$

By considering that K_{VCO} is equal to 1 to match Figure 2.11. The parameters P_{PLL} and I_{PLL} are found by fixing the damping ratio ζ and the pulstaion ω_n to 1 and $2\pi 100$ respectively, as the denominator corresponds to the second order: $s^2 + 2\zeta\omega_n s + \omega_n^2$. The gain K_{PD} has been tuned for optimal response and equal 4000. This leads to the following PI controller:

$$P_{PLL} = \frac{2\omega_n\zeta}{K_{PD}}$$

$$I_{PLL} = \frac{\omega_n^2}{K_{PD}}$$

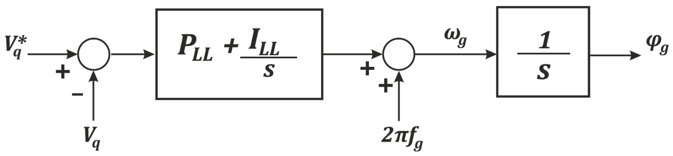

Figure 2.11: The phase locked loop

The control loops for the currents of the grid side are shown in Figure 2.12. As for the generator side, while designing the parameters of the external loop, the inner loop is considered as a unity block.

The control of voltage V_{DC} is the external loop computing the direct component of the current I_d. It is designed from equation 2.9, rewritten as:

$$V_{DC}^2 = \frac{P_s - V_{gd}I_d}{Cs}$$

The open loop transfer functions are:

$$C(s) = P_{ext} + \frac{I_{ext}}{s}$$

$$G(s) = -\frac{V_{gd}}{Cs}$$

and the closed loop transfer function is of second order:

$$T(s) = \frac{-\frac{V_{gd}}{C}(sP_{ext} + I_{ext})}{s^2 - \frac{V_{gd}P_{ext}}{C}s - \frac{V_{gd}I_{ext}}{C}}$$

The coefficients of the denominator are equal to the coefficients of $s^2 + 2\zeta\omega_n s + \omega_n^2$, leading to the following parameters of the PI controller.

$$P_{ext} = -\frac{2\omega_n\zeta C}{V_{gd}}$$

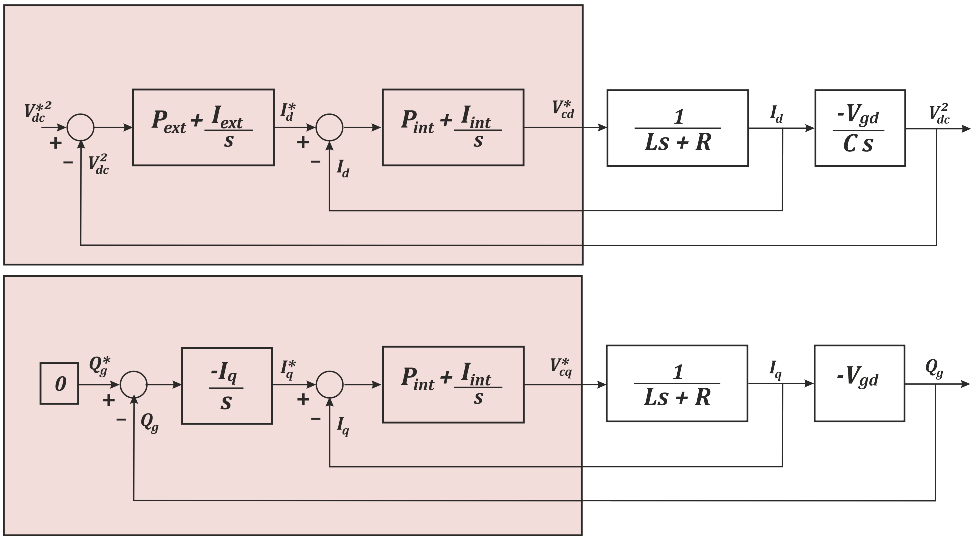

Figure 2.12: The control loops of the grid side converter

$$I_{ext} = -\frac{\omega_n^2 C}{V_{gd}}$$

For the external loop, the natural frequency is set to $10Hz$, therefore $\omega_{ext} = 2\pi 10$. Again, the damping ratio is fixed to 1.

The external loop controlling the reactive power is parametrized from Equation 2.8. Here, the control is an integrator with $C(s) = \frac{I_Q}{s}$ and the open loop transfer function is $G(s) = -V_{gd}$. I_Q is the integral parameter and should not be mistaken for the quadrature component of the current I_q. V_{gd} has a value of $4kV * sqrt(2/3)$, as presented in the parameters of the grid. The resulting closed loop transfer function is:

$$T(s) = \frac{1}{-\frac{s}{I_Q V_{gd}} + 1}$$

The reactive power reference is set to be nul in this step of the study. That means that the generator will not inject or absorb reactive power to or from the grid. I_Q is found by setting the natural frequency of this first order loop function at $10Hz$.

$$I_Q = -\frac{f_n}{V_{gd}}$$

Finally, the internal loop for the direct and quadrature components of the current is computed. The feedforward term of the control of I_d is $-\omega_g L I_q + V_{gd}$. The one for the control of I_q is $\omega_g L I_d$. They are obtained from the governing equations of the direct and quadrature voltages written in the Laplace domain. The parameters are the same in both PI controllers. The closed loop transfer function is:

$$T(s) = \frac{\frac{P_{int}}{L}s + \frac{I_{int}}{L}}{s^2 + \frac{R+P_{int}}{L}s + \frac{I_{int}}{L}}$$

The natural frequency chosen is $100Hz$ as this is the inner loop. The damping ratio is 1.

$$P_{int} = 2\zeta\omega_{int}L - R$$

$$I_{int} = \omega_{int}^2 L$$

2.2.3 Simulation Results

All the parameters computed are inserted in the Simulink simulations. The simulink blocks are gathered in Appendix B.4. In order to test the performance of the design, tests were executed using a wind turbine model with a function for the power coefficient found in the litterature [32]. The C_p curve is shown on Figure 2.13.

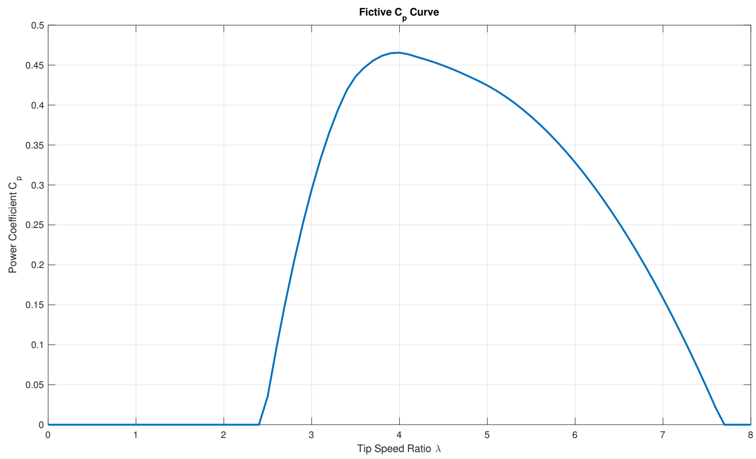

Figure 2.13: The theoretical C_p curve used to test the electrical part of the simulations

As the inertia of a VAWT is higher than the one of a HAWT for the same rated power (by more than a factor 10 in this case), the tests were performed using the parameters of the latter one in order to reduce the computation time. The NREL HAWT parameters were chosen.

The simulation tested the response to a variation in wind speed shown in Figure 2.14, as this is the important aspect in the coupling. The wind is decreased and increased in the shape of a ramp in order to test if the generator side control is able to follow the optimal speed and if the grid side control can keep V_{DC} at its value of $6400V$ and the reactive power fixed at 0. The wind speed variations are not realistic but allow a good view of the response expected.

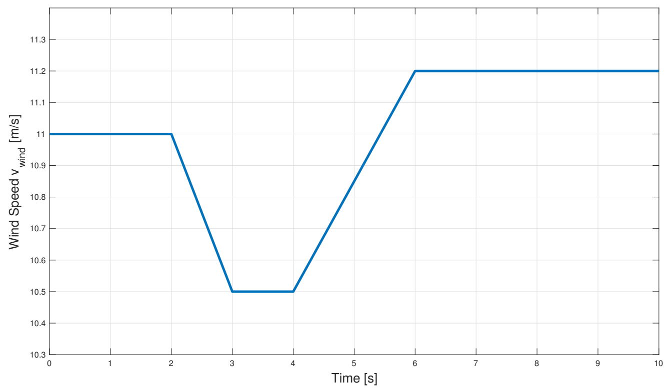

Figure 2.14: The wind speed

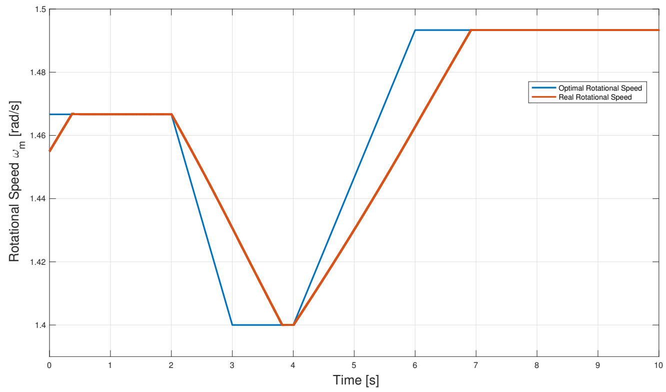

Figure 2.15: The rotational speed of the generator compared to the optimal rotational speed

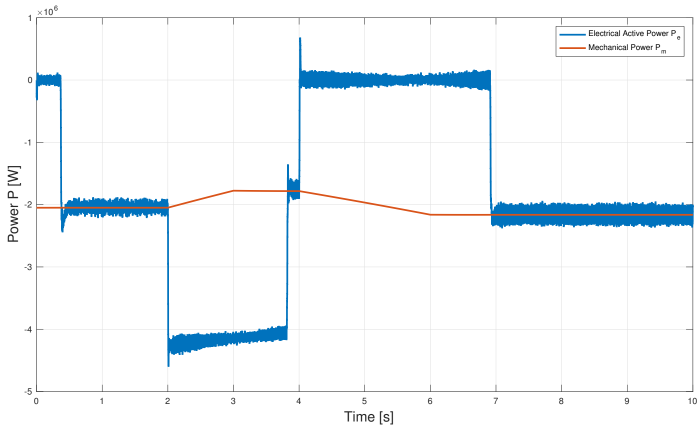

Figure 2.16: The electrical and mechanical power

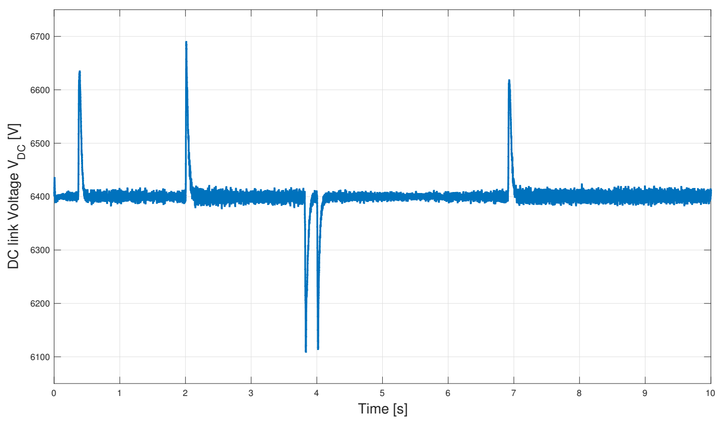

Figure 2.17: The DC link voltage

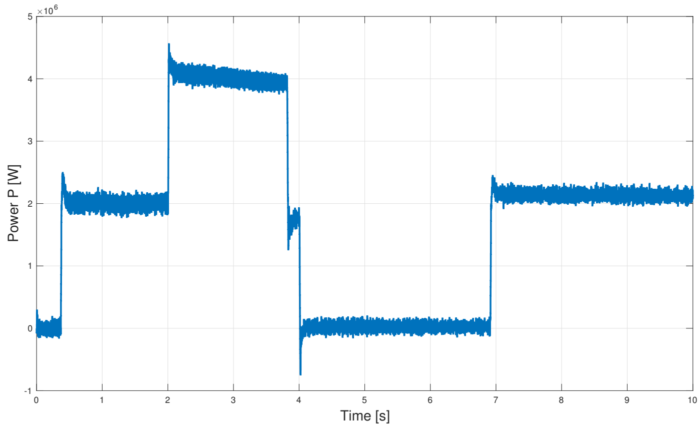

Figure 2.18: The active power produced

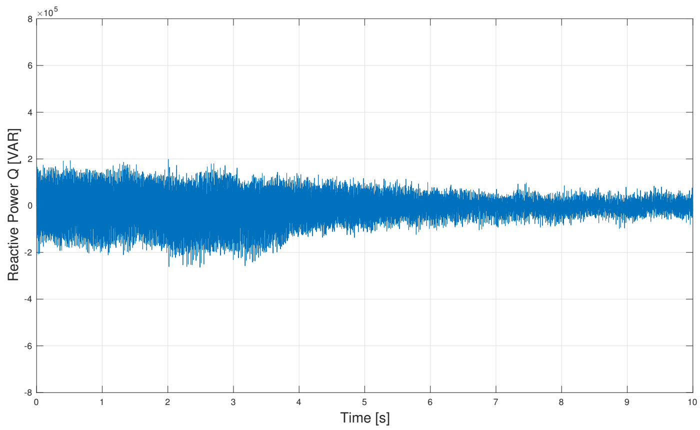

Figure 2.19: The reactive power injected or consumed by the generator

Rotational Speed:

The speeds shown in Figure 2.15 are the optimal speed computed from the wind speed following the MPPT strategy of optimal tip speed ratio and the real speed of the generator. The rotational speed is varied by the control in order to reach the maximum power coefficient which will yield the highest active power production.

In the simulation, first, the optimal rotational speed is reached, starting from an initial value of $1.455 rad/s$. Next, the wind speed decreases as does the optimal rotational speed. The rotational speed follows until reaching the new optimal one and entering steady-state for a short time. Then, the wind accelerates inducing an acceleration of the rotational speed that wants to follow the new optimal speed. Finally a new steady-state is reached and the rotational speed does not deviate from it. The wind speed observed accelerates faster than the generator's ability to follow because of the high inertia of the wind turbine, however the delay is small.

The conclusion is that the generator side control leads to a good response.

Electrical Power:

The electrical active power produced is compared to the mechanical power transferred in Figure 2.16. The figure actually indicates the dynamics of the system as the powers are directly linked to the torque through the rotational speed, and the torques are linked thanks to the Swing Equation 2.4. As the generator convention is followed, a negative power means production while a positive power means consumption. The simulation results show that the generator produces more power when it decelerates, while it produces nothing when accelerating. Actually, this comes from a limit put on the direct component of the generator current which is set to 0. When the optimal speed is reached and the system is in steady-state, the active power is constant. A lot of noise is observed in the signal, this is discussed in Section 2.3.3. Concerning the mechanical power, it is also constant at steady-state and varies with the rotational speed. The values reached by the electrical power are the maximum values of the torque. This is due to the rapid control.

DC Link Voltage:

The DC link voltage has to stay constant or vary in an acceptable range (10% of its value) in order for the active power to be transferred continuously without damaging the capacitor. Figure 2.17 shows that this condition is satisfied. The small overshoots occur when the speed variations take place because it influences the active power transmitted.

Active Power:

The active power produced is shown on Figure 2.18. The amount of power produced depends on the rotational speed of the wind turbine. The steady-state production of power increases with the wind speed as can be observed when comparing the power production between $0.3s$ and $2s$ with the one produced between $7s$ and $10s$. As expected, the active power is equal to the electrical power produced by the generator, however positive.

Reactive Power:

The reactive power is regulated to 0 at all times as shown in Figure 2.19. However, the reactive power is sensitive to the noise input as well. Again, this is discussed in Section 2.3.3.

2.2.4 Conclusion

The control of the wind turbine conversion chain that includes a PMSG and a back-to-back converter without gearbox is completely decoupled. The control of the generator side acts on the speed of the wind turbine and guides it to the optimal speed extracting the maximum power out of the wind. The control of the grid side acts on the voltage of the DC-link, stabilizing it to a constant value, and on the reactive power, fixing it to zero.

The results computed in this section are the essential parameters of the control of the wind turbine. They are dependent on the parameters of the physical components of the conversion chain which allow to use the simulations in different cases. The tuning parameters of the controllers are gathered in Table 2.3.

Table 2.3: Proportional and integral gains of the control loops of the wind turbine

Generator Side			
P_{int}	$2\zeta\omega_{int}L_s - R_s$	P_{ext}	$2\zeta\omega_{ext}\frac{J}{p\psi_{PM}}$
I_{int}	$\omega_{int}^2 L_s$	I_{ext}	$\omega_{ext}^2\frac{J}{p\psi_{PM}}$
Grid Side			
P_{PLL}	$\frac{2\omega_n\zeta}{K_{PD}}$	P_{Vdc}	$-\frac{2\omega_n\zeta C}{V_{gd}}$
I_{PLL}	$\frac{\omega_n^2}{K_{PD}}$	I_{Vdc}	$-\frac{\omega_n^2 C}{V_{gd}}$
P_{int}	$2\zeta\omega_{int}L - R$	I_Q	$-\frac{f_n}{V_{gd}}$
I_{int}	$\omega_{int}^2 L$		

The outcome of the simulations shows that the parameters computed lead to a good response in terms of speed, concerning the generator side control. The DC link voltage as well as the reactive power are kept at their wished value as well. This allows to conclude that the controls are operational.

2.3 The Average Model

The model of the wind energy conversion system is now designed and operational. That model is called the switching model because of the switching role of the back-to-back converter. However, the simulation of one wind turbine takes up a considerable computation time. In the next steps of the present study, the goal is to increase the number of wind turbines up to a batch of 20 machines. The amount of computation time to run that simulation is too high. To reduce it, an average model can be used.

An average model allows to keep the dynamics of the simulations while not propagating the high frequency phenomena. The fundamental frequency of the voltage and the current is the only component to be transmitted [61]. The results are very close to the switching model while offering a faster simulation time and preserve the current controllers.

The goal is to use the operation principle of the converter and its control and replace the interface between the generator and the AC grid. This means three simply controlled voltage sources are connected to the generator and three others to the grid. The DC link is replaced by a simple model.

In [46], [47], [48], [49], [50] and [65], the switching model and the Average Voltage Estimation Model (AVEM) are explained for different types of conversion chains. In this study, the PWM generator is suppressed and the *abc* control voltage $V_{abc-ctrl}$ is directly connected to the controlled voltage sources. This for the generator side as well as for the grid side, see the model on Figure 2.20.

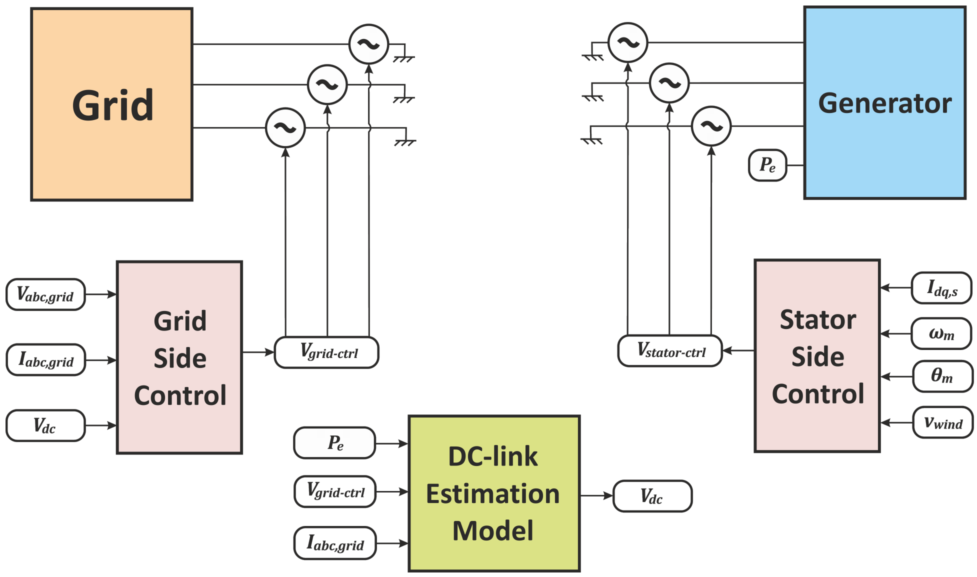

Figure 2.20: The average model

The advantages of an average model are plural. As stated before, the simulation time is considerably reduced, while the implementation is straightforward. The control, the mechanical system and the generator are untouched which ensures a similar result to the switching model. The switching component and their harmonics are suppressed, but this is not a problem in this type of study.

2.3.1 From Switching to Average Model

To model the converter as a set of fundamental frequency voltage sources, the following conditions need to be valid:

- The machine parameters are known
- The controllers operate in the linear region
- The terminal voltage is approximately the nominal value
- Vector modulation is used

The first two conditions are determined by the manufacturer, it is assumed to be true here. The third one is true if there are no grid faults, which are not considered in this study. The fourth is respected when PWM generators are used [60].

The estimation of the DC link voltage that enables its control is the model of the connection between the generator and the AC load which is the grid. For the generator side, the DC current I_{DCgen} coming from the stator side converter has to be computed. As the SSC has been replaced by the controlled voltage sources, it has to be implemented in a simple equation: the current is equal to the electrical power transmitted divided by the DC link voltage.

Regarding the DC current flowing towards the load I_{DCgrid}, it can be computed in a similar manner. The power from the grid is computed thanks to the voltage sources and the three-phase current I_{abc} and is then divided by the DC link voltage.

The equations are:

$$P_e = I_{DCgen} V_{DC}$$

$$P_{grid} = V_a I_a + V_b I_b + V_c I_c$$

$$P_C = P_e - P_{grid}$$

$$V_{DC} = \frac{I_{DCgen} - I_{DCgrid}}{Cs}$$

$$V_{DC} = \frac{\frac{P_e}{V_{DC}} - \frac{V_a I_a + V_b I_b + V_c I_c}{V_{DC}}}{Cs} \tag{2.10}$$

The model of Equation 2.10 is shown in Figure 2.21.

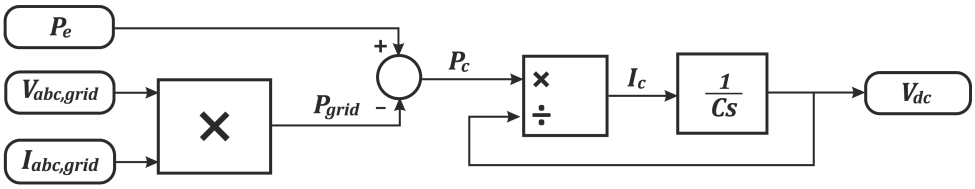

Figure 2.21: The model of the DC link

2.3.2 Simulation Results

The implementation in Simulink is in Appendix B.4. The most expected outcome is the gain in time. Both simulations of 10 seconds were executed on a computer using an Intel Core i5, saving the same amount of data and run in Simulink acceleration mode. The average model took 20 seconds to perform, while the detailed model took 4 minutes and 9 seconds. The detailed simulations take 12.45 times more computation time.

The resulting speed, voltage and power production are compared to the ones obtained by the switching model that were presented in Section 2.2.3. The same theoretical power coefficient and the same parameters are used, the same wind profile is applied.

Rotational Speed:

In Figure 2.22, the speed profile obtained with the switching model and with the average model are superposed. The average model keeps the dynamics of the generator side control intact. That is expected as the control is actually untouched.

DC Link Voltage:

The DC link voltage is shown in Figure 2.23. A high noise reduction can be observed when comparing the switching model to the average model, which suggests that the noise is produced by the switching of the universal bridge. Peaks are still observed each time the active power reaches a new state.

Active Power:

Again, the noise is reduced to 0 in case of the average model as can be observed in Figure 2.24. All the states of power are clear and follow the states of speed: deceleration, steady-state, acceleration. A slight overshoot can be observed each time the power reaches one of these states. It can be decreased or increased by varying the damping ratio ζ presented in the control in Section 2.2. Recall also that the wind input is not realistic. In Sections 3.2 and 3.3, results show that with a real wind input, this overshoot is not experienced by the system anymore.

Reactive Power:

Finally, for the reactive power (observed in Figure 2.25), the noise is reduced again. Some ripples are seen each time the active power overshoots. These are not significantly high but they will have an impact when all added in the farm.

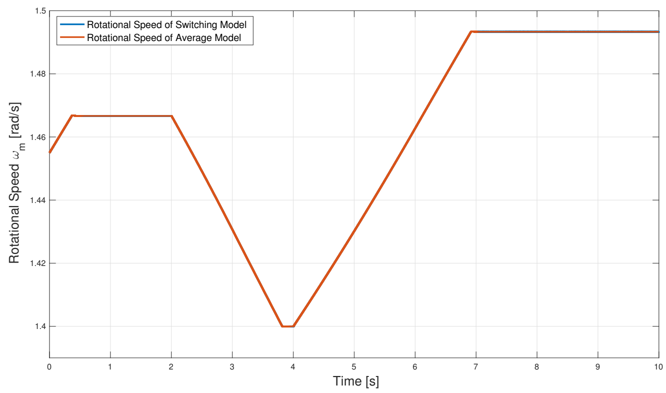

Figure 2.22: The rotational speed by the switching model and the average model

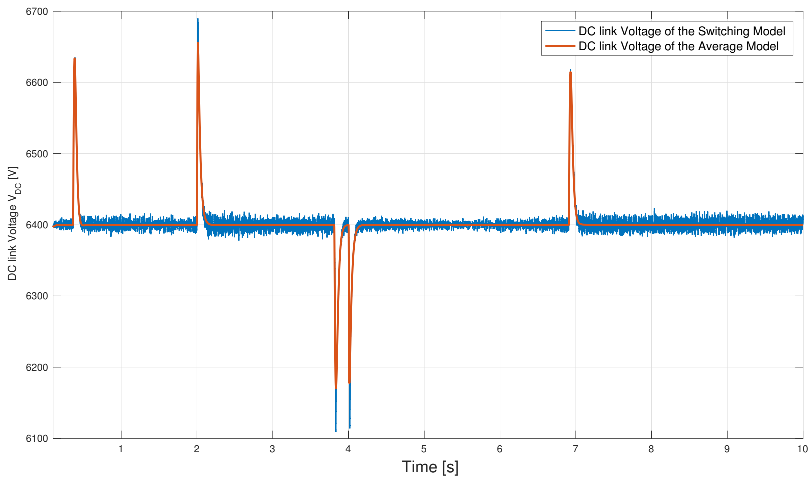

Figure 2.23: The DC link voltage by the switching model and the average model

The results allow to conclude that the dynamics of the wind turbine have been respected and therefore the precision of this model is satisfying.

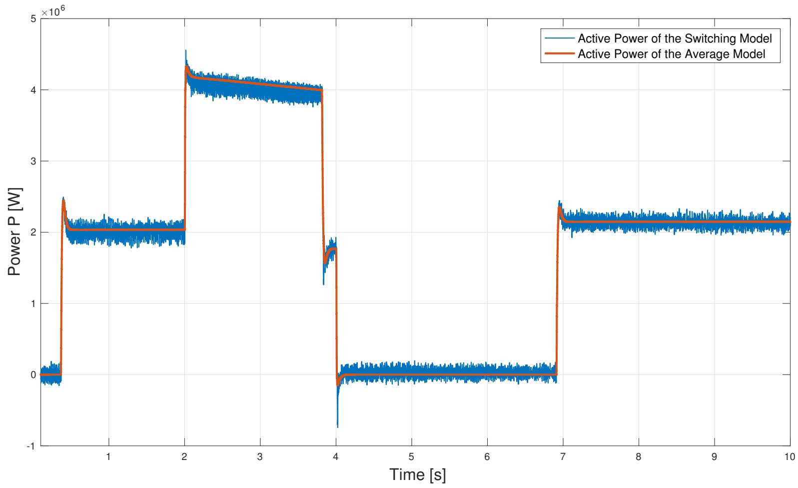

Figure 2.24: The active power production by the switching model and the average model

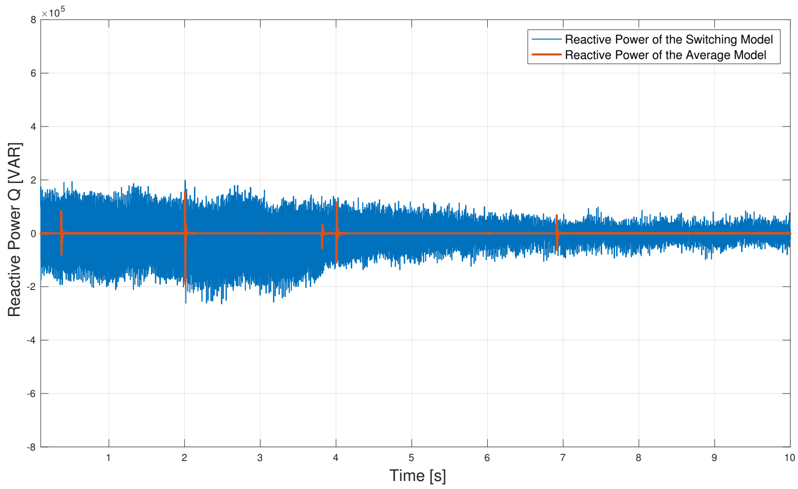

Figure 2.25: The reactive power by the switching model and the average model

2.3.3 Comparison between Switching and Average Model

The explanation of the average model and the results of the simulations show that the main difference between the results of the latter and the switching model is the noise induced by the switching frequency component and its harmonics injected in the grid. In the ideal case scenario, the current and voltage transmitted should be pure sine waves. However, in a realistic case, that wave is distorted, this is called harmonics [29].

The harmonics content of the switching model and the average model can be compared to each other to conclude which changes occur. Figures 2.26, 2.27 and 2.28 present the results concerning the current flowing towards the grid and the power injected into it. The conclusions of these observations are that the harmonics content is considerably reduced with the average model as expected.

The spectrum analyser of Simulink applied to the active power injected into the grid shows that the power is DC as expected. Indeed, the main frequency is $0Hz$. The amplitude of $2MW$ is correct as well.

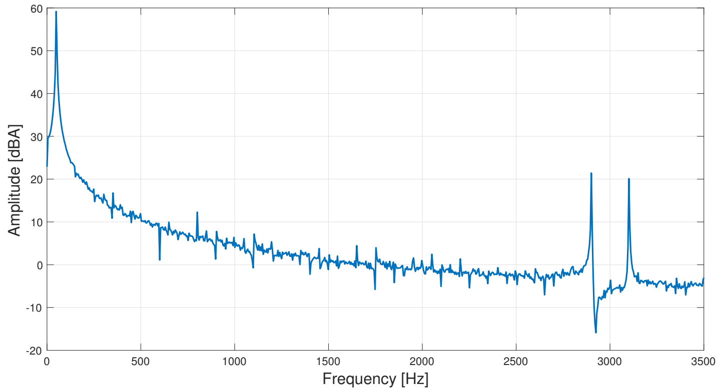

Figure 2.26: Harmonics content of the phase a of the current to the grid of the switching model

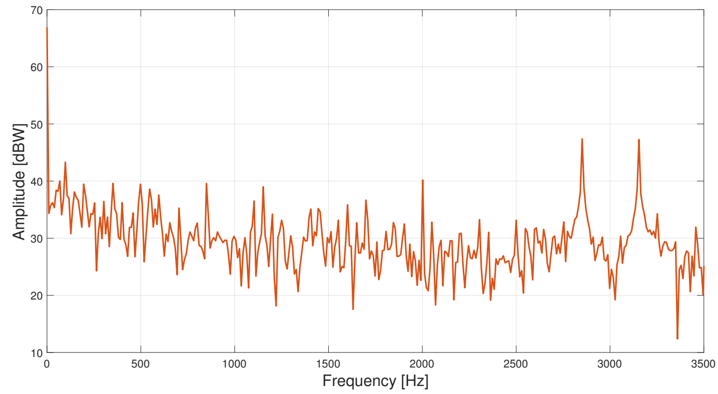

Figure 2.27: Harmonics content of the power transmitted to the grid of the switching model

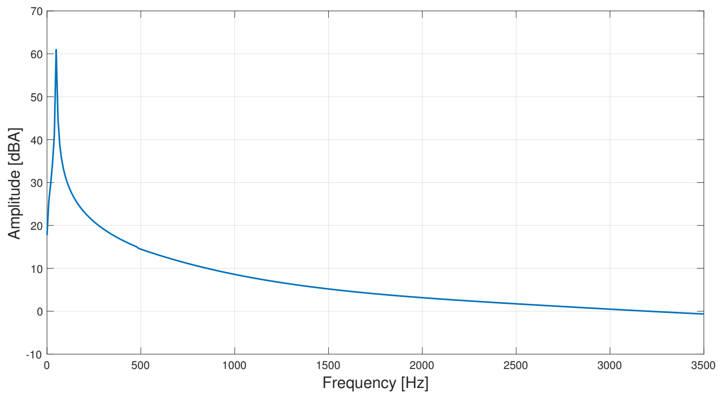

Figure 2.28: Harmonics content of the phase a of the current to the grid of the average model

In the switching model, noises at several frequencies are observed. The analysis of the current flowing to the grid shows that the fundamental frequency is $f_0 = 50Hz$ and noise is observed symmetrically around the frequency of $f_s = 3000Hz$ (at $f_s \pm 2f_0$), which is the switching frequency of the back-to-back converter. The same is observed for the power to the grid. An L-filter is used in this model, however it cannot cancel out completely all the harmonics.

The phase a of the current to the grid has a total harmonic distortion (THD) of 2.535% which is an acceptable amount for a wind turbine. Especially with a choice of asynchronous modulation in the switching model, the THD is set to be higher. When using the average model, that THD has decreased to approximately 0 as the switches are not present any more and do not input noise into the signal.

2.4 Electrical Synchronization between Wind Turbines

Now that one wind turbine is operational with the average model, an entire park can be built. Figure 2.29 presents the detailed scheme of the wind farm. The farm is composed of up to 20 wind turbines with a rated power of $5MW$. The wind turbines each have their own Wind Energy Conversion System (WECS) composed of the PMSG, the back-to-back converter and a small step up transformer. The last item allows to increase the voltage level from $4kV$ to $36kV$, which is the MV level of the local grid.

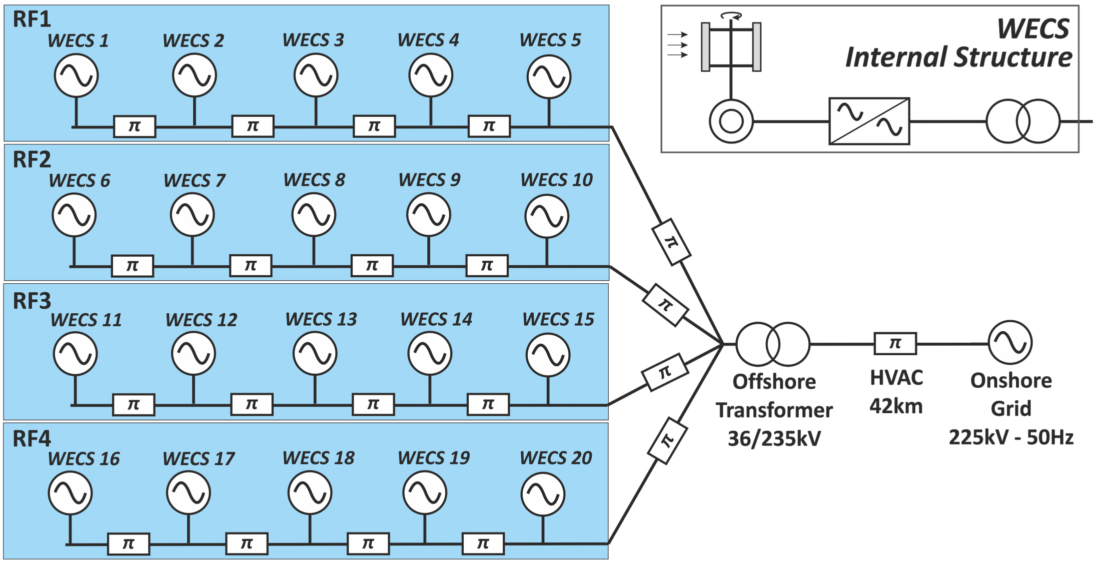

Figure 2.29: Scheme of Total Grid Connection

The lay-out of the farm is radial, that means it is composed of four branches connected to five WECS, called radial feeders (RF) and coloured in blue on Figure 2.29. The RF are gathered at one point before being coupled to an offshore transformer that steps up the voltage from $36kV$ to the level of $235kV$. This allows a less costly transmission of the power to the onshore grid. This transmission is obtained through a HVAC cable. The parameters and motivations for the choices made to create the farm are described in the following subsection.

As explained in the design of the control of the WECS, the reactive power production or compensation is fixed at zero. However the cables of the wind farm inject reactive power into the grid due to their capacitive behaviour. The compensation is also explained in this chapter.

2.4.1 The Parameters of the Connection to the Onshore Point of Coupling

Again, in order to obtain realistic results, data are taken from real components and situations. The Northwind Offshore Wind Farm is situated in the North Sea and is chosen as a typical wind farm to scale the parameters of the components needed for the grid connection. The parameters of this wind farm are gathered in Table 2.4 and the position in the North Sea is shown on Figure 2.30. The parametrisation of each component of the scheme shown in Figure 2.29 is detailed in the following text.

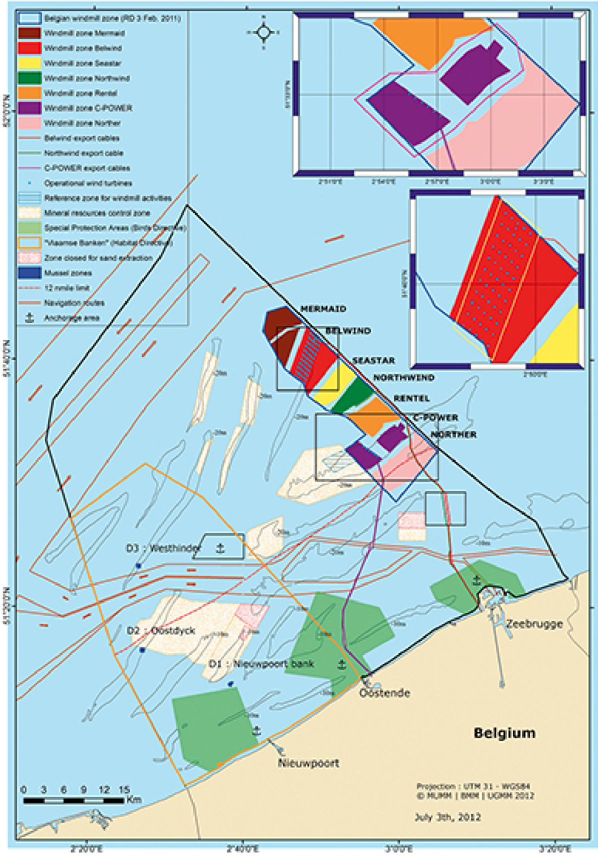

Figure 2.30: Map of the North Sea showing the Northwind Offshore Wind Farm in Dark Green [53]

Table 2.4: Characteristics of the Northwind Offshore Wind Farm [51]

Northwind Characteristics	
Total Capacity	$216MW$
Wind Turbine Capacity	$3MW$
Number of Wind Turbines	72
Distance From Shore	$37km$
10 year Average Wind Speed at $100m$ Height	$10.21m/s$
HVAC Cable	
Average Length of Cable	$42km$
Voltage	$245kV$
Array Cable	
Average Length of Cable	$51km$
Voltage	$36kV$
Offshore Substation	
Big Transformer	$180MVA$ and $225/33kV$

Before getting into the details of the transformers, two aspects should be noted. First, the configuration of the transformers (YD11, YnYg...) has no impact in these simulations as we are dealing with balanced three-phase voltage at both sides. If a specific unbalanced situation were to be simulated, then the most appropriate configuration can easily be implemented. Examples of such situations are faults in the grid, phase shifts, etc. Secondly, no grounding transformer is needed in this type of simulation. As explained in [52], the grounding transformer is the path towards the ground used to maintain the entire system neutral, but more importantly to limit overvoltages and overcurrents during faults. As we are simulating a perfectly balanced case, this type of transformer is not considered.

The Small Transformers

Each wind turbine is connected to the local grid through a small power transformer stepping up the voltage from $4kV$ to $36kV$, as modeled in Figure 2.31. The apparent power has to be more than $5MVA$ as the wind turbine is rated at $5MW$. A typical choice is a power transformer of $6MVA$ with a 10% impedance and a R/X ratio of 0.1.

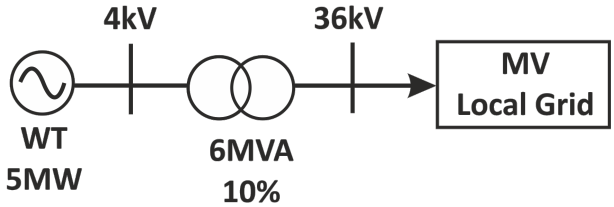

Figure 2.31: Scheme of the modeling of the small transformer

By choosing a base that is the secondary side of the transformer, we have: $S_B = 6MVA$, $V_B = 4/\sqrt{3}kV$ and $Z_B = 8/3\Omega$. This gives the following series impedance:

$$Z_{tf0} = 0.1pu$$

$$R_{tf0} = 0.026533\Omega$$

$$X_{tf0} = 0.26533\Omega$$

The Big Transformer

What is called the big transformer is the transformer between the collector system and the HVAC transmitting the power to the shore. Parameters of scale transformers are difficult to find in the literature. The transformer used in the simulations has a rated power of $180MVA$ and is stepping the voltage from $36kV$ to $235kV$. The characteristics of the small transformer are taken here as well: 10% impedance and a R/X ratio of 0.1.

The Array Cable

As described at the beginning of the subsection, the collector system is composed of underground cables connecting the Wind Energy Conversion Systems (WECS) to the big transformer. These cables form the array cable. As shown in Figure 2.29, the array is composed of 4 RF each connecting 5 WECS at a level of $36kV$.

The parameters required in the SimPowerSystems Π model of the cable are the positive and zero sequence resistance, inductance and capacitance per unit of lenght (km). For more information about symmetrical components, please refer to Appendix B.1. Considering insulated cables, the resistance and capacitance are the most important elements. The inductance is very low due to the proximity of the phases. All of the three elements are influenced by the shield. The cables have one screen per phase in order to keep the field radial as the voltage is quite high. A single core cable is also more easily replaced in case of a fault. The zero and positive sequence of each element can be taken as equal in this case [54].

Data for cables with this level of voltage can be found in [56]. The cable chosen is the $36kV$ Single Core armoured copper conductor. The important features are gathered in Table 2.5.

Table 2.5: Characteristics of the Array Cable [56]

Array Cable	
Voltage Level	$36kV$
Insulation	$XLPE$
Nominal Cross-sectional Area	$1000mm^2$
Continuous current capacity	$860A$
$r_0 = r_1$	$103m\Omega/km$
$c_0 = c_1$	$0.421\mu C/km$
$l_0 = l_1$	$0.317mH/km$

The orders of magnitude of all the parameters are compared to the advised ones given in [55] and are validated as they are in the recommended ranges.

The HVAC Cable

The choice of the HVAC cable is guided by the cost as it should be economical to use. An optimal cross-sectional area can be calculated based on the capital cost of the cable and the running costs provoked by the power losses in the cable. Here, the choice goes to a maximum voltage level of $245kV$ which approximately corresponds to the voltage level of the primary side of the big transformer. The final choice is a single core and XLPE insulated cable. The characteristics are found in Table 2.6. Again a SimPowerSystems Π model is used for the cable.

The parameters were found in [57] and then compared to the values and margins given in [55].

Table 2.6: Characteristics of the HVAC Cable [57]

HVAC Cable	
Voltage Level	$245kV$
Insulation	$XLPE$
Nominal Cross-sectional Area	$2500mm^2$
Continuous current capacity	$1248A$
$r_0 = r_1$	$7.2m\Omega/km$
$c_0 = c_1$	$0.27\mu C/km$
$l_0 = l_1$	$0.328mH/km$

2.4.2 Reactive Power Production and Compensation

As stated before, reactive power is set to zero at the wind energy conversion system level and is produced by the cables of the array and by the HVAC cable. First, the reactive power production is studied theoretically, then the simulation results are shown. For more information about what reactive power is, please refer to Appendix B.3.

The Production of Reactive Power in Theory

The reactive power produced or absorbed at the point of common coupling is directly linked to the voltage stability of the power injected at that point. This is why the reactive power of the farm is an important aspect to study.

The reactive power at WECS level has been controlled to zero. Voltage control with a reactive power command different than zero at wind turbine level is not advised in case of a wind farm where several wind turbines are connected at the same node [38]. However the cables from the collector system and the HVAC cable inject a considerable amount of reactive power into the grid and this calls for compensation.

The stability of the voltage depends on the active power produced by the farm. The dependence can be plotted in the nose or P-V curve [59].

In order to apply reactive power compensation, shunt reactors are used and switched on or off according to the need. This is possible if an estimation of the amount of reactive power produced or absorbed by all the components is known.

Amount of Reactive Power Injected by the Cables

Reactive power can be produced by the shunt capacitance of the cable or absorbed by the series inductance of the cable. From the parameters given in the previous sections of the cables, the capacitive and inductive reactances can be computed.

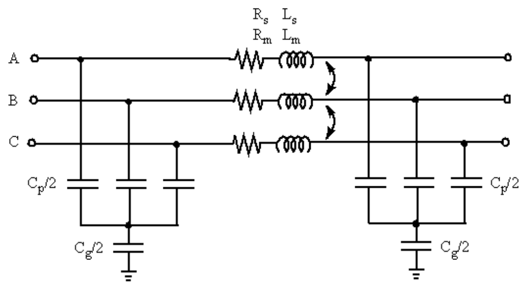

Figure 2.32: π-equivalent scheme of a cable [58]

As the cables correspond to the special case where $c_0 = c_1$ and $l_0 = l_1$, the mutual inductive reactance L_m and the ground capacitive reactance C_g are equal to zero. The inductive and capacitive reactances L_s and C_p are equal to their positive sequence value [58]. As the distances considered are smaller than $50km$, no correction factor is needed.

Considering the production of reactive power, the capacitive reactance is computed as follows:

$$X_C = \frac{1}{N2\pi 50 c_1 d}$$

N is the number of cables and d is the length of the cable. In case of the collector system, N is 4 for the four radial feeders and d is $6km$. For the HVAC cable, N is 1 and d is $42km$.

As the capacitors are parallel elements, the reactive power is calculated as follows:

$$Q_C = \frac{(V)^2}{X_C}$$

where V is the voltage level of the cable.

For the absorption of reactive power, the inductive reactance is:

$$X_L = N2\pi 50 l_1 d$$

Resulting in the following amount of reactive power, taking into account that the inductance is connected in series, so the amount depends on the current flowing through it:

$$Q_L = 3X_L I^2$$

A shunt reactance can be positioned at the point of common coupling in order to compensate the production, its value would be:

$$X_{shunt} = \frac{(V)^2}{Q_{C-collector} - Q_{L-collector} + Q_{C-HVAC} - Q_{L-HVAC}}$$

This time, V is the voltage level where the shunts are positioned.

The value of the shunts depends on the current flowing through the cable where the reactive power is produced or absorbed, however the influence is so small that it is insignificant. An approximation of the reactive power at the point of coupling can be computed by estimating the maximum current that can flow through the cables. This amount is rather constant:

$$Q_{tot} = 200MVAR$$

In this case, the compensation is made of shunt inductive reactors.

The HVAC is the highest injector of reactive power, therefore it is interesting to plot its nose curve. The transformers were not taken into account in the computation, the idea is to get an order of magnitude.

The Influence of the Active Power Production

In order to measure voltage stability around the HVAC cable, as this is the component producing the most reactive power and therefore the one that will induce the most instability, the PV curve, also called nose curve, is plotted.

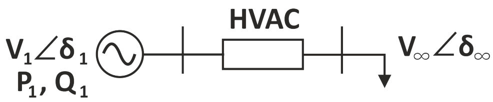

Figure 2.33: The representation of the HVAC cable between the node of the wind farm (1) and the infinite bus (2 or ∞)

The system (shown in Figure 2.33) is made out of two nodes, each described by four state variables V, δ, P and Q. One of the nodes is an infinite bus which is a slack bus as V_∞ and δ_∞ are known and chosen as reference. V_∞ is the nominal voltage of $235kV$ and δ_∞ is set to be equal to zero.

The HVAC cable is characterized by its admittance Y that leads to the admittance matrix with elements Y_{ij} and θ_{ij}, necessary to this study.

The governing equations are the following:

$$P_i = V_i \sum_j V_j Y_{ij} cos(\delta_j - \delta_i + \theta_{ij})$$

$$Q_i = -V_i \sum_j V_j Y_{ij} sin(\delta_j - \delta_i + \theta_{ij})$$

The unknown variables are V_1 and δ_1, the voltage and phase of the wind farm. P_1 is increased from 0 to a little bit over the maximum voltage in order to draw the curve and Q_1 is known through P_1 and the power factor, which is varied as well in order to test stability. The resulting system is non linear and needs to be solved iteratively, with Newton-Raphson for example:

$$\begin{bmatrix} \Delta P \\ \Delta Q \end{bmatrix} = \begin{bmatrix} \frac{\partial P}{\partial \theta} & \frac{\partial P}{\partial V} V \\ \frac{\partial Q}{\partial \theta} & \frac{\partial Q}{\partial V} V \end{bmatrix} \begin{bmatrix} \Delta \theta \\ \frac{\Delta V}{V} \end{bmatrix}$$

In the system, Δ represents the difference between two iterations $i+1$ and i.

Several tests are performed and the results are shown on Figures 2.34 and 2.35. First, only the inductive and capacitive reactances of the cable are considered (Figure 2.34). However, one quickly notices that the capacitance of the cable is insignificant in front of the inductance when the admittance of the cable is considered. Therefore, the capacitive admittance can be neglected. Three power factors are tested: the unity, one lagging and one leading. Results show that the maximum permissible voltage is quite high when considering a unity power factor. It is also the solution to keep a nominal voltage at the bus.

Next, the resistance of the cable is added (Figure 2.35). The maximum permissible injected active power is even higher, and can never be reached considering the 20 wind turbines, so instability is very unlikely to be observed. The resistance has a large influence and the induced voltage variation between the wind farm and the PCC can be as high as $4kV$ when the 20 wind turbines operate at rated power. This is about 1.7% of the nominal voltage. When operating at lagging power factor of 0.95, the maximum allowable active power is $2.33GW$.

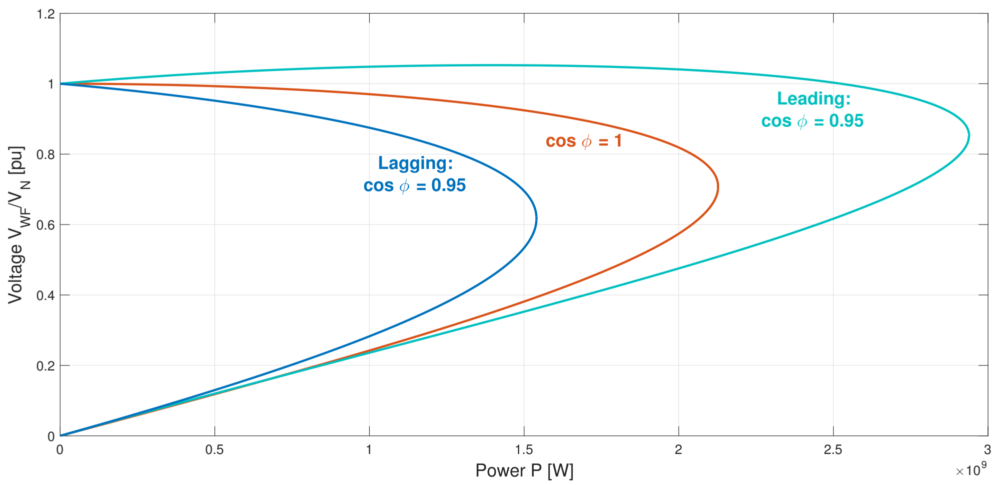

Figure 2.34: The nose curve considering the HVAC is modeled only by an inductive reactance

Compensation

FACTS such as an SVC or a STATCOM could be employed to perform compensation. However the dynamics provided by these solutions is quite high and unnecessary for such a farm. Therefore, a more appropriate solution is to use reactive power compensation banks switched on or off depending on the amount of reactive power injected by the farm.

The goal will be to absorb the reactive power that has been studied in the previous subsections. The maximum possible produced reactive power is computed, from that the highest needed inductive shunt reactor is computed. That reactor value is divided into smaller reactance elements all connected to switches. A control is created to activate or deactivate the switches depending on the level of reactive power flowing from the wind farm. The more reactive power is produced, the more reactance elements are connected.

In order to avoid untimely switching, a time delay is considered. This means, a reactance can be switched on or off only after the new level of reactive power production is estimated as constant and not a small overshoot.

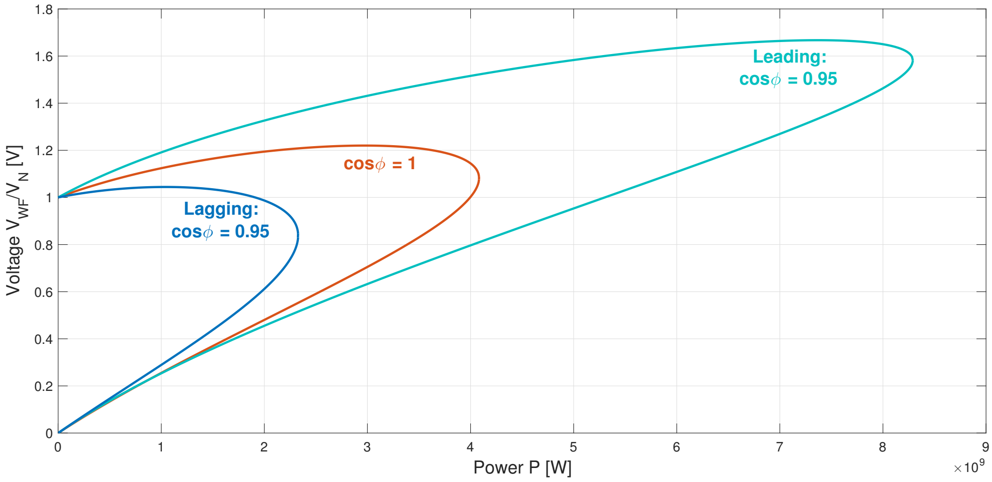

Figure 2.35: The nose curve considering the HVAC is modeled by an inductive reactance and a resistance

This compensation technique makes the assumption that at the point of common coupling, the system operator wants to absorb no reactive power. However, one could imagine that the system operator controls the switching depending on its needs. The compensation was not implemented in this study.

2.4.3 Grid Connection Requirements

The grid connection requirements for generation units are listed in the grid codes by ENTSO-e [64]. They apply to certain power-generating modules depending on the voltage level of their connection point and their maximum capacity. This wind farm is connected at 110kV or above, making it a type D power-generating module. Its maximum capacity is at or above a threshold determined by the synchronous area which is Continental Europe in this case. The threshold is 75MW. The wind farm designed here has a maximum capacity of 100MW obliging it to respect the grid codes [63].

The requirements are related to voltage stability (voltage ranges), robustness (fault-ride-through capability) and system management (voltage, frequency and phase). They can be summarised as follows [62]:

- The wind farm can be required to contribute to voltage control on the network which means a control of reactive power. This can be enabled through a compensation technique as explained before.

- They might be asked to regulate the frequency on the network through active power control. A technique for the wind farm is to regulate the MPPT in order for the wind farm to operate right under the maximum power point. Thereby when the network needs more active power production, the wind farm can inject it.

- In certain conditions of faults, the wind farm is required to operate through it, this is fault-ride-through capability.

- The wind farm will need a wind park control system in order to apply the requirements of the codes.

2.4.4 Simulation Results

The entire simulation has been designed to allow easy usage with other parameters. The blocks are shown in Appendix B.4. The parameters can be easily accessed through the matlab code that can be found in Appendix B.5, and changed in order to simulate a real situation.

The tests are performed on a farm composed of 20 wind turbines with the layout of Figure 2.29. The parameters are the ones of the NREL HAWT and the C_p is the same as the one used for the simulations of one wind turbine. Each wind turbine is distanced by $1km$ from the others. The average model is used to simulate the wind energy conversion system. Five different wind profiles are implemented.

Rotational Speed:

The results show that the connection of the wind turbines does not impact their control. The wind speeds are shown on Figure 2.36 and the rotor speeds on Figure 2.37. For clarity, only the speeds of 5 wind turbines are shown, the colours do correspond to the same wind turbine in the two figures. The response is satisfying and corresponds to the one studied in Section 2.2.3.

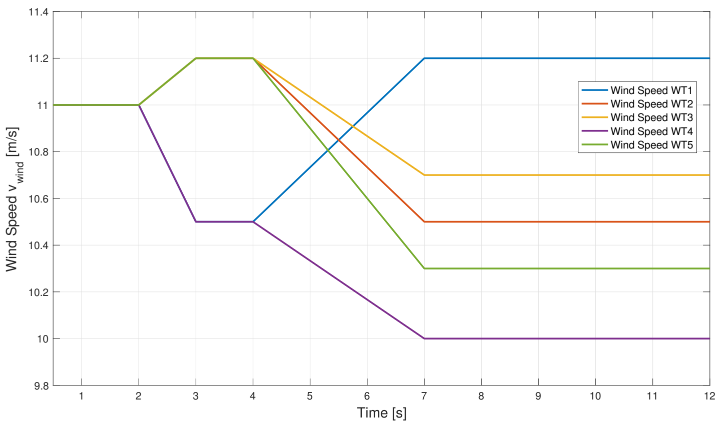

Figure 2.36: The 5 different wind speeds implemented

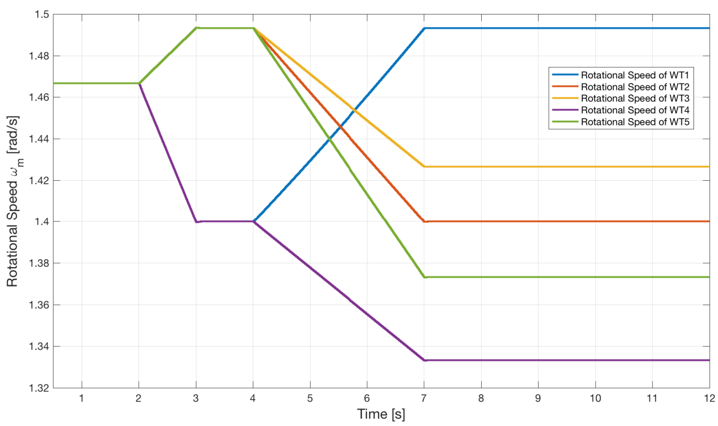

Figure 2.37: The rotational speeds of 5 wind turbines of the farm

Active Power:

The active power has been recorded at different levels of voltage. At the $4kV$ level, the output is the same as shown in Figure 2.24 in Section 2.3.2, as expected. At the levels $36kV$ and at the point of common coupling, the power is shown in Figure 2.38 and 2.39. The active power is multiplied by 4 between the measurement at $36kV$ and the one at the PCC, as there are 4 radial feeders. A bit of noise injected by the HVAC can be observed.

Reactive Power:

At the node right after the wind energy conversion system, an overshoot of active power produced is observed when stabilising or when the state of the system changes. That overshoot is transmitted through the DC link and in turn influences the reactive power injected in the system as shown in Section 2.3.2. They have a maximum amplitude of $500kVAr$ and a frequency of $100Hz$. They are directly linked to the active power production as the oscillations appear at the same moment, however, the amplitude of the ripple does not depend on the active power level.

For the farm, the reactive power is shown at the different voltage levels on Figures 2.40, 2.41 and 2.42. At the point of common coupling, the magnitude of these oscillations amounts $10MVAr$, which is approximately a sum of the ripples created by each wind turbine. Reactive power is injected by the cables of the collector system and by the HVAC cable. A high increase can be observed. The shape, however, stays the same. This confirms the assumption that the cables inject a constant amount of reactive power.

It can be noted that the more active power produced by the wind turbines, the fewer reactive power is injected. This is probably the effect of the transformers which have an impedance that is mostly inductive.

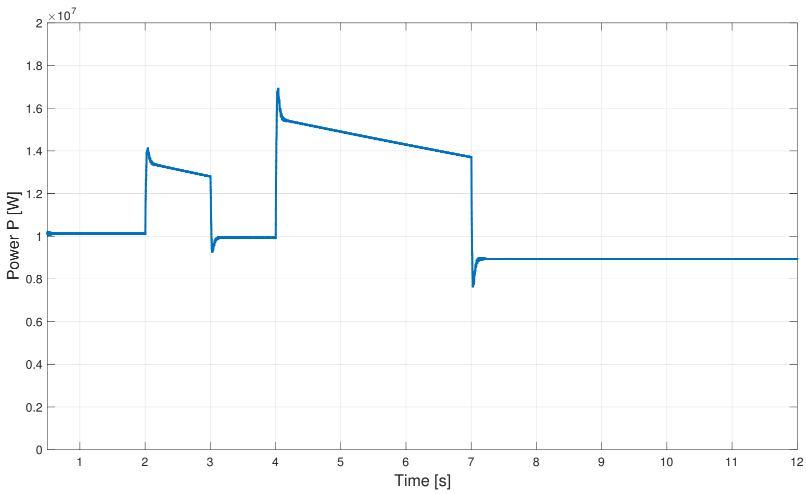

Figure 2.38: The active power produced by radial feeder 1 at the $36kV$ level

2.4.5 Conclusion

In this section, the wind farm layout has been presented as well as the choices of parameters. Then, the reactive power production has been studied considering the major elements of the system.

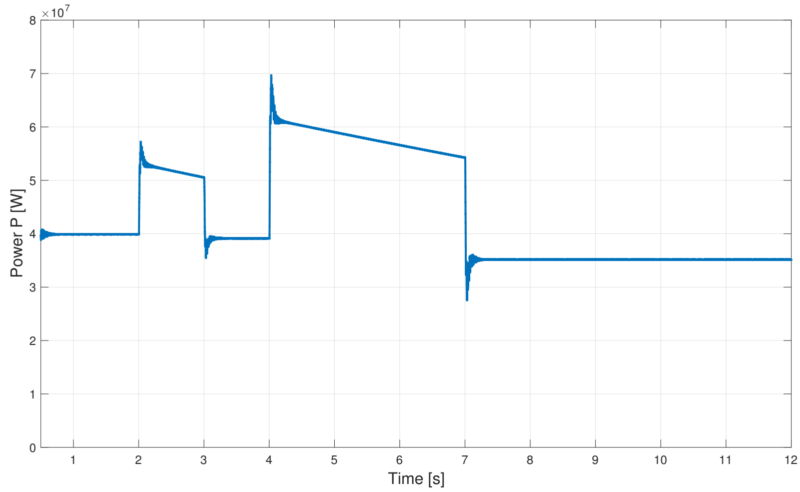

Figure 2.39: The active power produced by the wind farm at the point of common coupling.

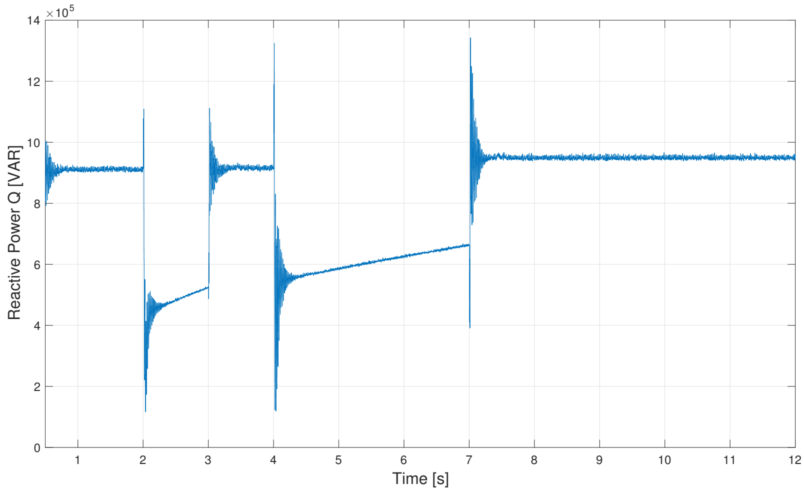

Figure 2.40: The reactive power produced by radial feeder 1 at the $36kV$ level

Next the layout has been tested in simulations involving 20 wind turbines undergoing different winds. It was interesting to observe the active power and reactive power injected into the grid. The results follow the theory described before which allows to conclude positively about the robustness of the simulation.

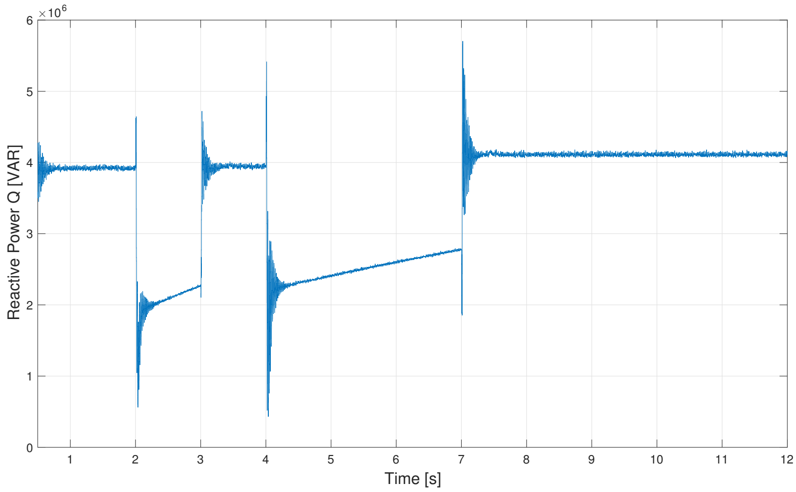

Figure 2.41: The reactive power produced by the wind farm right after the big transformer

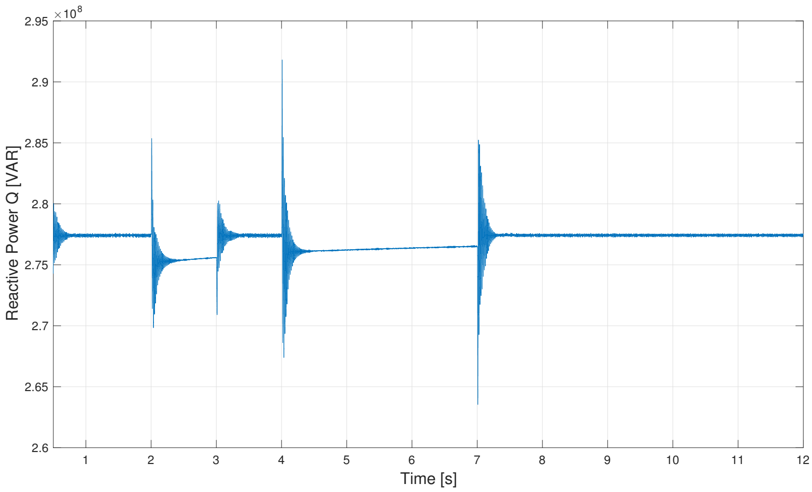

Figure 2.42: The reactive power produced by the wind farm at the point of common coupling.

CHAPTER 3

COUPLING OF ELECTRICAL AND MECHANICAL PARTS

The coupling of the project relies on the same method as the one employed in [32]. It is a one-way procedure: the output of the mechanical part is the input of the electrical part. More particularly, the aero-dynamical torque is used as input of the generator at each time step. A targeted speed, given by the mechanical part, is used as input reference of the generator side controller. The electrical MPPT operates and the resulting speed of the generator is compared to the one obtained by the MPPT of the mechanical part. The coupling is validated if both rotational speeds, mechanical and electrical, are equal. Then, the generated powers are compared. This shows the performance of the Maximum Power Point Tracking of both parts. A scheme clarifying the coupling is shown in Figure 3.1.

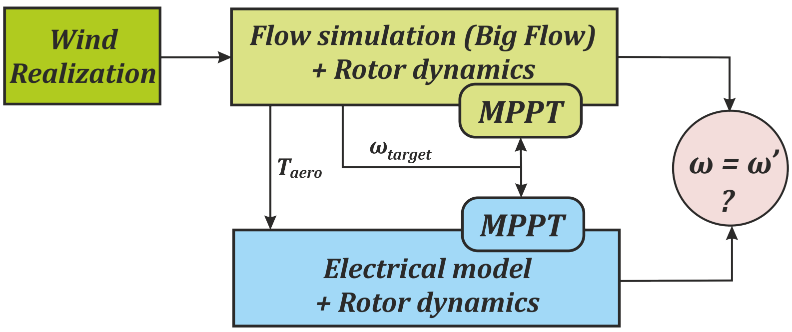

Figure 3.1: Coupling scheme between mechanical and electrical simulations (inspired by [32])

The mechanical MPPT was described previously in Section 1.6.1, while the electrical MPPT was explained in the control of the generator which is in Section 2.2. The coupling is performed on a HAWT farm and a VAWT farm of fifteen wind turbines and same topology. Then, the results are discussed. To conclude, a comparison of HAWT and VAWT farms is presented.

3.1 Method of Coupling

The HAWT farm mechanical results come from the simulations realised with Big Flow, as part of the PhD thesis of M. Moens. This program does not provide an optimal rotational speed and cares for its own MPPT in the same way as in the *NREL* project. However the control is performed thanks to a filtered speed that we can call the targeted rotational speed, ω_{target}, and there is no PI control involved.

Concerning the VAWT farm, an optimal rotational speed as well as a targeted rotational speed are computed, that are then used inside a PI controller.

To allow a comparison as true as possible between the simulation of the HAWT farm and the VAWT farm, the coupling is done as follows: The output torque T_{aero} of the mechanical part is the input of the generator in the electrical part. The Stator Side Controller takes ω_{target} as optimal speed in both cases.

In the case of the HAWT farm, as there is no PI controller, the natural frequency of the speed controller of the SSC is increased and is equal to $20Hz$ in order to follow that speed as closely as possible, as the MPPT is already performed by the mechanical part. In the case of the VAWT farm, the parameters of the speed controller are adapted and equal in the mechanical and electrical simulations.

The results of both farms are presented and discussed in the following sections. In the figures of the power, P_{aero} is the aero power extracted from the wind, P_{mech} is the mechanical power computed by the mechanical simulation (torque times rotational speed) and P_{elec} is the electrical power resulting from the electrical simulation.

3.2 The Simulation of a HAWT Farm

The simulation relates to 15 wind turbines in a radial layout: there are three radial feeders, each connected to five wind turbines. It is interesting to observe whether the rotational speed computed by the mechanical simulation is the same as the one reached by the electrical one. The power is also presented as it is what we want to produce after all. A report for 15 wind turbines would be too long, so that the plot of only one wind turbines will be presented, but the results are similar for each wind turbine.

The rotational speed of one wind turbine is shown on Figure 3.2 and a zoom of a 30-second zone is shown on Figure 3.3. The rotational speed in the electrical simulation is very similar to the one in the mechanical simulation which leads to the conclusion that the coupling succeeded.

The powers shown in Figure 3.4 are the aero power, the mechanical power and the electrical power. The three of them are varying quite similarly, they have the same shape. The P_{elec} and P_{mech} vary in a similar way which shows that both parts (mechanical and electrical) induce the right and the same behaviour. Compared to P_{aero}, they are shifted to the right due to the delay coming from the inertia of the wind turbine and downward due to the efficiency of the machine. However P_{mech} is lower, due to the efficiency chosen in the mechanical part (94%). When computing the efficiency between the aero power and the electrical power, it is found to be 99.65%. The electrical power is measured at the output of the generator which explains the very high efficiency. The efficiencies were computed by taking means of the power across the entire simulation time and by taking a mean over all of the wind turbines.

The active power at the point of coupling can be observed in Figure 3.5. Variations are observed following the injection of active power from the wind turbines. The overshoot that was present during the test simulations (presented in Section 2.3.2) are not observed anymore. In Figure 3.6, the reactive power is quite constant as there is no high variation in active power.

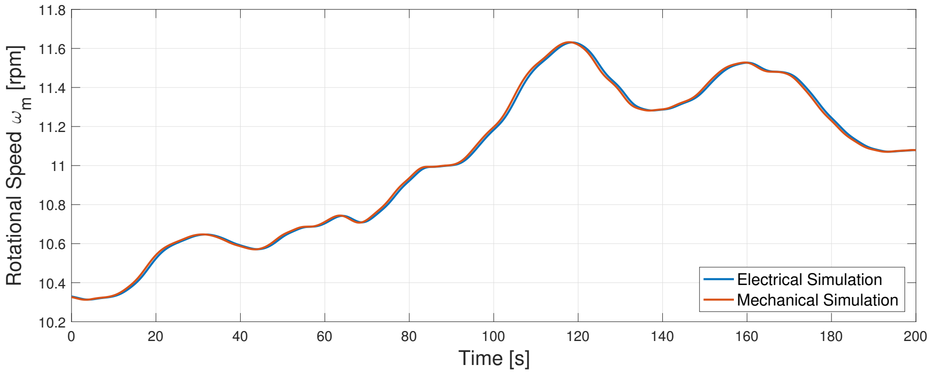

Figure 3.2: HAWT: The rotational speed of one wind turbine over the whole simulation time

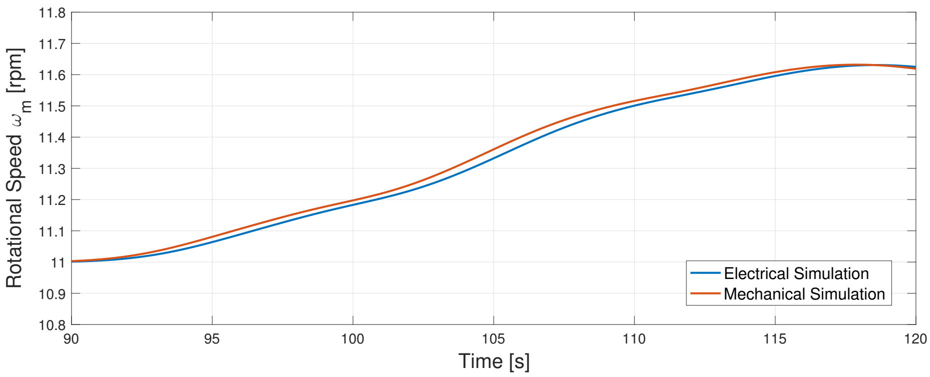

Figure 3.3: HAWT: The rotational speed of one wind turbine over 30s of simulation time

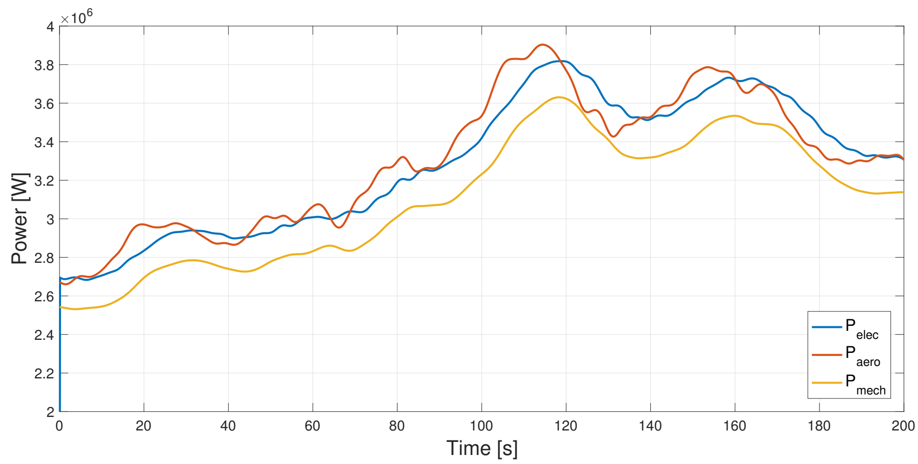

Figure 3.4: HAWT: aero, mechanical and electrical powers

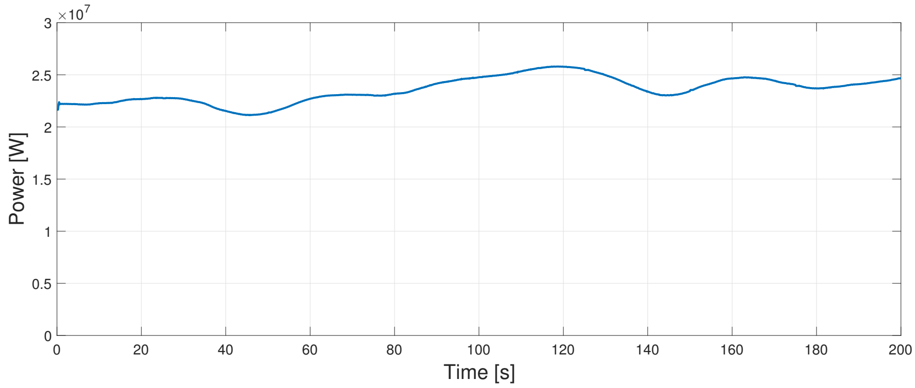

Figure 3.5: HAWT: The active power at the point of coupling

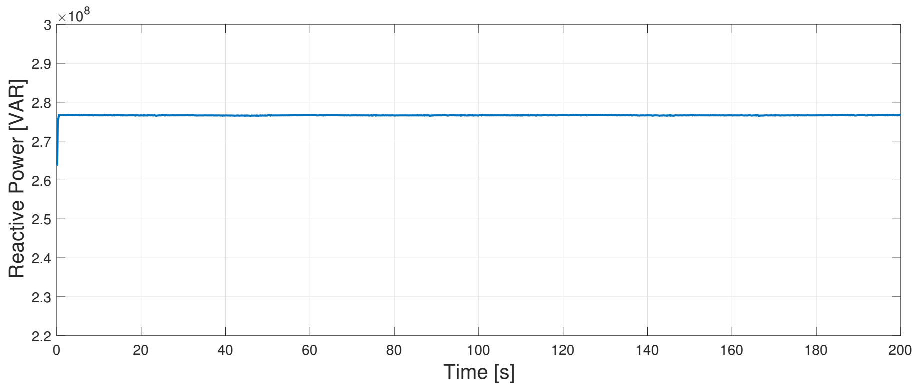

Figure 3.6: HAWT: The reactive power at the point of coupling

3.3 The Simulation of a VAWT Farm

Similarly, 15 wind turbines are simulated in a radial layout and only the results of the first one are presented. In order to validate the coupling, the rotational speed of the mechanical simulation is compared to the one of the electrical one. The results (shown in Figure 3.7 and zoomed in Figure 3.8) are satisfying the condition as they follow each other very closely. One can conclude that the coupling is a success in case of a VAWT as well.

In Figure 3.9, the aero, the mechanical and the electrical powers are plotted. The P_{aero} varies the most, while P_{mech} and P_{elec} are a smoothed and shifted to the right version of that power. This is due to the inertia of the VAWT. In these simulations, no power conversion efficiency was implemented in both mechanical and electrical simulations, so the computation of the efficiency gives approximately a 100% between aero and electrical, as well as between aero and mechanical.

The electrical power computed by the mechanical simulation (P_{mech}), is the same as P_{elec}, which means the control implemented in both simulations is similar. This confirms the coupling once again.

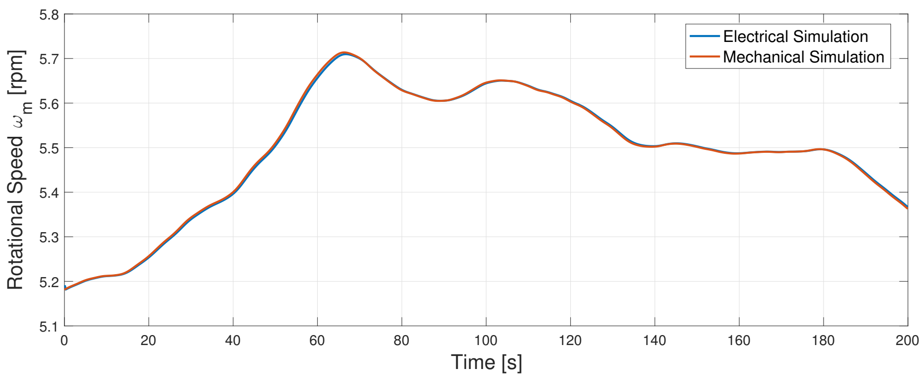

Figure 3.7: VAWT: The rotational speed of one wind turbine over the whole simulation time

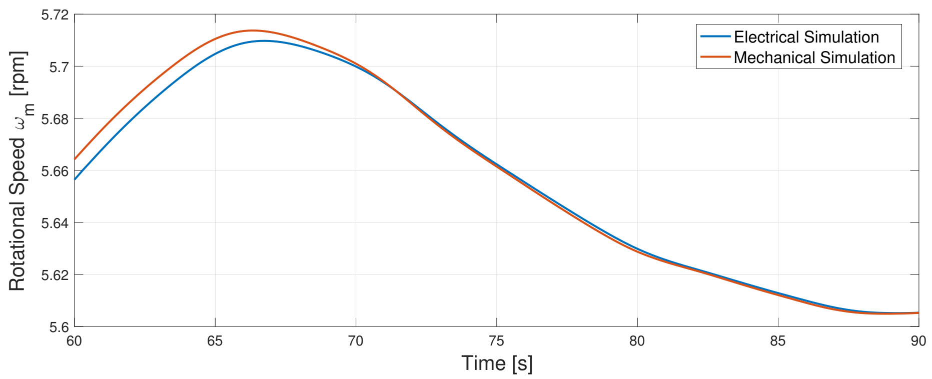

Figure 3.8: VAWT: The rotational speed of one wind turbine over 30s of simulation time

The active and reactive powers at the point of coupling are shown on Figures 3.10 and 3.11, respectively. The active power varies according to the injection of the different wind turbines. Concerning the reactive power, the injection is constant and no variation is observed.

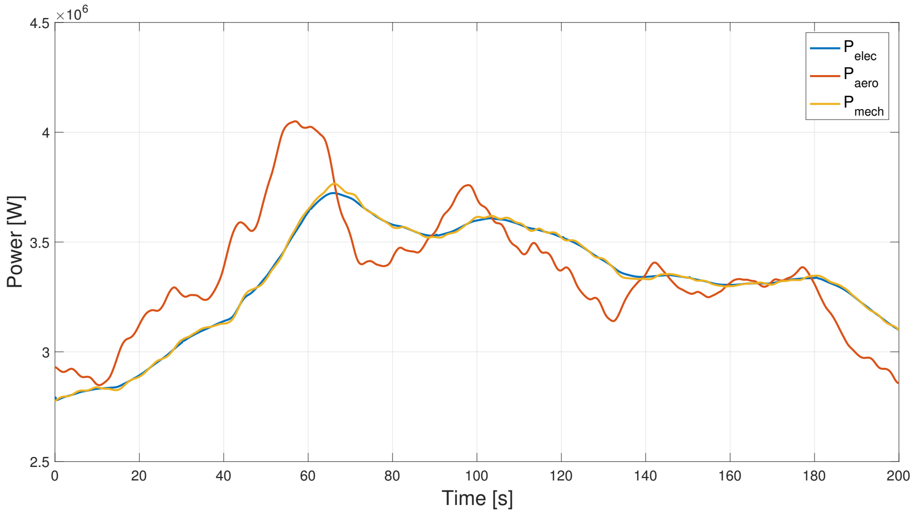

Figure 3.9: VAWT: aero, mechanical and electrical powers

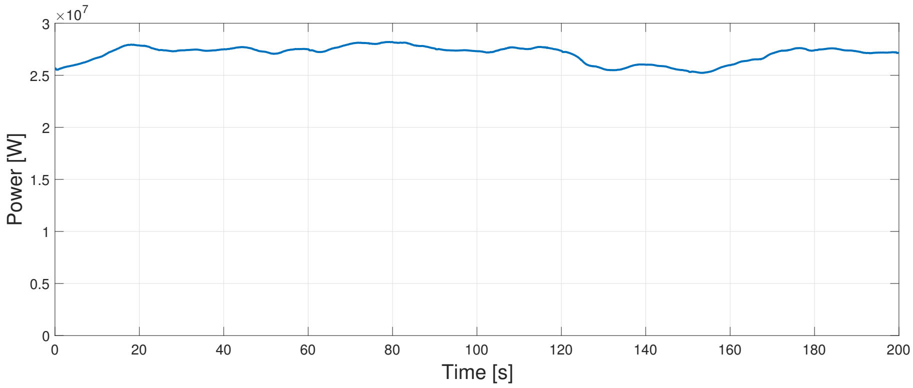

Figure 3.10: VAWT: The active power at the point of coupling

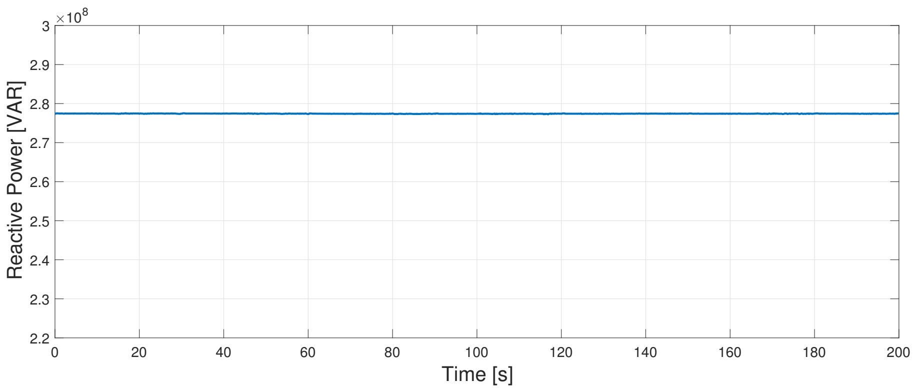

Figure 3.11: VAWT: The reactive power at the point of coupling

3.4 Comparison between the HAWT Farm and the VAWT Farm

The results of the HAWT farm can be compared to the ones of the VAWT farm.

Concerning the electrical simulations of both farms, the coupling is a success proving that farms can be developed and tested in simulations with a one way method (the output of the mechanical part is the input of the electrical part.

The variation in rotational speed, considered relatively to the nominal speed, is the same for both types of wind turbines. However the generated power is smoother in case of the VAWT due to the higher inertia of the turbine.

Figures 3.12 and 3.13 show a comparison between the power generated for the 15 wind turbines in each case. The first observation is the drastic decrease between the first line of wind turbines and the upcoming ones. This is due to the layout and the fact that the most adverse scenario is simulated. Secondly, for the HAWT farm, the power is generally decreasing when the turbine is more downstream than the previous one. However, for the VAWT farm, the second wind turbine experiences a large decrease, smaller than in the second HAWT, while the power production increases slightly afterwards.

The total mean active power production of the HAWT farm is 23.6 MW while it is 26.7 MW for the VAWT farm. The production of the HAWTs is only 88.4% from that of the VAWTs, while both farms were experiencing the same upstream wind. This is due to the unrealistic mechanical model leading to a high power coefficient, as explained in Section 1.5. The reactive power injection is the same in both farms.

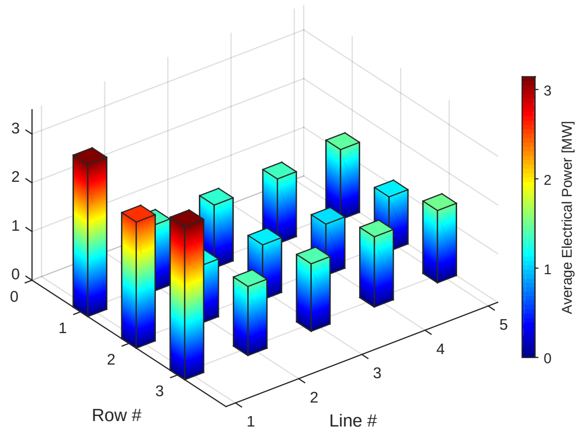

(a) HAWT

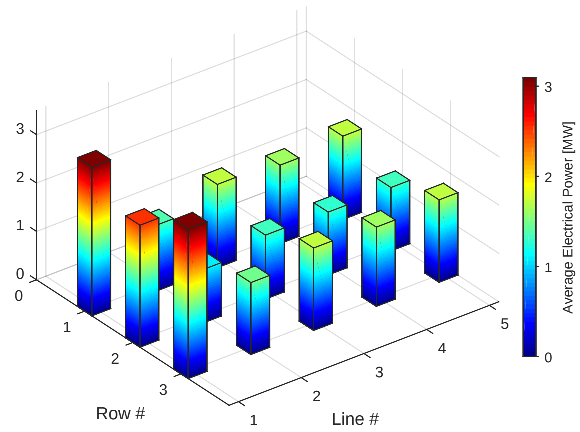

(b) VAWT

Figure 3.12: Mean Electrical power generation per wind turbine

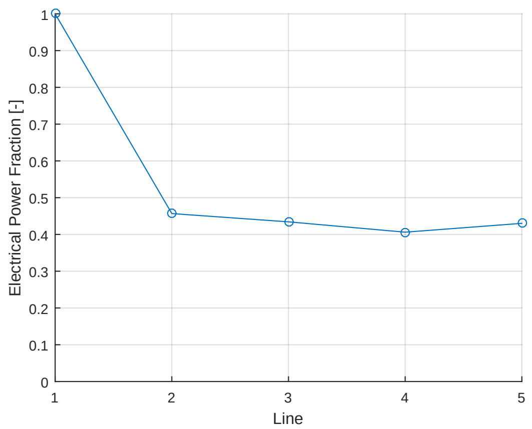

(a) HAWT

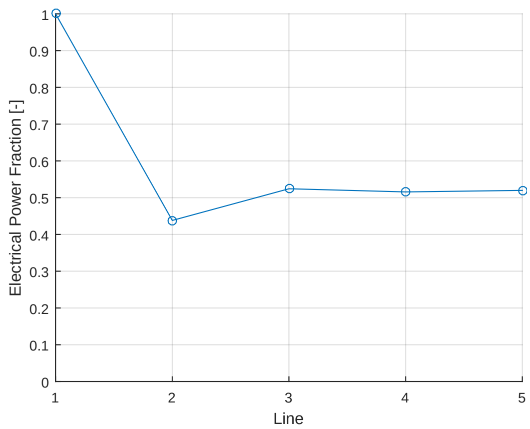

(b) VAWT

Figure 3.13: Fraction of mean electrical power generation on the central row with regards to the first line wind turbine

CONCLUSION AND FURTHER POSSIBLE DEVELOPMENTS

The objective of the project was to design a study of the power conversion in a VAWT farm from the wind resource to the electro-mechanical conversion and to compare it to the processes of a HAWT farm.

The aerodynamic study of VAWTs at the scale of an offshore farm has proven to be doable, yet the original momentum-based model has shown more limitations than initially thought, and has required the use of reference data to be tuned with. The complex aerodynamics of VAWTs is only partially covered by the current model, leading to overestimations of their performances. Then, an up-scaling method was developed and thoroughly discussed, facilitating potential future studies. Besides, A control scheme has been integrated in the model to allow a one-way coupling with electrical simulations.

Considering further possible developments, the use of a more detailed aerodynamic model that would allow for the computation of forces without the constrained order of calculation set by the stream tubes distribution, and their induction factors, would allow for a simpler yet more accurate approach to the computation of dynamic effect of the airfoil motion. This improvement, coupled other previously modelled effects like tip loss effect, flow curvature and variable pitch, could improve greatly the performance prediction of VAWTs in the future.

Secondly, the electro-mechanical conversion chain was described including the definition of the parameters of the control. With the goal of the wind farm in mind, the computation time needed to be reduced. Therefore, the average model has been drafted. When the model was validated, the farm could finally be set up. Different parameters were determined and studied in order to create a robust simulation.

Concerning the electrical part of the work, several further developments are possible in order to represent the real behaviour of the system. First, the reactive power compensation technique can be easily implemented as that injection is quite constant. The solution of the inductance banks seems to be the most adequate solution. Secondly, in order to test the stability and robustness of the farm, some faults could be implemented (in the radial feeders for example), and an imbalanced system and transient states could be more thoroughly studied. Finally, a wind park control system can be implemented in order to respect the requirements of the grid codes.

In the last chapter, the coupling of both the mechanical study and the electro-mechanical conversion was performed using a mechanical MPPT and an electrical MPPT with the same behaviour. It was concluded that this method leads to a reliable coupling as the controls did operate correctly leading to the correct speed output of both sides. From the comparison of the tests on both farms, it is difficult to confirm any technical advantages of choosing for VAWTs over HAWTs in case of offshore wind farms. Indeed, the increase in power output when using the former is due to the unrealistic mechanical model. However, as explained in the second chapter, the construction and O&M costs would be lowered, which could lead to a lower LCOE.

The most significant future development would be to couple the mechanical and electrical study back and forth. The control would be managed by the electrical part exclusively leading the turbine (in the mechanical part) to reach the right speed. However, one could wonder if it is worth the drastic increase in computational cost, as the study has proven the one way coupling to be robust.

BIBLIOGRAPHY

[1] "IEA Wind Annual Report", 2015, p92.

[2] J Watanabe, "Giant Fall in Generating Costs from Offshore Wind", *Bloomberg New Energy Finance*, 2016.

[3] H. Polinder, F.F.A. van der Pijl, G-J. de Vilder, P.J. Tavner, "Renewable Energy Technologies: Cost Analysis Series: Wind Power", *International Renewable Energy Agency: Volume 1: Power Sector - Issue 5/5*, 2012.

[4] C. Röckmann , S. Lagerveld, J. Stavenuiter, "Operation and Maintenance Costs of Offshore Wind Farms and Potential Multi-use Platforms in the Dutch North Sea". Online. `https://link.springer.com/chapter/10.1007/978-3-319-51159-7_4/fulltext.html`. Consulted : 20 May 2017.

[5] Q. Taverne, "Modélisation par forces surfaciques d'éoliennes à axe vertical", *UCL, Université catholique de Louvain*, 2015.

[6] M. Donnay, Q. Lallemand, "Conception d'un aérogénérateur à axe vertical fabricable par des techniques de prototypage rapide", *UCL, Université catholique de Louvain*, 2016.

[7] E. Kulunk, "Fundamental and Advanced Topics in Wind Power", Aerodynamics of Wind Turbines, 2011.

[8] I. Paraschivoiu. "Wind turbine design: with emphasis on Darrieus concept". Presses inter Polytechnique, 2002.

[9] W. Tjiu, et al. "Darrieus vertical axis wind turbine for power generation I: Assessment of Darrieus VAWT configurations." Renewable Energy 75 : 50-67, 2015.

[10] M.O.L. Hansen, et al. "State of the art in wind turbine aerodynamics and aeroelasticity." Progress in aerospace sciences 42.4 : 285-330, 2006.

[11] C. E. Soraghan. "Aerodynamic modelling and control of vertical axis wind turbines", *Diss. University of Strathclyde*, 2014.

[12] S. Ferreira, "The near wake of the VAWT: 2D and 3D views of the VAWT aerodynamics", *Diss. TU Delft, Delft University of Technology*, 2009.

[13] C. E. Soraghan, et al. "Double multiple streamtube model for variable pitch vertical axis wind turbines." 31st AIAA Applied Aerodynamics Conference, 2013.

[14] J. W. Oler, et al. "Dynamic stall regulation of the Darrieus turbine". Sandia National Labs., Albuquerque, NM (USA), 1983.

[15] R.E. Sheldahl, P.C. Klimas. "Aerodynamic characteristics of seven symmetrical airfoil sections through 180-degree angle of attack for use in aerodynamic analysis of vertical axis wind turbines". No. SAND-80-2114. Sandia National Labs., Albuquerque, NM (USA), 1981.

[16] P. Chatelain, et al. "Large eddy simulation of wind turbine wakes." Flow, turbulence and combustion 91.3: 587-605, 2013.

[17] P. Chatelain, M. Duponcheel, D.-G. Caprace, Y. Marichal, and G. Winckelmans, "Vortex Particle-Mesh simulations of Vertical Axis Wind Turbine flows: from the blade aerodynamics to the very far wake", Wind Energ. Sci. Discuss., https://doi.org/10.5194/wes-2016-56, in review, 2017.

[18] R. Sheldahl, and P. Klimas. "Aerodynamic characteristics of seven symmetrical airfoil sections through 180-degree angle of attack for use in aerodynamic analysis of vertical axis wind turbines". No. SAND-80-2114. *Sandia National Labs.*, Albuquerque, NM (USA), 1981.

[19] J. Jonkman, et al. "Definition of a 5-MW reference wind turbine for offshore system development." National Renewable Energy Laboratory, Golden, CO, Technical Report No. NREL/TP-500-38060, 2009.

[20] M. Moens, M. Duponcheel, G. Winckelmans, and P. Chatelain, "LES of wind farm response to transient scenarios using a high fidelity actuator disk model." *Journal of Physics: Conference Series*. Vol. 753. No. 3. IOP Publishing, 2016.

[21] C. Galinos, "Study of Design Load Cases for Multi-Megawatt Onshore Vertical Axis Wind Turbines." *European Wind Energy Master Thesis*, Roskilde, Denmark, 2015.

[22] G. Sieros, et al. "Upscaling wind turbines: theoretical and practical aspects and their impact on the cost of energy." Wind energy 15.1 : 3-17, 2012

[23] U.S. Paulsen, et al. "DeepWind-from idea to 5 MW concept." Energy Procedia 53 : 23-33, 2014.

[24] N. Chrysochoïdis-Antsos, "The conceptual design of a safety system : For the 5MW Deepwind wind turbine". Delft University of Technology 23 : 04, 2014

[25] D. Bang, H. Polinder, G. Shrestha, J.A. Ferreira, "Review of Generator Systems for Direct-Drive Wind Turbines", *Electrical Power Processing/DUWIND, Delft University of Technology, Delft*, 2008.

[26] H. Polinder, F.F.A. van der Pijl, G-J. de Vilder, P.J. Tavner, "Comparison of direct-drive and geared generator concepts for wind turbines", *IEEE transactions on energy conversion, vol. 21, no. 3, August, pp.725-733*, 2006.

[27] Md. Rabiul Islam Youguang Guo Jianguo ZhuA, "Review of Offshore Wind Turbine Nacelle: Technical Challenges, Research and Development Trends", *Centre for Electrical Machines and Power Electronics, University of Technology Sydney*, 2007.

[28] Leban K.M., "Design Tool for Direct Drive Wind Turbine Generators: Proposed solutions for direct drive Darrieus generators 20MW", *Department of Energy Technology, Aalborg University*, 2014.

[29] F. Santjer, G.J. Gerdes, P. Christiansen, D. Milborrow, "Wind Turbine Grid Connection and Interaction", *General Information, European Commission*, 2001.

[30] Z. Chen, "Issues of Connecting Wind Farms into Power Systems", *IEEE/PES Transmission and Distribution Conference & Exhibition*, 2005.

[31] A. Sudria, M. Chindris, A. Sumper, G. Gross, F. Ferrer, "Wind Turbine Operation in Power Systems and Grid Connection Requirements", *Renewable Energy and Power Quality Journal, vol. 1, no. 3*, 2005.

[32] M. Duponcheel, C. Leroi, S. Zeoli, G. Winckelmans, L. Bricteux, P. Chatelain, E. De Jaeger, "Small wind turbines: a study of the full conversion chain", *Université Catholique de Louvain-la-Neuve*, 2016.

[33] J. Driesen, "Electrical Aspects of Wind Turbine Drives", *Course : "Electrical Drives", KULeuven, Belgium*, 2016.

[34] V. Delli Colli, F. Marignetti, C. Attaianese, "Analytical and Multiphysics Approach to the Optimal Design of a 10-MW DFIG for Direct-Drive Wind Turbines", *IEEE Transactions on Industrial Electronics, vol. 59, no. 7, pp.2791-2799*, 2012.

[35] Josef Schachner, "Power Connections for Offshore Wind Farms", *TU Delft - Diploma Thesis*, 2004.

[36] Wikipedia, "Doubly-Fed Electric Machine". Online. `https://en.wikipedia.org/wiki/Doubly-fed_electric_machine`. Consulted : 10 November 2016.

[37] A.M. Hemeida Wael, A. Farag, O.A. Mahgoub, "Modeling and Control of Direct Driven PMSG for Ultra Large Wind Turbines", *International Journal of Computer, Electrical, Automation, Control and Information Engineering, vol. 5, no. 11, pp.1269-1275*, 2011.

[38] T. Mercier, "Participation of Wind Turbine Generators to Voltage Control in Power Systems", *Université Catholique de Louvain*, 2013.

[39] A. Carlsson, "The Back To Back Converter, Control and Design", *Lund Institute of Technology*, 1998.

[40] G. Terörde, "Electrical Drives and Control Techniques", *Handbook*, 2004.

[41] E. De Jaeger, "Synchronous Machines", *Course : "LELEC2753 - Electrical Energy Systems : Advanced Topics", Université Catholique de Louvain, Belgium*, 2017.

[42] Nikolaos Chrysochoïdis-Antsos, "The conceptual design of a safety system: For the 5MW Deepwind wind turbine", *TU Delft - Master in Science Thesis*, 2014.

[43] Majid A. Abdullah, A.H.M. Yatim, Chee Wei, Tan, "A Study of Maximum Power Point Tracking Algorithms for Wind Ener System", *IEEE First Conference on Clean Energy and Technology CET, Department of Energy Conversion Universiti Teknologi Malaysia*, 2011.

[44] Manish Bhardwaj, "Software Phase Locked Loop Design Using $C2000^{TM}$ Microcontrollers for Single Phase Grid Connected Inverter", *Texas Instrument Incorporated - Application Report, SPRABT3*, July 2013.

[45] Jim Ögren, "PLL design for inverter grid connection - Simulations for ideal and non-ideal grid conditions", *Uppsala University*, July 2011.

[46] P.O. Ohiero, C. Cossar, J. Melone, "A Fast Simulation Model for a Permanent Magnet Synchronous Generator (PMSG) Drive System", *School of Engineering, University of Glasgow, UK*, 2015.

[47] P.O. Ohiero, "Development of Fast Multi-System Simulation Models for Permanent Magnet Synchronous Motor and Generator Drive Systems", *School of Engineering, University of Glasgow, UK*, July 2015.

[48] Diah Septi Yanaratri, Mochamad Ashari, Dedet C. Riawan, "Modelling Fullscale Converter Type 4 with Average Model in Wind Power System Using PMSG", *Department of Electrical Engineering, Institut Teknologi Sepuluh Nopember, Surabaya, Indonesia*, ???.

[49] Anisa Harumwidiah, Mochamad Ashari, and Dedet C. Riawan, "Modelling Back-to-Back Converter with Average Model in Wind Power System using DFIG", *IPTEK, Journal of Proceeding Series, Vol. 1*, 2014.

[50] Hua Ye, Juan Su, Songhuai Du, "Simulation and Analysis of PMSG-based Wind Energy Conversion System using Different Coverter Models", *Published Online - Scientific Research*, January 2013.

[51] Orbis Energy Center, "4C Offshore - Northwind Offshore Wind Farm". Online. `http://www.4coffshore.com/windfarms/northwind-belgium-be02.html`. Consulted : 3 March 2017.

[52] Pacific Crest Transformers, "Grounding Transformer FAQs". Online. `https://www.pacificcresttrans.com`. Consulted : 11 March 2017.

[53] DEME, "Belgian contractor for Northwind Wind Farm". Online. `http://www.deme-group.com/news/belgian-contractor-northwind-wind-farm`. Consulted : 7 March 2017.

[54] Dirk Van Hertem, "Parameters of grid elements: lines and cables", *Course H04A9A: Power System Calculations*, February 2016.

[55] Benoît de METZ-NOBLAT, "Cahier technique n° 18: Analyse des réseaux triphasés en régime perturbé à l'aide des composantes symétriques", *Schneider Electric*, June 2005.

[56] "6-36kV Medium Voltage Underground Power Cables - XLPE insulated cables", *Nexans Energy Networks*, 2009.

[57] "High Voltage Cables", *Prysmiam Cables and Systems B.V.*, Consulted: April 2017.

[58] Simulink - SimPowerSystems, "Three-Phase PI Section Line". Online. `https://nl.mathworks.com/help/physmod/sps/powersys/ref/threephasepisectionline.html`. Consulted : 15 May 2017.

[59] Snehal B. Bhaladhare, A. S. Telang, Prashant P. Bedekar, "P-V, Q-V Curve – A Novel Approach for Voltage Stability Analysis", `NationalConferenceonInnovativeParadigmsinEngineering&Technology`. 2013.

[60] Thomas Ackermann, "Wind Power in Power Systems", *Handbook, Royal Institute of Technology Stockholm, Sweden*, 2005

[61] Panos M. Pardalos, Steffen Rebennack, Mario V. F. Pereira, Niko A. Iliadis, Vijay Pappu, "Handbook of Wind Power Systems", *Handbook, Energy Systems, Springer*, 2013

[62] María Paz Comech, Miguel García-Gracia, Susana Martín Arroyo and Miguel Ángel Martínez Guillén, "Wind Farms and Grid Codes", *CIRCE-University of Zaragoza Spain*, 2011

[63] The European Commision, "Regulations: Establishing a Network Code on Requirements for Grid Connection of Generators", *Official Journal of the European Union - regulation (EU) 2016/631*, 27.4.2016

[64] Elia, "Implementation EU Network Codes". Online. `http://www.elia.be/en/users-group/Implementation-EU-Network-Codes`. Consulted : 26 May 2017.

[65] Richard Gagnon, "Simscape Power Systems Examples - Renewable Energy - Wind Farm (IG)", *Matlab - Simulink - Hydro-Quebec*, Consulted: February 2017.

[66] Richard Gagnon, Jacques Brochu, "Simscape Power Systems Examples - Renewable Energy - Wind Farm - Synchronous Generator and Full Scale Converter (Type 4) Detaield and Average Model", *Matlab - Simulink - Hydro-Quebec*, Consulted: March 2017

[67] Dirk Van Hertem, "Per-unit calculations and Unbalanced systems: the symmetrical components", *Course H04A9A: Power System Calculations*, February 2016.

[68] A. Amberg, A. Rangel, "Tutorial on Symmetrical Components: Part 2 - Anwser Key", *Schweitzer Engineering Laboratories, Inc.*, 2014.

[69] Fault Calculation - Symmetrical Components Online. `http://myelectrical.com/notes/entryid/213/fault-calculation-symmetrical-components`. Consulted : 30 May 2017.

[70] Direct-quadrature-zero transfomation Online. `https://en.wikipedia.org/wiki/Direct-quadrature-zero_transformation#The_Park_transform_derivation`. Consulted : 15 May 2017.

[71] "AC Power". Online. `https://en.wikipedia.org/wiki/AC_power`. Consulted : 15 May 2017.

APPENDIX A

MECHANICAL PART

A.1 Convergence of the DMST Method

Detailed results of the convergence study are provided hereafter for angle of attack α, normal, $F_n/(cq_0)$, and tangential, $F_t/(cq_0)$, force coefficients.

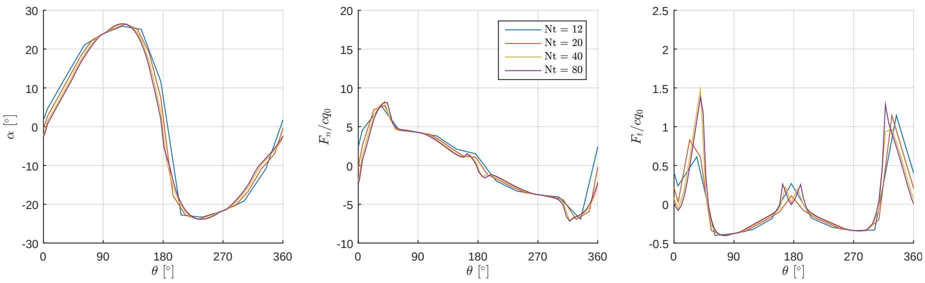

(a) TSR = 2.14

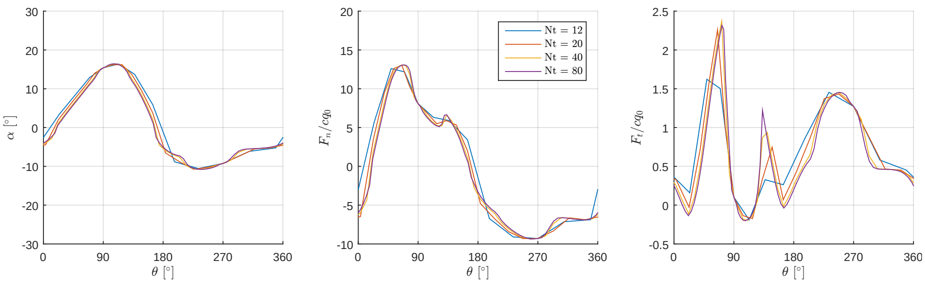

(b) TSR = 3.21

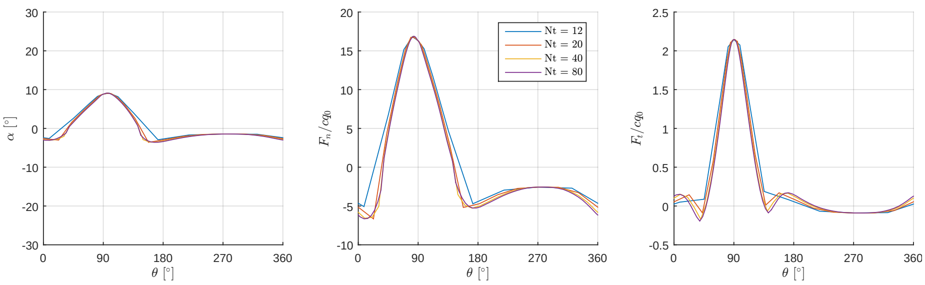

(c) TSR = 4.28

Figure A.1: Convergence of the DMST Method

APPENDIX B

ELECTRO-MECHANICAL CONVERSION AND GRID CONNECTION

B.1 The Per Unit System and Symmetrical Components

The per-unit system and the symmetrical components are essential concepts to understand the power system [68]. In this master thesis, the per-unit system is used to describe the parameters of the synchronous generator and the parameters of the cables are given in symmetrical components.

B.1.1 The Per Unit System

Any quantity can be expressed in *pu* (the unit of the per-unit system) by taking the ratio of that quantity to its base [67].

$$\text{per-unit value } [pu] = \frac{\text{real value [physical units]}}{\text{base [physical units]}}$$

The quantity can either be a voltage, a current, a power or an impedance. To model the power system, two of these quantities must be fixed. When the base changes, a conversion between the bases is used.

The per unit system makes calculations at different voltage levels easier, this is useful as there are many different voltage levels in the power system. The comparison between the quantities makes more sense as well.

B.1.2 The Symmetrical Components

In order to facilitate the resolution of unbalanced systems, such as systems that go through short circuit faults, symmetrical components are used. In this master thesis, the system considered is balanced, however the data found to represent the cables are the symmetrical components.

The symmetrical commponents are based on Fortescue's paper proving that a 3-phase system results in 3 balanced systems with as condition that the system should be linear [67].

The symmetrical components are:

- the positive-sequence (direct component): 3 phasors of equal magnitude, a 120° phase difference, turning clockwise.
- the negative-sequence (indirect): 3 phasors of equal magnitude, a 120° phase difference, turning counter clockwise.
- the zero-sequence (homopolar): 3 phasors of equal magnitude and a zero phase difference.

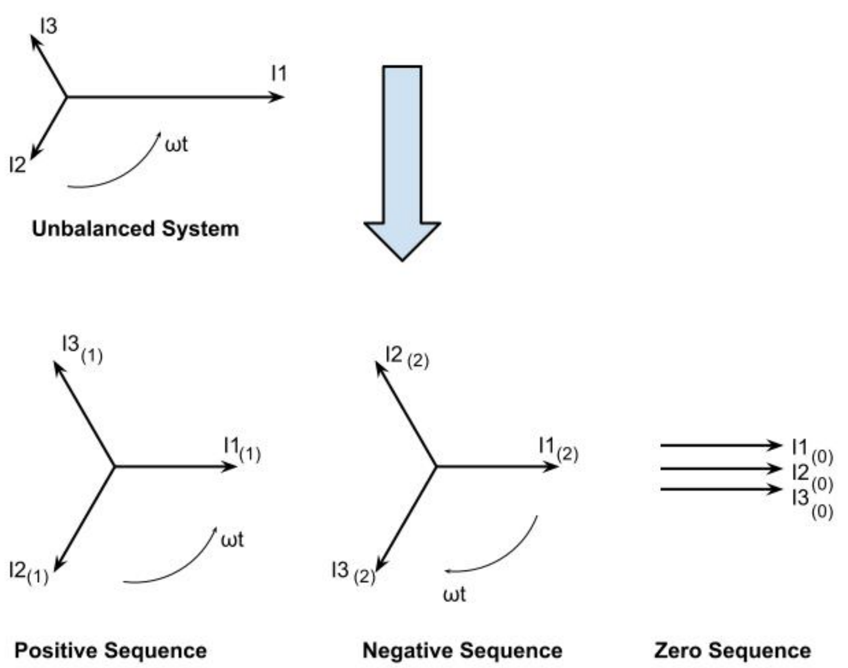

Figure B.1: The symmetrical components [69]

They are shown on Figure B.1.

The mathematical definition is:

$$U_a = U_{a,1} + U_{a,2} + U_{a,0}$$

$$U_b = U_{b,1} + U_{b,2} + U_{b,0}$$

$$U_c = U_{c,1} + U_{c,2} + U_{c,0}$$

In case of lines, the positive and negative sequence are always equal. In the specific case of the cables of this thesis, the components are all equal as long as they have the right order of magnitude, which was checked.

B.2 The Park Transform

The Park transform, also called the direct-quadrature-zero $0dq$ transformation, has been used throughout this study to model the equations of the different controls in the wind energy conversion system. This transformation facilitates the implementation of the control by simplifying the three-phase system into a direct and a quadrature component [70].

Mathematically, the Park transformation is a tensor that rotates the reference frame of the abc components in order for them to become $0dq$ [41].

$$\mathbf{X}_{abc} = \mathbf{T}_P \mathbf{X}_{0dq}$$

$$\begin{bmatrix} x_a \\ x_b \\ x_c \end{bmatrix} = \sqrt{\frac{2}{3}} \begin{bmatrix} \frac{1}{\sqrt{2}} & cos\theta & -sin\theta \\ \frac{1}{\sqrt{2}} & cos(\theta - 2\pi/3) & -sin(\theta - 2\pi/3) \\ \frac{1}{\sqrt{2}} & cos(\theta - 4\pi/3) & -sin(\theta - 4\pi/3) \end{bmatrix} \begin{bmatrix} x_0 \\ x_d \\ x_q \end{bmatrix}$$

The angle θ is the phase difference between the a-axis and the direct-axis.The inverse of the transformation is quite easy to compute as $\mathbf{T}_P^{-1} = \mathbf{T}_P^T$.

The governing equations can all be rewritten in the $0dq$ reference frame, which simplifies them allowing a control on the direct component and one on the quadrature component.

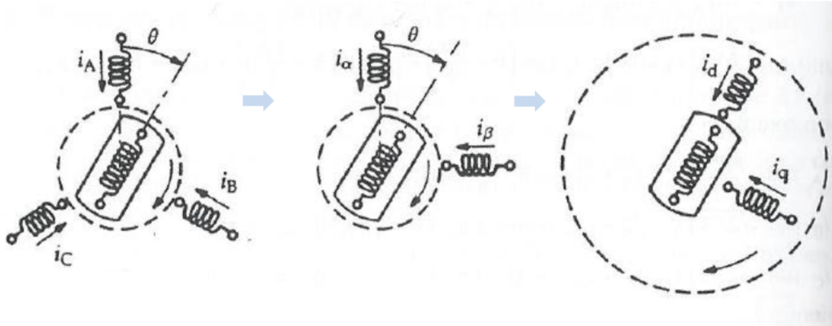

Figure B.2: The Park transform applied to a synchronous generator [41]

In case of the synchronous generator, the rotation is shown in Figure B.2. The transformation shows that the zero-sequence component is fully decoupled from the others.

$$v_0 = R_s i_0 + (L_s + 2M_s)\frac{di_0}{dt}$$

with M_s the mutual inductance in the stator. It does not participate in the electromechanical energy conversion and is only responsible for Joule losses [41].

B.3 Reactive Power

As we are dealing with power system using alternating current (AC) and a current and voltage that are sinusoidal, the apparent power S of the system is divided into active power P and reactive power Q [71]. The active power [W] is the real part of the apparent power [VA] while the reactive power [VAr] is the imaginary part:

$$S = P + jQ$$

P translates a unidirectional energy exchange of power between the source and the load, that power is dissipated by the real impedance. Q shows the energy reversibly stored in and out of a reactance, it is the bilateral energy exchange between the source and the load, therefore between the generator and the consumer.

B.4 The Simulink-SimPowerSystems Blocks

The Simulink blocks were built in the Simscape - Power System environment and partly inspired by [65] and [66].

Figure B.3 shows the conversion chain with the switching model. The PMSG is blue and the grid is orange. The mechanical model of the wind turbine and the wind are in green and both controllers are pink. In Figure B.4, the conversion chain is represented with the average model. The same color code is used. The model for the DC link voltage is in a darker green.

The mechanical model of the wind turbine used for the tests performed exclusively with Simulink is shown in Figure B.5. A color code is used to put the inputs at the right place easily.

The stator side controller of the WECS is presented in Figure B.6. Voltages V_d and V_q are computed by speed controller and the current controllers. Again, a color code facilitates the reading. For the grid side controller, refer to Figure B.7. A dark green block shows the phase-locked-loop, but its details are shown in Figure B.8. The inputs need to be processed before being used by the controllers. Indeed, the control is applied to the direct and quadrature components. Regulation is employed for the DC link voltage and the reactive power. Both controllers are implemented in the switching and the average model.

Figure B.9 presents the layout of the farm. The PCC at the onshore grid is colored in orange, in pink is the HVAC cable, the transformers are purple and the array cable is yellow. Again, the wind is in the green block. To see the radial feeders, one has to go inside the blue block. This can be observed in Figure B.10. The WECS presented in Figure B.4 are inside the blue blocks.

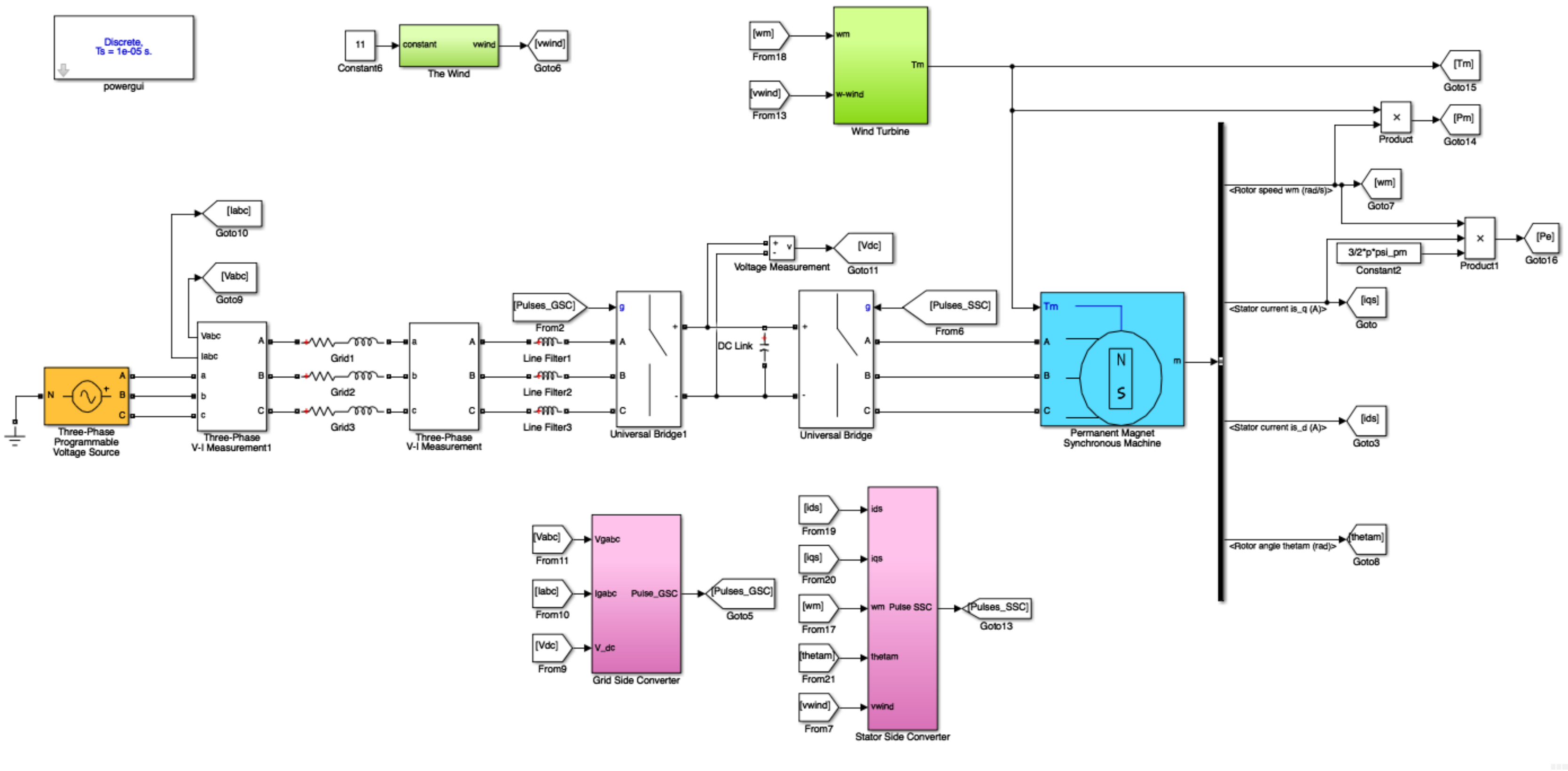

Figure B.3: The detailed implementation of the WECS

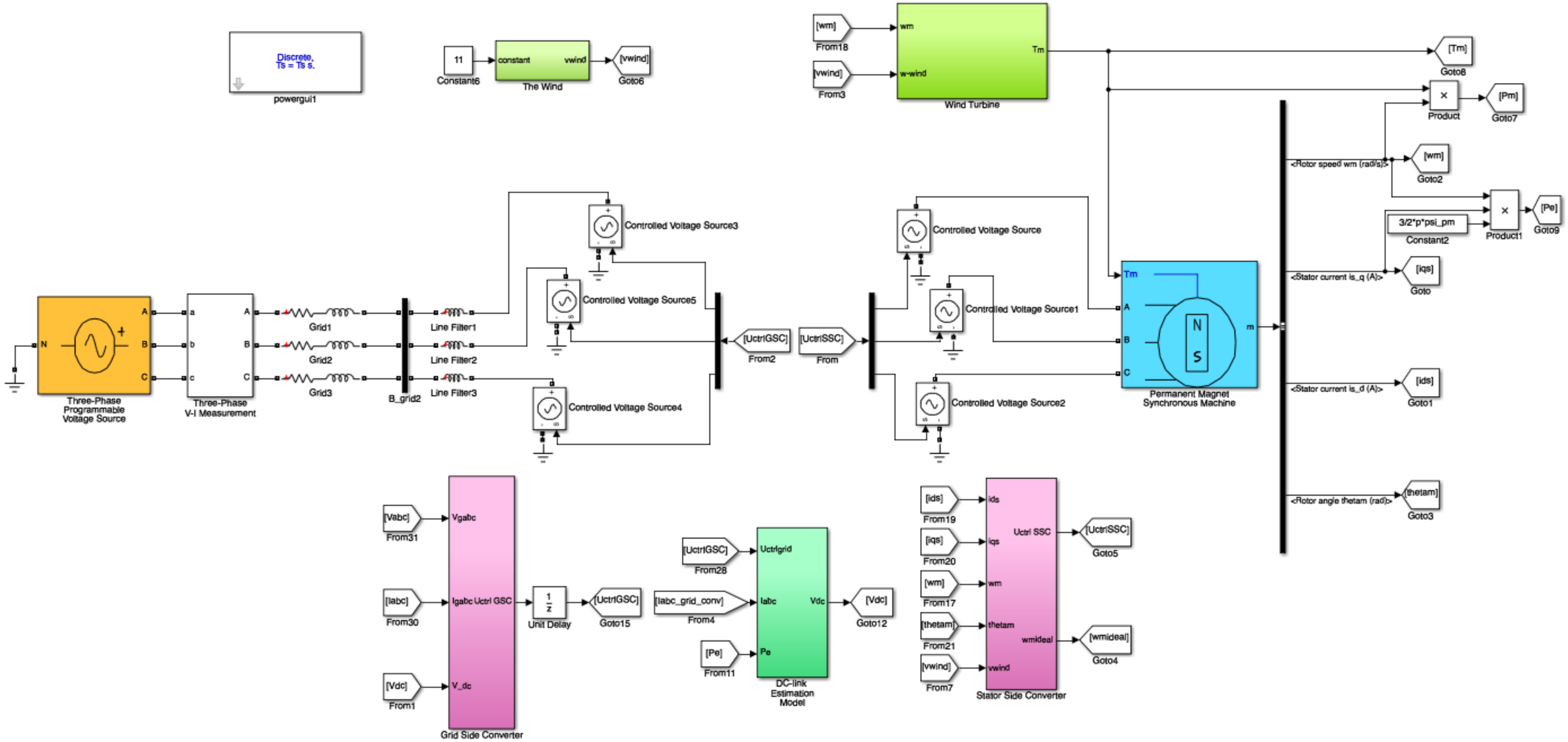

Figure B.4: The averaged implementation of the WECS

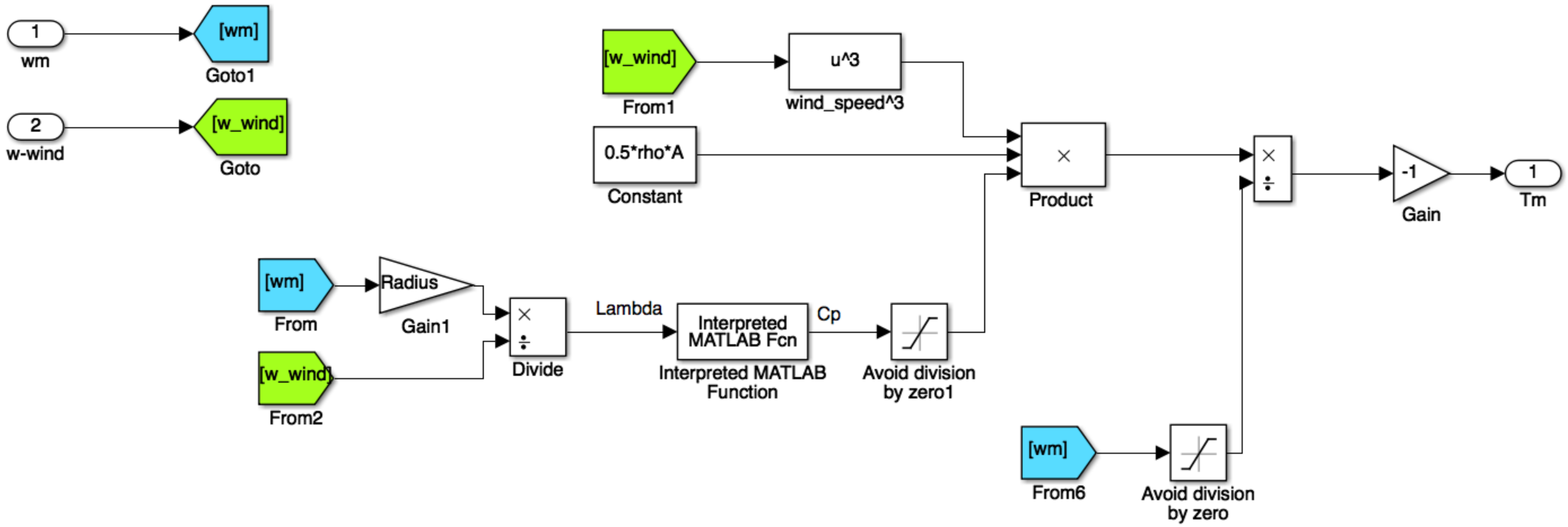

Figure B.5: The model of the wind turbine used for the tests before the coupling

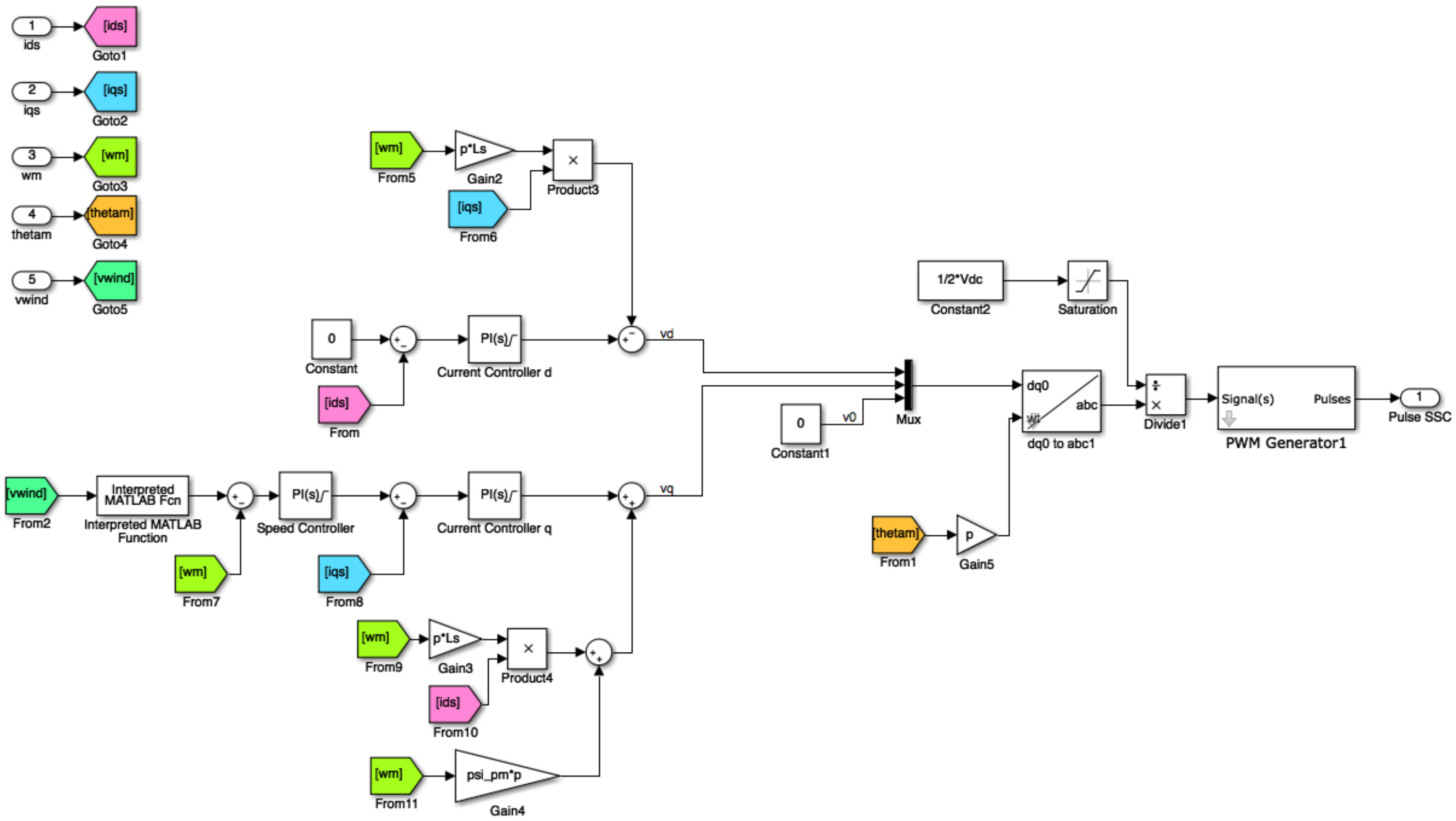

Figure B.6: The implemetation blocks of the stator side controller of the WECS

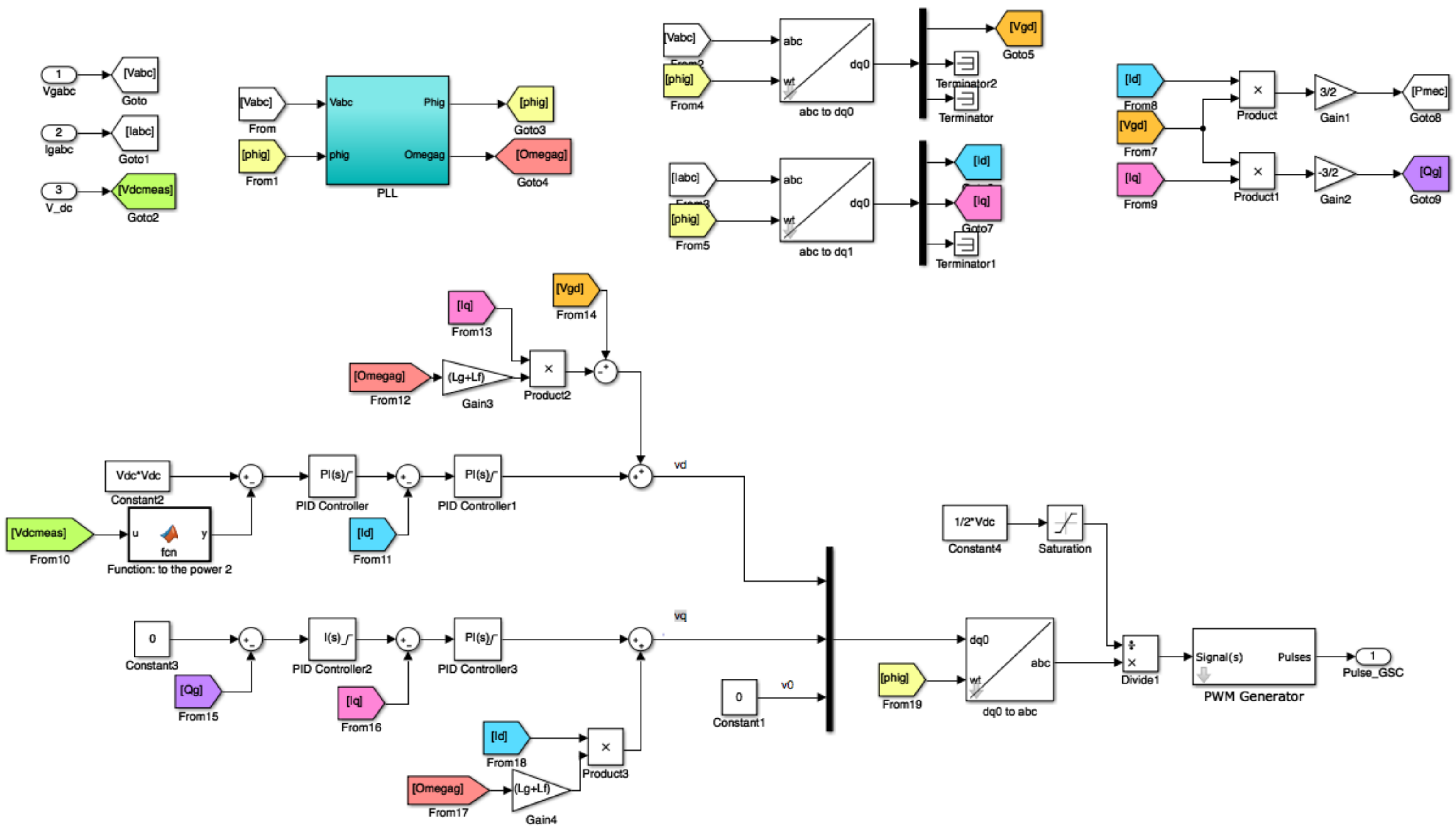

Figure B.7: The implemetation blocks of the grid side controller of the WECS

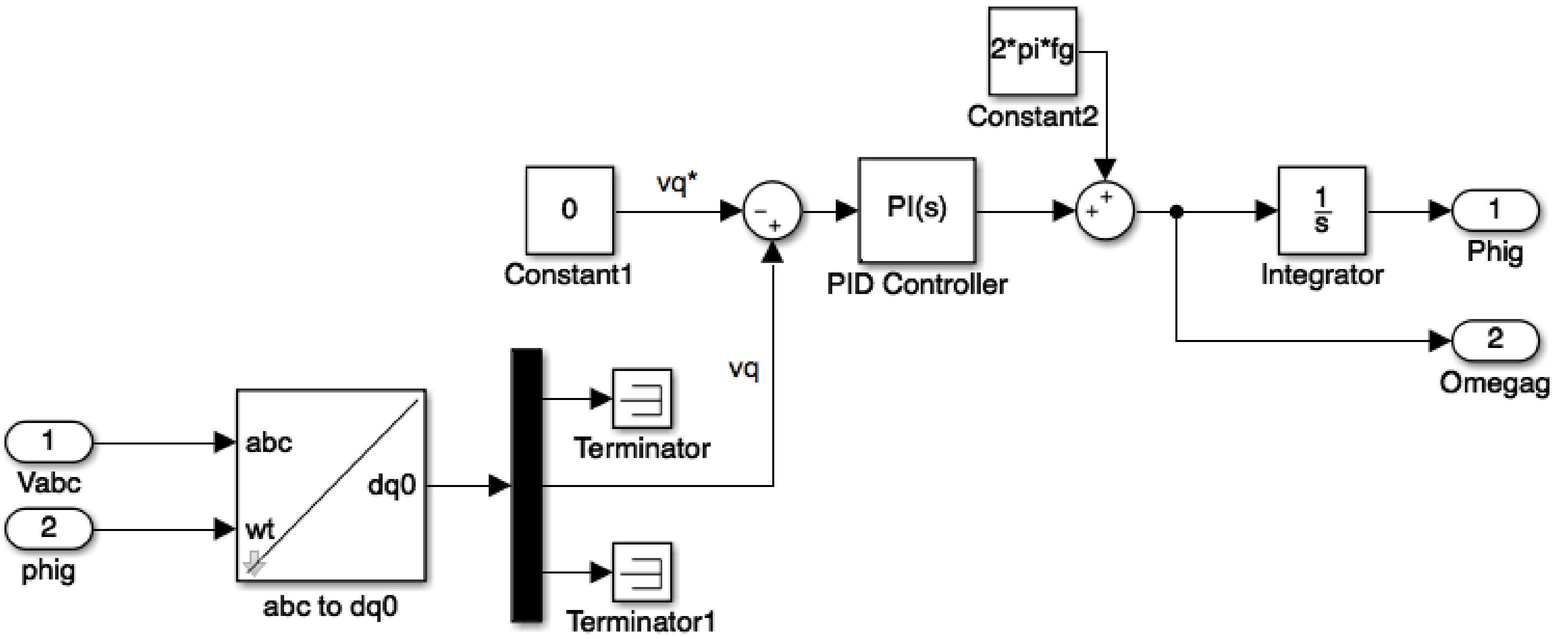

Figure B.8: The implementation of the phase locked loop

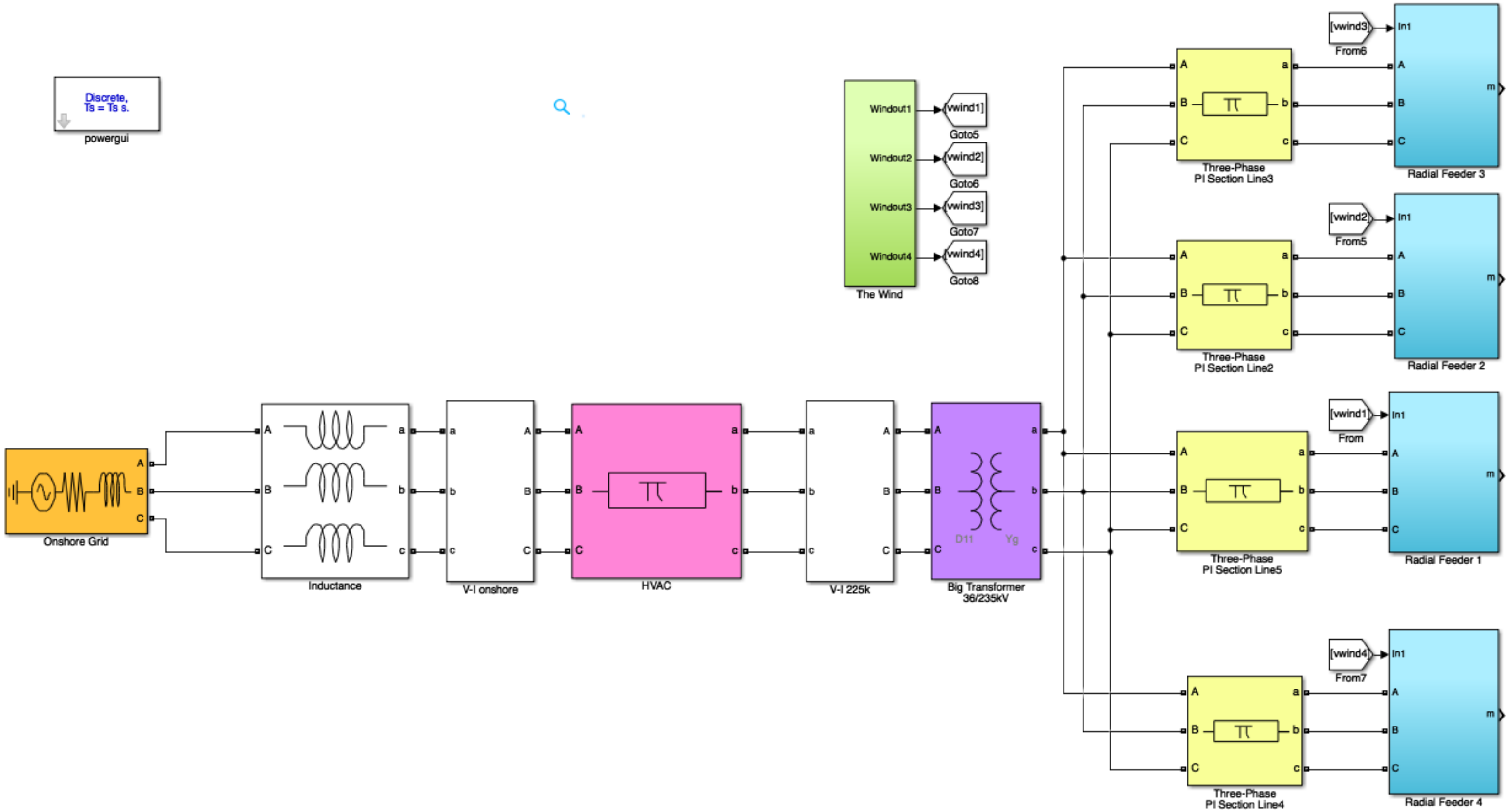

Figure B.9: The implementation of farm of 20 wind turbines

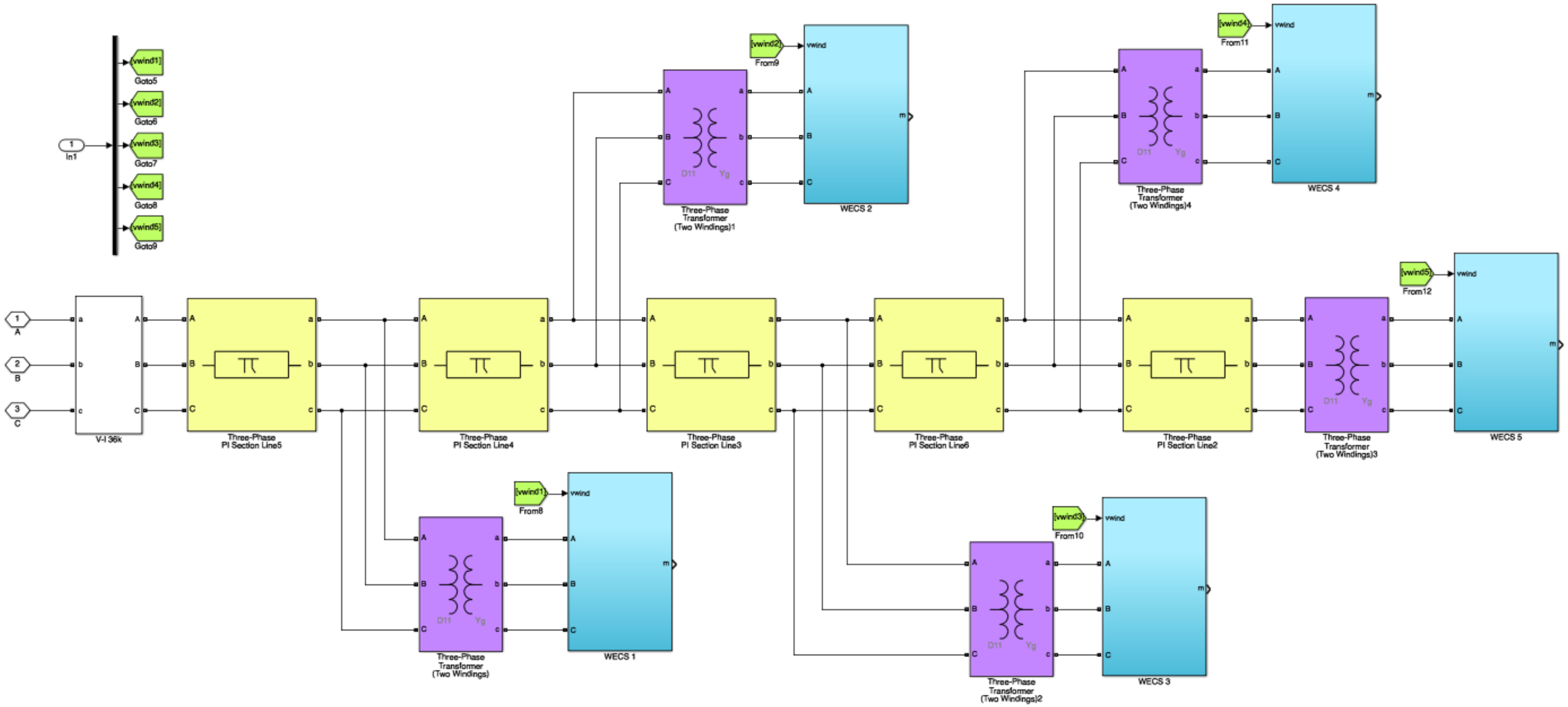

Figure B.10: The implementation of one radial feeder connecting 5 wind turbines

B.5 Matlab Code

The Matlab Code shown in this appendix allows an easy replacement of the parameters of the entire chain, making the simulations useful in other possible situations.

```
%%%%%%%%%%% Electrical Parameters %%%%%%%%%%%
% Data for the HAWT farm
%% Wind Turbine
Radius = 126/2; %m
A = pi*Radius^2; %m^2
rho = 1.225; %kg/m^3
Jwt =  38.759228 * 10^6; %kg m^2 - inertia of the wind turbine

%% Permanent Magnet Synchronous Generator
Pnom = 5.3*10^6; %W - Nominal power
Tnom = 4.18*10^6; %Nm - Nominal torque
wnom =  Pnom/Tnom; %rad/sec - Nominal speed
Jgen = 5025500; %kg m2 - inertia of the generator
p = 100; %Number of poles
Ls = 3.352*10^-3 + 5.028e-3; %H - Stator inductance
Rs = 0.08; %Ohm - Stator resistance
E0 = sqrt(2)*2.31*10^3; %V - Induced no load voltage at rated rpm
psi_pm = E0/(p*wnom); %Wb - Flux linkage
F = 0; % viscous damping
Tf = 0; % static friction
J = Jgen + Jwt; %kg m^2 - Total inertia
H = 1/2 * J * wnom^2/Pnom; %s - Inertial constant

%% Parameters of the generator side controller
zetas = 1; %Damping ratio

omegains = 2*pi*200; %rad/s - Internal loop pulsation
omegaouts = 2*pi*20; %rad/s - External loop pulsation

%PI parameters, internal and external
Pint = (2*zetas*omegains*Ls-Rs);
Iint = (Ls*omegains^2);

Tem = 3/2*psi_pm*p;

Pext = 2*zetas*omegaouts*J/Tem;
Iext = J*omegaouts^2/Tem;

%% Parameters of the grid side controller
fsw = 3000; %Switching frequency of the PWM

C = 4000e-6; %F - The DC link: a capacitor
Vdc = 6400; %V - DC link voltage
Lf = 4e-3; %H - Inductance for the line filter

fg = 50; %Hz - Grid frequency
Vg1 = 4000; %V WECS voltage level
```

```
Vg2 = 36000; %V Collector system voltage

%PLL
zeta_pll = 1; %Damping ratio
omega_pll = 2*pi*100; %Pulsation

PPLL = 2*omega_pll^2*zeta_pll/(omega_pll*4000);
IPLL = omega_pll^2/4000;

%Grid side converter
zetag = 1; %Damping ratio
Ed = Vg1 * sqrt(2/3); %V - Grid voltage

Lg = 1.0721e-3; %H - Estimated grid inductance
Rg = 0.06227; % Ohm - Estimated grid resistance

omegaing = 2*pi*100; %rad/s - Internal loop pulsation
omegaoutg = 2*pi*10; %rad/s - External loop pulsation

%PI parameters, internal and external
Pintg = 2*zetag*omegaing*Ltot-Rg;
Iintg = Ltot*omegaing^2;

Pextg = -2*zetag*omegaoutg*C/(Ed*1.5);
Iextg = -C*omegaoutg^2/(Ed*1.5);

tau = 2*pi/omegaoutg/5;
IQref = -1/(tau*Ed*1.5);

%% Onshore Grid Connection
% Distance from the WT to the collector system in order of WT
Dist = [0.882 0.882 0.882 0.882 0.882];

%36kV Underground cable parameters
r1_36 = 0.103; %Ohm/km
r0_36 = r1_36;
l1_36 = 0.317e-3; %H/km
l0_36 = l1_36;
c1_36 = 0.421e-6; %F/km
c0_36 = c1_36;

%245kV HVAC cable parameters
r1_245 = 0.0072; %Ohm/km
r0_245 = r1_245;
l1_245 = 3.2786e-4; %H/km
l0_245 = l1_245;
c1_245 = 0.27e-6; %F/km
c0_245 = c1_245;
```

Rue Archimède, 1 bte L6.11.01, 1348 Louvain-la-Neuve www.uclouvain.be/epl